

UNIVERSIDAD AUTÓNOMA DE SAN LUIS POTOSÍ

Doctorado Institucional en Ingeniería y Ciencia de Materiales

Study on the fabrication and ion transport properties of channel functionalized two-dimensional montmorillonite membranes

PARA OBTENER EL GRADO DE

DOCTOR EN INGENIERÍA Y CIENCIA DE MATERIALES

QUE PRESENTA

Zhenlei Wang

DIRECTOR

Dr. Damiano Sarocchi

Co-DIRECTOR

Dr Shaoxian Song



PATROCINADO POR SECIHTI Beca número 1327527

San Luis Potosí, S. L. P. diciembre de 2026

UNIVERSIDAD AUTÓNOMA DE SAN LUIS POTOSÍ

Doctorado Institucional en Ingeniería y Ciencia de Materiales

Study on the fabrication and ion transport properties of channel functionalized two-dimensional montmorillonite membranes

PARA OBTENER EL GRADO DE

DOCTOR EN INGENIERÍA Y CIENCIA DE MATERIALES

QUE PRESENTA

Zhenlei Wang

DIRECTOR

Dr. Damiano Sarocchi

Co-DIRECTOR

Dr Shaoxian Song

Sinodales

Dr. Damiano Sarocchi _____

Dr. Shaoxian Song _____

Dra. J. Viridiana García Meza _____

Dr. Lorenzo Borselli _____

Dra. Ma. Selene Berber Mendoza _____

Dr. Armando Encinas _____

San Luis Potosí, S. L. P. diciembre de 2026



Study on the fabrication and ion transport properties of channel functionalized two-dimensional montmorillonite membranes by Zhenlei Wang is licensed under Attribution-NonCommercial-NoDerivatives 4.0 International

Acknowledgement

My doctoral journey has flown by in the blink of an eye, yet memories of the past remain vivid, flashing before my eyes. Looking back, what stands out most is the unwavering support I received from my advisors, family, and fellow students throughout my research career-support for which I am deeply grateful.

The guidance of my advisors has been as vast as the ocean, illuminating the path of my journey. Whenever I reflect on my life, I cannot help but feel that I have been an exceptionally fortunate person. During my overseas academic exchange, I was fortunate to study under Dr. Damiano Sarocchi, who became a steadfast source of support, giving me the confidence and courage to pursue my studies far from home. I am sincerely grateful for his continued guidance and assistance, and for helping me navigate the uncertainties and challenges of my academic journey. I would also like to express my heartfelt gratitude to Dra. J. Viridiana García Meza, who generously offered me dedicated support and guidance in both my personal life and academic work during this period. No matter where life takes me, I will always remember the kindness and friendship of these two mentors. I look forward to the many opportunities we may have to meet again in the future. Throughout my many years of education, I have been fortunate to encounter many dedicated and responsible advisors. In particular, after entering graduate school, Professor Yunliang Zhao and Professor Tingting Zhang became not only exemplary advisors but also mentors who guided me through both words and actions. They enriched my scientific knowledge and professional expertise while also teaching me invaluable lessons about how to conduct myself and approach life's challenges. These lessons are treasures that I will cherish and benefit from throughout my life. Professor Shaoxian Song is another advisor whom I deeply respect. Like a kind and caring elder, he quietly watches over the growth of every student and offers direct and timely assistance when it matters most. In addition, I would like to extend my sincere appreciation to Dr. Lorenzo Borselli, Dra. Ma. Selene Berber Mendoza, Dr. Armando Encinas, and Lic. Maricela Lara Silva for their kindness, care, and guidance.

Life is like a voyage across the sea, and it is natural to encounter uncertainty and hardship when facing an unknown future. Whenever I lose confidence or struggle to find my direction, my family remains my eternal harbor and the place to which I can

always return, especially in my loneliest moments. As a child, I was timid and lacked confidence, yet my family quietly stayed by my side, reminding me that they would always be my strongest support, no matter what happened. Gradually, I learned to shed my timidity, face one setback after another with courage, and work toward overcoming each small goal along the way. I would also like to express my heartfelt gratitude to Ms. Dingning Ke, whose warm and sunny smile brought light into my loneliest moments. Like a mirror, she often helped me recognize my shortcomings in the most unassuming ways, enabling me to become a more thoughtful and well-rounded person. Above all, she has given me boundless encouragement and love, helping me move beyond the pain caused by pressure and become someone who faces difficulties with positivity and embraces challenges with courage.

Sincere friendship is one of life's most precious gifts. I have been truly fortunate to meet so many outstanding friends during my graduate studies, whose companionship has made the road ahead feel far less lonely. I am deeply grateful to my senior colleagues and fellow students. Lingjie Zhang, who has always looked after me like an elder brother: whether I was struggling with scientific questions or facing difficulties in daily life, he was always there to help me find effective solutions and guide me through challenging times. How fortunate I am to have such a friend! Tong Wen, Haoyu Bai, and Licai Chen, I will always cherish the memorable and demanding times we spent tackling challenging research projects together, experiences from which I learned so much. I would also like to thank my fellow students in Mexico: Ning Wang, Yingxin Chen, Jianhui Zhu, Yunjia Ling, Cui Zhang, Jie Wu, Zijia Zhang, and Weiquan Zhan. Your courage to innovate and your perseverance in the face of challenges have been truly inspiring. I sincerely wish each of you a bright and flourishing future.

Time flies, yet the road ahead remains long. Carrying with me the gratitude and enthusiasm I have gained along this journey, I will continue forward with renewed determination and a more positive outlook, striving to help others whenever I am able to do so. Finally, I sincerely acknowledge the financial support provided by the Secretariat of Science, Humanities, Technology and Innovation (SECIHTI) of Mexico, under Grant No. 1327527.

Zhenlei Wang

Mexico

Abstract

High-performance membrane materials are essential for advancing efficient ion transport and selective separation technologies. Their development is particularly important for water purification, critical resource recovery, and clean energy conversion. Two-dimensional (2D) membranes provide a versatile platform for these applications by enabling molecular-scale confinement, adjustable transport pathways, and tailored interfacial interactions. Among them, 2D montmorillonite (MMT) clay membranes are promising candidates because of their naturally layered architecture, abundant mineral resources, and potential for scalable fabrication. However, achieving uniform nanochannels, balancing transport efficiency with selectivity and structural stability remain significant challenges.

Herein, we first elaborate on the fundamental transport mechanisms in two-dimensional nanofluidic channels, and subsequently analyses how the ordered arrangement of nanoplates, the connectivity of hydrogen-bond networks, and specific recognition interactions influence membrane transport and separation performance. Furthermore, by focusing on the influencing of the performance for two-dimensional channel membranes, this study summarizes the bottlenecks facing two-dimensional membranes in terms of precise channel engineering, interface control and structural stability. To address these challenges, a series of strategies have been developed, including spatial ordering regulation, interfacial hydrogen-bond network engineering, and interfacial regulation coupled with ion-recognition engineering, to overcome the limitations of 2D MMT functional membranes in practical applications. The modified 2D MMT membranes exhibit significantly enhanced proton conductivity and ion-separation performance, with excellent stability. Benefiting from these advances, the fabricated membranes achieve a proton conductivity of 149.53 mS cm^{-1} at room temperature and outstanding Li^{+}/Mg^{2+} separation performance. The thesis provides insights into the design of artificial channel membranes and offers a range of strategies for the development of high-performance proton-exchange membranes and lithium-magnesium separation membranes.

Keywords: Two-dimensional nanofluidic channel; Montmorillonite; Proton conductivity; Ion-separation; Modification

Resumen

Los materiales de membrana de alto rendimiento son esenciales para impulsar el desarrollo de tecnologías eficientes de transporte iónico y separación selectiva. Su desarrollo reviste especial importancia para la purificación del agua, la recuperación de recursos estratégicos y la conversión de energía limpia. Las membranas bidimensionales (2D) ofrecen una plataforma versátil para estas aplicaciones, ya que permiten el confinamiento a escala molecular, la regulación de las vías de transporte y el diseño de interacciones interfaciales específicas. Entre ellas, las membranas de arcilla de montmorillonita (MMT) 2D constituyen candidatas prometedoras debido a su estructura laminar natural, la abundancia de este mineral y su potencial para la fabricación a gran escala. Sin embargo, lograr nanocanales uniformes y equilibrar la eficiencia del transporte con la selectividad y la estabilidad estructural sigue siendo un desafío importante.

En esta tesis se describen los mecanismos fundamentales de transporte en los nanocanales fluídicos 2D y se examina cómo el ordenamiento de las nanoláminas, la conectividad de las redes de enlaces de hidrógeno y las interacciones de reconocimiento específico influyen en el transporte y la separación a través de las membranas. Asimismo, mediante el análisis de los factores que determinan el rendimiento de las membranas con canales 2D, se resumen los principales obstáculos que estas presentan en términos de ingeniería precisa de canales, control interfacial y estabilidad estructural. Para superar estos desafíos, se han desarrollado diversas estrategias, entre ellas la regulación del ordenamiento espacial, la ingeniería de redes interfaciales de enlaces de hidrógeno y la regulación interfacial combinada con el diseño de mecanismos de reconocimiento iónico, con el fin de superar las limitaciones de las membranas funcionales de MMT 2D en aplicaciones prácticas. Las membranas de MMT 2D modificadas presentan mejoras significativas en la conductividad protónica y el rendimiento de separación iónica, además de una excelente estabilidad. Gracias a estas estrategias, las membranas fabricadas alcanzan una conductividad protónica de 149.53 mS cm^{-1} a temperatura ambiente y un rendimiento sobresaliente en la separación de Li^{+}/Mg^{2+}. Esta tesis aporta conocimientos fundamentales para el diseño de membranas con canales artificiales y propone diversas estrategias para desarrollar membranas de intercambio protónico y membranas de separación de litio y magnesio de alto rendimiento.

Palabras clave: Nanocanales fluídicos bidimensionales; Montmorillonita; Conductividad protónica; Separación iónica; Modificación.

Extended Abstract

The growing demand for efficient molecular and ion transport, selective separation, and electrochemical energy conversion has driven extensive research into high-performance membrane materials. These membranes are essential for applications in water purification, the recovery of critical resources, and sustainable energy technologies. Among emerging membrane platforms, two-dimensional (2D) membranes offer distinctive advantages, including tunable interlayer nanochannels, large surface areas, and tailorable interfacial chemistry, enabling precise regulation of transport pathways and selective interactions. In particular, 2 D montmorillonite (MMT) membranes have attracted considerable interest owing to their naturally layered structures, abundant availability and potential for scalable fabrication, making them promising candidates for ion separation and proton-conducting applications. Nevertheless, their practical performance remains constrained by disordered nanosheet stacking, hydration-induced swelling, heterogeneous transport channels and insufficiently controlled interfacial interactions.

Here, the fundamental transport mechanisms governing ion and molecule migration through 2D nanofluidic channels are first synthesized, including nanosheet stacking order, interfacial hydrogen-bond networks, and specific recognition interactions. Taking the natural interlayer channels, abundant raw materials, tunable surface chemistry, and the capability for scalable, low-cost production, 2D MMT materials represent an advanced option for industrial applications. It then systematically examines how structural and physicochemical regulation of these channels influences membrane performance, revealing that transport efficiency, selectivity, and structural stability are the primary limitations hindering the further development of two-dimensional channel membranes.

To elucidate the mechanism underlying the ions conduction properties of 2D MMT membranes, a series of MMT membranes featuring 3.5 Å bio-inspired proton channels were prepared. The proton transport ability of MMT sub-nanochannels was investigated systematically, which showed excellent and robust proton conductivity. Following this, an “internal regulation” strategy based on the intrinsic LCD properties of nanosheets was developed. Characterization and simulations revealed the tunable spatial orientation, proton concentration, and surface charge of such sub-nanochannels controlled by the LCD. Consequently, the optimal membrane had a proton conductivity

of 79.11 mS cm^{-1} in the absence of "external regulation" to provide external proton carriers.

To improve the orderliness of the channels in a 2D MMT membrane, a dual-constrained assembly strategy was proposed. This strategy not only enhances the electrostatic constraint effect between the nanosheets but also provides a capillary force compensation effect, thereby enabling the construction of highly oriented nanofluidic channels to achieve efficient proton transport. The exfoliated MMT nanosheets were modified with sulfonated polyvinyl alcohol (SPVA), where SPVA acted as a negatively charged coating, cross-linking agent and proton carrier. Consequently, SPVA-modified MMT (SMMT) nanosheets featured the higher negative charge to enhance the electrostatic repulsion and thereby constrain the edge-to-edge interactions, contributing the improved spatial orientation degree of nanosheets dispersion. During the assembly process, hydrogen bond interaction between SPVA and MMT nanosheets generated tensile forces to compensate for capillary forces, thus restraining the nanochannels disordering. Further, SPVA provided additional sulfonic acid groups within the aligned nanochannels to enhance Grotthuss proton transport mechanism. Benefiting from the dual-constrained assembly strategy, the prepared SMMT membrane presented ultra-high proton conductivity of 134.58 mS cm^{-1} at 30 °C, ultra-low activation energy of 9.19 kJ mol^{-1}, and outstanding stability.

To enhance the proton-conducting properties of 2D MMT membranes, a high-performance MMT proton-conductive membrane was prepared using an acid–base pair regulation strategy. This strategy established a robust and densely interconnected acid–base pair proton-conducting network within the nanofluidic channels, thereby enabling stable and rapid proton transport. The surface crosslinking and modification of MMT nanosheets using (3-aminopropyl)triethoxysilane (APTES) endow the nanochannels with silane networks for manipulating interlayer interactions. 1-Hydroxyethylidene-1,1-diphosphonic acid (HEDP) molecules were further introduced to form a stable interlocked structure with the $-NH_3^+$ groups of APTES, effectively suppressing membrane swelling in aqueous environments. Meanwhile, owing to the interplay between $-PO_3^-$ groups and $-NH_3^+$ groups, acid-base pairs were formed in the nanofluidic channels and edge regions, creating high-density hydrogen-bonding networks for low-barrier proton transport. As the result, the modified MMT membrane achieves simultaneous improvements in properties of anti-swelling, mechanical strength and proton conductivity, delivering a conductivity as high as 149.53 mS cm^{-1}, representing

a 31.38% increase over the pristine membrane.

To realize efficient recovery and separation of Li^+/Mg^{2+} from brine, a novel two-dimensional nanochannel edge-functionalization strategy has been proposed. By precisely regulating the ion pathway, a selective polyamide (PA) layer can be constructed in a controlled manner, thereby enabling the preparation of advanced nanofiltration membranes capable of efficiently separating Li^+/Mg^{2+}. Specifically, a 2D MMT layer was first deposited onto a PVDF substrate, followed by selective edge functionalization with APTES to introduce positively charged amino groups ($-NH_3^+$) at the edges of the MMT nanochannels. These $-NH_3^+$ functionalized edge sites effectively regulated the diffusion of PEI through the two-dimensional nanochannels and simultaneously tailored the transport environment for Li^+/Mg^{2+}. This functionalization of the nanochannel edges precisely regulates the diffusion of PEI through the two-dimensional layer toward the organic phase, granting governance over the ensuing interfacial amidation. This strategy produced a highly crosslinked PA selective layer with a compressed pore size spread, reduced thickness, and fewer structural defects. Meanwhile, the $-NH_3^+$ functionalized MMT nanochannels provided additional ion-recognition sites through electrostatic interactions, further suppressing the transport of Mg^{2+}. Consequently, compared to traditional NF membranes, the ASMMT/PA membrane exhibited remarkably enhanced Li^+/Mg^{2+} separation selectivity.

Contents

Acknowledgement I
Abstract I
Resumen II
Extended Abstract III
Contents VI
Index of Figures IX
Chapter 1. 1
Introduction 1
1.1. Justification 1
1.2. Objectives 3
1.2.1. General objective 3
1.2.2. Goals 3
1.3. References 4
Chapter 2. 7
Literature Review 7
2.1. Introduction 7
2.2. Fundamental concepts of ion transport in 2D layered nanochannels 9
2.2.1. Geometric Sieving Mechanism 9
2.2.2. Hydration Shell Modulation 10
2.2.3. Electrical Double Layer (EDL) Controlled 11
2.2.4. Surface Charge and Diffusion Mechanism 13
2.3. Regulation strategies for two-dimensional layered nanochannels 14
2.3.1. Interlayer spacing regulation 14
2.3.2. Nanosheet alignment regulation 16
2.3.3. Horizontal and vertical channel ordering 18
2.4. Conclusions and perspectives 19
2.5. References 20
Chapter 3. 27
Bioinspired Tunable Sub-Nanochannels in Two-Dimensional Montmorillonite Membranes for Fast and Stable Proton Transport 27
3.1. Introduction 27

3.2. Experimental section....29
3.2.1. Material synthesis....29
3.2.2. Characterizations....30
3.2.3. Layer charge density and surface charge density calculation....31
3.2.4. Ion exchange capacity determination....32
3.2.5. Vapor uptake and swelling measurement....32
3.2.6. Conductivity measurement of membranes....32
3.2.7. Molecular dynamics simulation....33
3.3. Results and discussion....34
3.3.1. Preparation and characterization of membranes with different LCD 34
3.3.2. Layer charge density-dependent ions conductivity....37
3.3.3. Ion transport mechanisms modulated by LCD in 2D sub-nanochannels 40
3.4. Conclusions....44
3.5. References....45
Chapter 4....49
A Dual-constrained Assembly Strategy of Highly Aligned Two-dimensional Montmorillonite Membrane For Efficient Proton Transport....49
4.1. Introduction....49
4.2. Experimental section....51
4.2.1. Material synthesis....51
4.2.2. Characterizations....52
4.2.3. Conductivity measurement of membranes....52
4.2.4. Liquid nitrogen transient freeze-drying treatment....53
4.2.5. Orientation factor calculation....53
4.2.6. Ion exchange capacity determination....53
4.2.7. Degree of sulfonation determination....54
4.2.8. Theoretical calculations....54
4.3. Results and discussion....54
4.3.1. Preparation of the spatially ordered SMMT nanosheets....54
4.3.2. Fabrication of the in-plane aligned SMMT membrane....58
4.3.3. Proton conductivity of the SMMT membrane....64
4.3.4. Conductivity Stability of the SMMT membrane....69
4.4. Conclusions....72

4.5. References 73
Chapter 5. 77
Conclusions 77
Conclusive remarks 79
Appendix I. Articles published during the Ph. D studies 80
Relationship Between the Research Parts 82
Appendix II. Experimental data 83

Index of Figures

Figure 2.1 Schematic illustration of nanofluidic membranes with defined channels for regulated ion transport and separation.. 7
Figure 2.2 Schematic of the regulation and effects for 2D material-based nanofluidic membranes. (a) Diversity of 2D unable nanochannels, (b) Multi-factor regulated ion transport, (c) Structural bottlenecks in 2D membranes.. 9
Figure 2.3 Geometric sieving mechanism in 2D nanofluidic membranes. (a) Precision Sieving via AB-Stacking, (b) Permeability and selectivity trade-off challenge, (c) Photothermal-triggered confined gelation (PTCG) in GLLMs membrane.. 10
Figure 2.4 Schematic illustration of hydration shell regulation and electrical double layer (EDL) overlap mechanisms in 2D nanofluidic channels. (a) Hydration shell dehydration, (b) Functional group functionalization, (c) Electrical double layer (EDL) Overlap and surface charge dominated transport.. 12
Figure 2.5 Schematic illustration of interlayer spacing regulation. (a) Physical confinement of GO membranes, (b) Cation-mediated GO membranes, (c) Polymer-assisted layered membranes ($Ti_3C_2T_x$-alginate). (d) Multivalent cation pillaring for MXene membranes 16
Figure 2.6 Schematic illustration of regulation strategies for two-dimensional layered nanochannels. (a) Control of the ordered arrangement of nanoplates, (b) Orderly arrangement of horizontal and vertical channels.. 19
Figure 3.1 Design and preparation of the bioinspired proton channels. Schematic of (a) biological proton channels with sub-nanometer hopping sites (histidine residues) and (b) artificial proton channels. (c) Schematic of MMT bioinspired sub-nanochannels for fast proton transport. Schematic and corresponding properties of (d) MMT nanosheets and (e) MMT membranes.. 29
Figure 3.2 (a) UV-vis spectra of the montmorillonite nanosheets. (b-d) Photographs of the montmorillonite nanosheets under a red laser beam. (e-g) AFM images of MMT nanosheets. (h) TEM image and selected area electron diffraction pattern of m-MMT nanosheet. (i) The electrostatic potential distributions of dodecyl trimethyl ammonium chloride and XRD patterns of dodecyl trimethyl ammonium chloride intercalated MMT. (j) The calculated layer charge density of MMT by Weiss equation. (k) IEC values of MMT membranes. (l) The cross-sectional FESEM image of m@MMT membrane.. 35
Figure 3.3 (a) The HR-TEM image of m@MMT membrane and the corresponding interlayer spacing between adjacent nanosheets. (b, c) TEM image and the corresponding inverse Fourier transform (IFT) image of the m@MMT membrane. (d) XRD patterns of MMT membranes. (e) FTIR spectra of water and MMT membranes. (f) WAXS diffraction pattern and (i) 2D image of m@MMT membrane.. 36

Figure 3.4 (a) The initial water contact angle images of MMT membranes. (b) Humidity-dependent vapor adsorption-desorption curves of MMT membranes. (c) The dimensional swelling of MMT PEM at 80°C and 98% RH. (d) The proton conductivity of Nafion 117 and MMT membranes at 98% RH with different temperatures. (e) The *I/V* curves of the MMT membranes recorded in HCl-D_2O and HCl-H_2O solution of 0.1 mol L^{-1}. (f) The proton conductivity of Nafion 117 and MMT membranes at 60 °C with different humidities.....38

Figure 3.5 Thermogravimetric (TG) analysis and differential scanning calorimetry (DSC) patterns of (a) l@MMT, (b) m@MMT, and (c) h@MMT treated at 30% RH and 30°C for 24h. (d) Swelling ratio versus proton conductivity from MMT membranes and state-of-the-art PEMs reported in the literature. (e) Conducting stability of MMT membranes under the cooling-heating cycle from 30 to 80 °C at 98% RH. (f) Nyquist plots of m@MMT before and after annealing at 300 °C and defrosting at -20 °C for 12h under 98% RH and 80 °C. (g) Cross-section SEM images of MMT membrane afterannealing at 300 °C and defrosting at -20 °C for 12h. (h) XRD patterns of h@MMT before and after annealing at 300 °C and defrosting at -20 °C for 12h. (i) The relationship between proton conductivity of MMT membranes and the layer charge density.....39

Figure 3.6 (a-c) WAXS patterns for an incident Cu Kα x-ray beam parallel and corresponding azimuthal scan profiles of MMT membranes. (d-f) AFM images and roughness analysis of MMT membranes. (g) Contour plots of SAXRD patterns of MMT membranes. (h) Schematic of the surface radius of MMT membranes.. ...41

Figure 3.7 (a) Proton concentrations and (c) effective mobilities in within membranes at 98% RH with different temperatures. (b) Surface charge densities of MMT membranes under different pH values. Mean square displacement (MSD) curves of (d) protons and (f) H_2O molecules within MMT membranes. Diffusion coefficients of (e) protons and (g) H_2O molecules within MMT membranes. (h) Relationship between layer charge density and proton concentration as well as effective mobility. (i) Schematic of sub-nanochannels with different LCDs.. 44

Figure 4.1 (a) Schematic illustration of the preparation process of the SMMT membrane. (b, c) The atomic force microscopy (AFM) image and corresponding monocrystal diameter of the typical MMT nanosheets. (d) Photographs of the montmorillonite nanosheets before and after SPVA modification under a red laser beam. (e) Molecular structure and electrostatic potential of the SPVA molecule. (f) FTIR and (g) ^1H NMR spectra of SPVA. 55

Figure 4.2 (a) UV-vis absorption spectra of the SPVA solution, MMT nanosheet, and SMMT nanosheet. XPS spectra of full spectra (b) and O 1s (c) for MMT nanosheets before and after SPVA modification. (d) Zeta potential of MMT nanosheets before and after SPVA modification 56

Figure 4.3 SEM images of (a) MMT nanosheets and (b) SMMT nanosheets after liquid

nitrogen transient freeze-drying treatment. (c) POM images of MMT and SMMT nanosheets in dispersions with different concentrations. (d) Schematic illustration of the effect of SPVA modification on the spatial distribution of nanosheets in dispersions. 58
Figure 4.4 Three-dimensional AFM images of (a) MMT and (b) SMMT membranes. (c) Water contact angle images of MMT membrane and SMMT membrane. 59
Figure 4.5 Surface SEM images of (a) MMT and (b) SMMT membranes. Cross-sectional SEM images of (c) MMT and (d) SMMT membranes. The EDS mapping of the cross section of the (e) MMT and (f) SMMT membrane.. 60
Figure 4.6 (a) XRD patterns of MMT and SMMT membranes. TEM images of (b) MMT and (c) SMMT membranes. S 2p core level XPS spectra for (d) MMT and (e) SMMT membranes. (f) O 1s XPS spectra for MMT and SMMT membranes. 61
Figure 4.7 (a) POM images of MMT membrane and SMMT membrane. Analysis of nanosheet dispersion on different membrane surfaces by Fiji ImageJ software. WAXS patterns of (b) MMT and (c) SMMT membranes. 62
Figure 4.8 Schematic illustration of the hydrogen bonding interaction between interlayer SPVA and MMT nanosheets to generate tensile forces for compensating the capillary forces during water removal. 63
Figure 4.9 (a) Schematic illustration of the nanofluidic device. (b) I-V curves obtained on dry SMMT membranes. (c) The representative I-V curves of the SMMT membranes determined at different temperatures in 0.1 M HCl solution. (d) Temperature-dependent proton conductivities of the MMT and SMMT membranes.. 64
Figure 4.10 (a) Arrhenius plots of the MMT and SMMT membranes. (b) The I/V curves of the MMT and SMMT membranes recorded in HCl-D2O and HCl-H2O solution of 0.1 M at room temperature. 65
Figure 4.11 The IEC value of MMT and SMMT membranes. 66
Figure 4.12 TGA curves of (a) MMT and (b) SMMT membranes. (c) The conductivities of MMT and SMMT membranes in different electrolytes of 1 M. (d) The binding energies between Na^+/K^+ and SO_3^-. 67
Figure 4.13 Proton conductivity and activation energy of the SMMT membrane compared with those of state-of-the-art PEMs reported in the literature. 68
Figure 4.14 (a) Concentration-dependent proton conductivities of the MMT and SMMT membranes at room temperature. (b) Proton conductivities of the SMMT membrane in the low (0.1 mM) and high (0.1 M) proton concentration compared with those of state-of-the-art PEMs reported in the literature. 68
Figure 4.15 (a) The in-plane and (b) through-plane dimensional swelling of SMMT under different temperatures and 98% RH. (c) Proton conductivity stability of the SMMT membrane during the long-term test at room temperature. (d) Proton conductivity stability of the SMMT membrane under two heating-cooling cycles

from 30 to 80 °C. 70
Figure 4.16 (a) The XRD pattern of the SMMT membranes after long-term operation at the room temperature. (b) The stress-strain curves of the MMT and SMMT membranes. (c) Proton conductivity and mechanical strength of the SMMT membrane compared with those of state-of-the-art PEMs reported in the literature. (d) Representative I-V curves of the SMMT membrane recorded at 0.1 M HCl concentration at the straight and different curved states. 71
Figure 4.17 (a) The thickness of different sites from SMMT membranes. (b) Average thickness of different SMMT membranes. The error bars in the figure represent the standard deviations for nine measurements. (c) The photograph of the scaled-up free-standing SMMT membrane marked with four randomly selected test sites. (d) Proton conductivities at different sites of the scaled-up SMMT membrane. 72

Chapter 1.

Introduction

1.1. Justification

Advanced functional membranes have emerged as critical materials for efficient molecular and ion transport, selective separation, and energy conversion in a wide range of applications, including water purification, resource recovery, and electrochemical energy systems [1–4]. Despite these advances, conventional polymeric membranes often exhibit limited control over transport pathways and interfacial chemistry [5], while the trade-off between permeability, selectivity, and structural stability continues to constrain their performance in demanding ion-transport and separation applications.

Two-dimensional (2D) functional membranes have attracted growing interest as promising alternatives to conventional polymeric membranes because their atomically thin building blocks, large lateral dimensions, tunable interlayer spacing, and chemically modifiable surfaces offer versatile platforms for constructing confined transport channels [6–10]. These structural and chemical features enable the regulation of ion transport through geometric confinement, surface-charge effects, and specific interfacial interactions, providing opportunities to improve transport efficiency and selectivity while tailoring membrane functionality for different applications [11]. Nevertheless, practical implementation remains challenging because nanosheet restacking, nonuniform interlayer channels, defects, and insufficient interfacial cohesion can lead to unstable transport pathways, compromised selectivity, and inadequate mechanical or operational stability [12].

In recent years, two-dimensional clay minerals have emerged as attractive building blocks for functional membranes, owing to their natural layered structures, abundant availability, and potential for scalable and cost-effective membrane fabrication [13,14]. Unlike many synthetic 2D materials, clay minerals possess intrinsically charged silicate layers, hydrophilic surfaces, and exchangeable interlayer cations, which provide opportunities to regulate interlayer hydration, surface electrostatics, and ion-specific interactions within confined nanochannels [15,16]. Developing high-performance membranes based on two-dimensional clay minerals is therefore of considerable interest because it offers a potentially scalable route to combine naturally confined

nanochannels with tunable interfacial chemistry for selective ion transport and electrochemical energy applications.

Montmorillonite is a 2:1 layered phyllosilicate composed of an octahedral sheet sandwiched between two tetrahedral silica sheets, with isomorphic substitution generating permanent negative layer charges that are balanced by exchangeable cations in the interlayer galleries [17,18]. Its hydrophilic interlayer galleries, high cation-exchange capacity, and expandable layered structure facilitate hydration-dependent interlayer-spacing regulation and ion-surface interactions [19,20], making MMT-based materials promising for applications such as selective ion separation, water purification, and electrochemical energy devices [21]. For membrane fabrication, the plate-like morphology of MMT enables the assembly of overlapping nanosheets into continuous lamellar pathways, while its intrinsic negative charge, ion-exchange properties, and chemically accessible surfaces provide multiple routes for tuning channel dimensions, interfacial charge, and proton-conducting functionality [22–24]. However, the development of high-performance MMT membranes requires precise control over nanosheet stacking, hydration-induced swelling, interlayer-channel uniformity, and interfacial cohesion, because excessive swelling, structural defects, and weak interlayer interactions may compromise dimensional stability, mechanical integrity, and selective proton transport [25,26]. Accordingly, integrating molecular-level interfacial engineering with channel-structure regulation represents a promising strategy for functionalizing MMT membranes, as it may simultaneously strengthen interlayer cohesion, regulate hydrogen-bond networks, and create favorable pathways for efficient proton transport without sacrificing structural stability [27] .

The intrinsically layered architecture of MMT provides a natural platform of constructing functional membranes for proton transport and selective ion separation. Its negatively charged silicate surfaces, hydrophilic interlayer galleries, high cation-exchange capacity, and tunable interlayer spacing offer opportunities to regulate ion-conducting environments through interfacial chemical modification [28]. Accordingly, the optimization of MMT-based membranes should focus on two complementary directions: i) For proton transport, engineering continuous hydrogen-bond networks and favorable interfacial environments to facilitate proton migration [29]. ii) For ion separation, precisely regulating interlayer spacing, surface charge, and interfacial chemistry to enhance ion selectivity while maintaining high permeation rates [30]. Previous studies on two-dimensional layered membranes have demonstrated that

structural regulation and interfacial functionalization can improve transport performance by modulating confined pathways, ion-surface interactions, and membrane stability [31]. For example, molecular intercalation and crosslinking have been employed to regulate interlayer spacing and suppress excessive swelling in layered membranes, thereby improving structural stability and selective molecular or ion transport [7]. In addition, functionalization with proton-conducting groups and the construction of interconnected hydrogen-bond networks have been shown to facilitate proton migration and enhance proton conductivity in proton-exchange membranes [32]. Inspired by these advances, this study aims to develop an interface-engineered two-dimensional MMT membrane by combining channel ordering with hydrogen-bond network regulation, elucidate the relationships among interfacial interactions, interlayer structure, and ion-transport behavior. To establish a set of structural design strategies aimed at achieving efficient ion transport and separation performance.

1.2. Objectives

1.2.1. General objective

Building on the unique structural and physicochemical properties of 2D MMT, this study aims to develop novel functional membrane materials with engineered nanochannels and tailored interfacial chemistry to overcome the limitations of existing membranes in transport efficiency, selectivity, and structural stability. By establishing a systematic framework linking membrane fabrication, interfacial interactions, nanochannel structure, and ion-transport behavior, this research seeks to provide theoretical guidance and technical support for the development of next-generation high-performance two-dimensional functional membranes. Ultimately, this work is expected to contribute to global efforts toward the advancement of high-performance membrane technologies for addressing critical challenges in energy sustainability and resource security.

1.2.2. Goals

(1) By preparing a series of MMT membranes featuring biomimetic proton channels (with a pore diameter of 3.5 Å), the proton transport properties of MMT sub-nanochannels were systematically investigated, revealing the tunable spatial orientation, proton concentration, and surface charge of such sub-nanochannels controlled by the layer charge density (LCD).

(2) A highly ordered nanofluidic channel is constructed using a dual-constraint assembly strategy involving 2D MMT nanosheets. By modulating the physicochemical properties of the MMT nanosheets using sulphonated polyvinyl alcohol (SPVA), the electrostatic confinement effect between the nanosheets is enhanced and a capillary force compensation effect is provided, thereby creating a highly oriented nanofluidic channel for efficient proton transport.

(3) Proton transport performance is enhanced by constructing a stable and highly interconnected acid-base pairs conduction network within the interlayers of 2D MMT. By utilizing the interactions between $-PO_3^-$ groups and $-NH_3^+$ groups, acid-base pairs are formed within the two-dimensional nanofluidic channels and at the edge regions, thereby establishing a high-density hydrogen-bond network and enabling proton transport with a low energy barrier.

(4) Highly efficient separation of Li^+ and Mg^{2+} was achieved by functionalizing the edges of two-dimensional (2D) nanochannels. By directionally anchoring amino-functionalized siloxane molecules at the sub-nanochannel edge of the MMT layered membrane, the diffusion rate of PEI across the two-dimensional MMT layer edge during the IP process was modulated, resulting in the formation of a PA layer with controllable pore size and enabling efficient separation of Li^+ and Mg^{2+}.

1.3. References

[1] Wang J, Zhang X, Yu Z, et al. Fast water transport and ionic sieving in ultrathin stacked nanoporous 2D membranes. National Science Review, 2025, 12(3): nwae482.

[2] Guo Y, He J, Zhang J, et al. Deciphering co-ion and counterion transport in polyamide desalination membranes reveals ion selectivity mechanisms. Science advances, 2025, 11(23): eadu8302.

[3] Li X, Zuo P, Ge X, et al. Constructing new-generation ion exchange membranes under confinement regime. National Science Review, 2025, 12(2): nwae439.

[4] Xia J, Pan S, Li Q, et al. Fast and highly selective proton transport through Ca^{2+}-regularized laminar membrane for spontaneous acid recovery and energy generation. Water Research, 2025, 285: 124155.

[5] Chen G, Zhu H, Liu G, et al. Confinement effects and manipulation strategies of nanocomposite membranes towards molecular separation. Angewandte Chemie International Edition, 2025, 64(4): e202418649.

[6] Ma X, Sun R, Liu Y, et al. 2D Ultrathin Ion-Selective Membranes With Negatively Charged Interlayer Spacing Enabled by Edge-Sulfonated Graphene Oxide for Efficient Osmotic Power Generation. Small, 2026: e74095.

[7] Ma Z, Fan J, Zhu C, et al. Deep Dehydrated Layered Vermiculite Membrane for Selective Lithium Separation. Angewandte Chemie, 2026, 138(28): e9661914.

[8] Dai L, Guan K, Mai Z, et al. Sodium-ion traps in a two-dimensional confined channel for effective water and ion selective transport. Nano Letters, 2024, 24(43): 13686-13694.

[9] Dai L, Guan K, Hu M, et al. Heterogeneity-Guided Interlayer Tuning in Vermiculite-MOF Membranes for Efficient Li^{+}/Mg^{2+} Separation. Advanced Science, 2026, 13(26): e74597.

[10] Yang K, Wang Q, Nikolaev K G, et al. Nanoconfined MXene/cellulose membranes for selective lithium extraction from brines and Black Mass. ACS nano, 2025, 19(40): 35483-35492.

[11] Wang S, Huang Y, Qiang Y, et al. Nanoconfined electrostatic interaction for efficient anion sieving in graphene oxide membranes. Water Research, 2025, 270: 122855.

[12] Zhang W, Wang Z, Wang P, et al. Efficient cation sieving and recovery via synergistic nanoconfinement and ionic anchoring in engineered PSS-functionalized nanochannel membranes. Water Research, 2026: 125529.

[13] Li S, Guo W, Li Y, et al. Modulating the Interlayer Spacing of Montmorillonite 2D Nanofluidic Membranes by Cation Intercalation for Osmotic Energy Conversion. Small, 2025, 21(34): 2506206.

[14] Booth A J, Kim M A, Sparks K I, et al. Scalable slot-die coating of phyllosilicate membranes for selective ion separations. Cambridge Materials: Water, 1-31.

[15] Jiang X, Zhang L, Miao Y, et al. Intrinsic roles of nanosheet characteristics in two-dimensional montmorillonite membranes for efficient Li+/Mg2+ separation. Water Research, 2025, 276: 123291.

[16] Stevenson M, Pappler S, Kanzler L, et al. Ion and Solvent Dynamics in Charged 2D Clay Nanoslits with Unprecedented Ångström-Precise Slit Height Control. Advanced Functional Materials, 2026, 36(8): e15706.

[17] Cui J, Wu Q, Li F, et al. Selective separation of structurally similar alkaloids by graphene oxide membranes. Separation and Purification Technology, 2024, 347: 127474.

[18] Han B, Sun X, Fan Z, et al. Enhanced mono/divalent ion separation via charged interlayer channels in montmorillonite-based membranes. Environmental Science & Technology, 2024, 58(9): 4415-4427.

[19] Liu Z, Qin M, Fu B, et al. Effective proton conduction in quasi-solid zinc-manganese batteries via constructing highly connected transfer pathways. Angewandte Chemie, 2025, 137(5): e202417049.

[20] Wang X, Wen T, Zhao Y, et al. Stabilization of structure and channel height of two-dimensional montmorillonite membrane for efficient ion separation. Colloids and Surfaces A: Physicochemical and Engineering Aspects, 2024, 696: 134277.

[21] Wang W, Zhao Y, Chen L, et al. Two-dimensional montmorillonite membranes

with controllable sub-nanochannel for precise separation of mono/divalent cations. Chemical Engineering Journal, 2024, 500: 156801.

[22] Chen Y, Gu J L, Huang M Y, et al. Cation-intercalated clay-based two-dimensional membranes for effective desalination and molecule sieving. ACS Applied Materials & Interfaces, 2024, 16(1): 1749-1756.

[23] Zhang L, Wang Z, Zhang T, et al. Bioinspired Tunable Subnanochannels in Two-Dimensional Montmorillonite Membranes for Fast and Stable Proton Transport. ACS Materials Letters, 2025, 7(8): 2835-2843.

[24] Gao Y, Qiao Z, Zhang L, et al. High-Performance Proton Exchange Membrane with Vertically Aligned Montmorillonite Nanochannels. Small, 2025, 21(7): 2409192.

[25] Wen T, Zhao Y, Kuang B, et al. Enhanced Li^+/Mg^{2+} selectivity of two-dimensional montmorillonite membranes by end-face and interfacial layer constraint for nanosheets. Separation and Purification Technology, 2024, 339: 126707.

[26] Liu J, Zhao Y, Gao R, et al. Efficient Li^+/Mg^{2+} separation by two-dimensional montmorillonite membrane with stable channel structure through ion exchange and metal–organic coordination strategy. Separation and Purification Technology, 2025, 358: 130141.

[27] Tang J, Zhang Q, Zhang M, et al. Constructing Continuous Interlayer Hydrogen-Bond Network in Nanofluidic Clay Membranes for Fast Cation Conduction and Anti-Swelling Osmotic Energy Generator. Advanced Materials, 2026: e73660.

[28] Zhang X, Chen L, Zhao Y, et al. 2D montmorillonite nanosheet layer modulated interfacial polymerization for enhanced Mg^{2+}/Li^+ separation performance from salt-lake brines by polyamide membrane. Separation and Purification Technology, 2025: 134649.

[29] Lei D, Wang Y, Zhang Q, et al. High-performance solid-state proton gating membranes based on two-dimensional hydrogen-bonded organic framework composites. Nature Communications, 2025, 16(1): 754.

[30] Lv Z, Li H, Wen C, et al. 2D biomimetic membranes constructed by charge assembly and hydrogen bonding for precise ion separation. Advanced Materials, 2025, 37(13): 2419496.

[31] Wang L, Zhang M, Deng K, et al. Non-intrusive regulation of interlayer spacing in MoS2 membranes for selective ion separation. Journal of Membrane Science, 2026: 125379.

[32] Wu Q, Zhang W, Lai C, et al. In-situ Formation of Metal-Polyphenol Networks in MXene Membranes for Efficient Molecular/Ion Sieving. Journal of Membrane Science, 2026: 125797.

Chapter 2.

Literature Review

2.1. Introduction

Nanofluidic membranes featuring well-defined nanoscale channels have attracted considerable attention for energy storage and conversion, as well as ion transport and separation, due to their unique ability to regulate molecular and ion transport at the nanoscale [1–5]. The physical and chemical properties of these intramembrane nanochannels fundamentally influence the performance of ion transport and separation across the membrane [6,7]. These structural and chemical characteristics can modulate ion transport through mechanisms such as size exclusion, electrostatic interactions, ion channel interactions, and selective hydration, thereby strongly influencing ion transport (Figure 2.1) [8]. Traditional polymeric membranes generally suffer from relatively disordered transport pathways, limited control over channel dimensions, which restrict their ability to achieve precise ion transport [9,10]. Addressing these limitations is therefore of great importance for developing membrane technologies capable of achieving both efficient and selective mass transport.

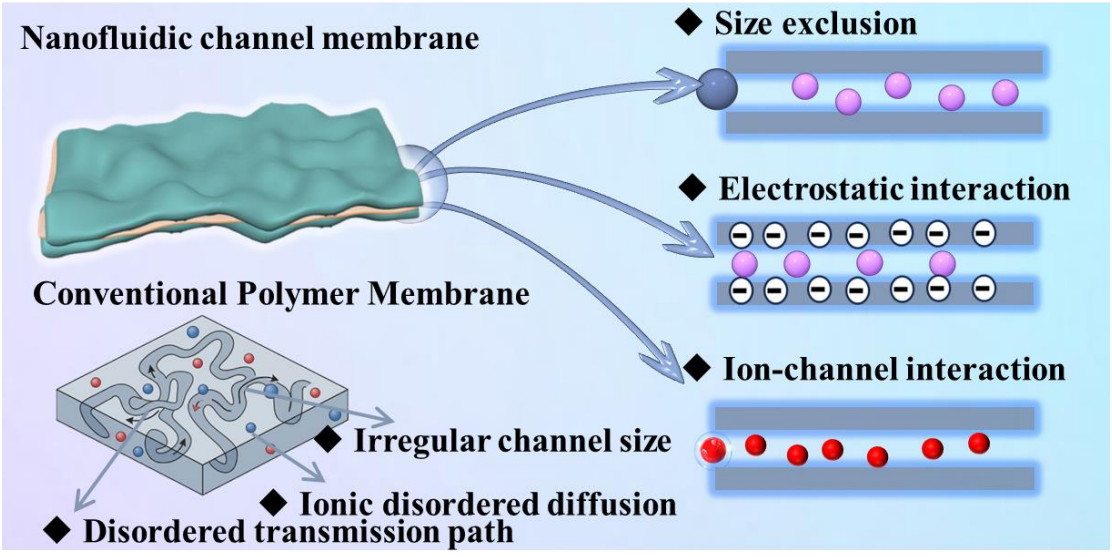


Figure 2.1 Schematic illustration of nanofluidic membranes with defined channels for regulated ion transport and separation.

The emergence of two-dimensional (2D) materials has opened up a new avenue for constructing highly confined and tunable transport pathways at the nanoscale scale

[11,12]. Early studies on 2D material membranes demonstrated that their interlayer nanochannels could serve as confined transport pathways for water, ions, and small molecules, with transport behavior strongly governed by channel dimensions and interfacial interactions [13–15]. Different classes of 2D materials have subsequently exhibited distinct advantages in proton transport and ion separation. For example, graphene-based materials provide highly confined and chemically tunable channels, MXenes offer hydrophilic surfaces and abundant functional groups, layered metal-organic frameworks enable molecularly defined pores, while clay minerals provide charged and naturally confined interlayer galleries favorable for selective ion transport (Figure 2.2a) [16–19]. Recent advances have further demonstrated that engineering the channel spacing, surface charge, functional groups, and structural ordering of 2D membranes can substantially enhance ion permeability and selectivity, highlighting the considerable potential of 2D nanofluidic membranes for high-performance proton transport and ion separation (Figure 2.2b) [20,21].

Unlike conventional polymer membranes, where ion transport is influenced by random pore connectivity, ion migration in 2D layered nanochannel systems is governed by the complex interplay of factors such as steric hindrance, interfacial electrostatic interactions, and structural order [22,23]. In particular, factors such as the functional group characteristics of 2D nanosheets and random stacking during the membrane forming process can lead to uneven interlayer spacing in two-dimensional membranes and low mass transfer efficiency, thereby increasing the tortuosity of the transport path and the transport barrier, which typically reduces selectivity and conductivity (Figure 2.2c) [24,25]. Therefore, a fundamental understanding of how the functionalization of 2D channels regulates ion transport is crucial for the rational design of high-performance membranes.

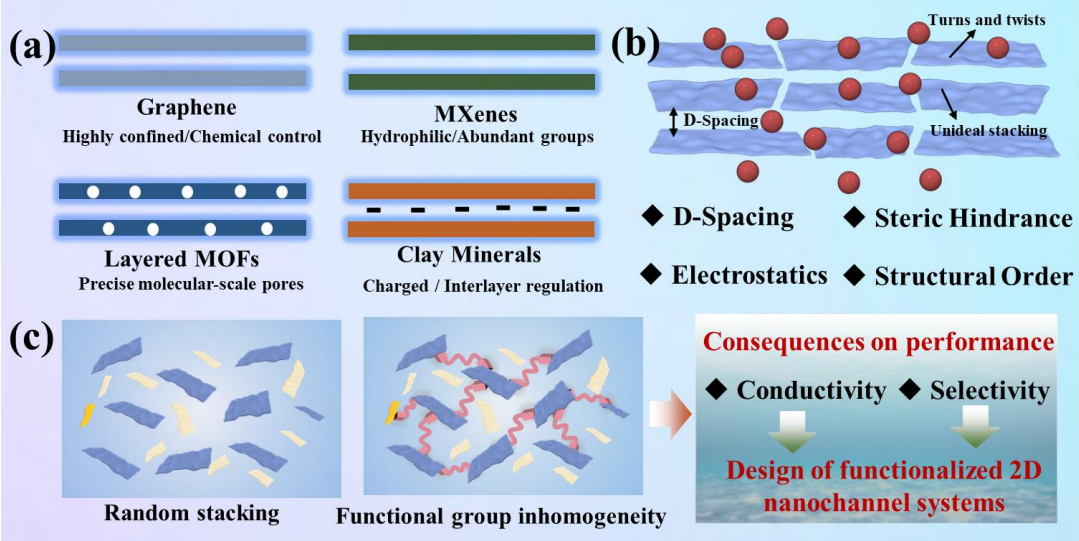


Figure 2.2 Schematic of the regulation and effects for 2D material-based nanofluidic membranes. (a) Diversity of tunable nanochannels, (b) Multi-factor regulated ion transport, (c) Structural bottlenecks in 2D membranes.

2.2. Fundamental concepts of ion transport in 2D layered nanochannels

Sub-nanoscale confinement within two-dimensional layered channels imposes strict spatial confinement effects, thereby controlling the transport behavior of ions. When the channel height is smaller than the diameter of hydrated ions, geometric sieving effects lead to strict spatial exclusion. At the same time, the confinement effect disrupts the structure of interfacial water, forcing permeating ions to undergo partial or complete dehydration [26,27]. While the geometric sieving effect provides the structural basis for size separation, its efficiency is modulated by the energetic barrier of shedding bound water molecules. The following sections will elaborate on these interacting mechanisms and their dependence on channel uniformity.

2.2.1. Geometric Sieving Mechanism

Size effect is the most fundamental transport mechanism in two-dimensional nanofluidic channel membranes, essentially determining whether ions can pass through the nanofluidic channels [28,29]. When the hydrated diameter of ions approaches the channel size, a strong size-exclusion effect occurs, allowing only species smaller than the channel height to pass through [30]. For instance, by regulating the highly polar linkers in two-dimensional metal-organic framework (MOF) nanosheets to induce AB stacking between adjacent nanosheets, the effective interlayer pore size can be reduced

by 0.372 nm. This dimension is highly favorable for the permeation of small gas molecules (such as H_2) while blocking larger ones (such as CO_2 and CH_4), thus enabling efficient hydrogen sieving (Figure 2.3a) [31].

Based on the size effect, separation and regulation of nanoscale substances can be achieved, which is crucial for applications such as ion-selective transport. However, the trade-off between ion transport rate and selectivity poses a significant challenge. Typically, larger interlayer channels provide pathways that facilitate faster ion transport but tend to compromise ion selectivity. Conversely, excessively small interlayer channels may restrict ion transport efficiency. Extensive research has focused on developing advanced membrane materials with highly stable and controllable channel dimensions (Figure 2.3b) [32,33]. For example, Xu et al. developed photothermal-triggered confined gelation (PTCG) technology, forming a highly crosslinked gel network within two-dimensional nanoconductors. This gel network "locks" the channel structure, enabling it to maintain a stable dimensions even under harsh conditions (such as varying pH and high temperatures), thereby ensuring long-term stability of the size-sieving performance [34]. As shown in Figure 2.3c, the GLLMs membrane exhibits comparable stability in its layered nanochannel structure as well as demonstrates enhanced permeability, selectivity, and stability.

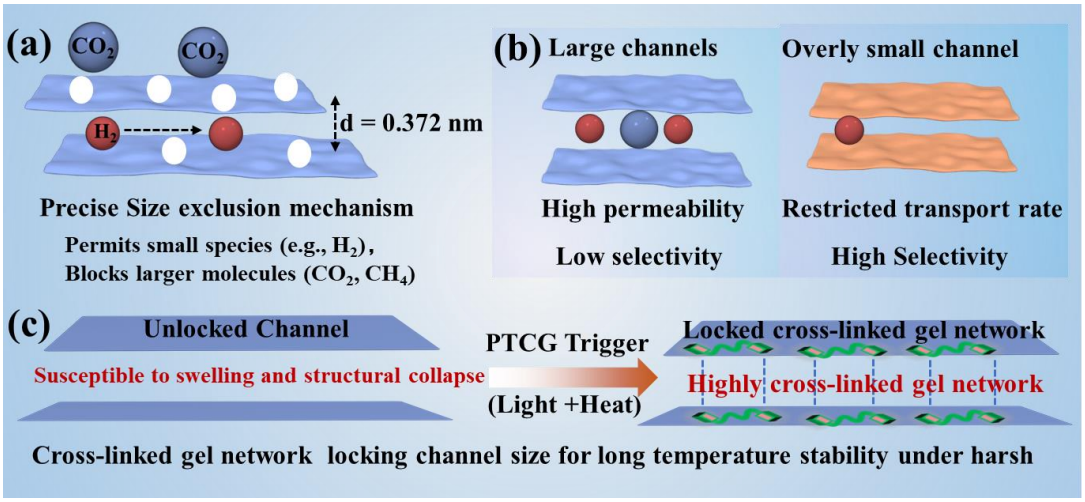


Figure 2.3 Geometric sieving mechanism in 2D nanofluidic membranes. (a) Precision Sieving via AB-Stacking, (b) Permeability and selectivity trade-off challenge, (c) Photothermal-triggered confined gelation (PTCG) in GLLMs membrane.

2.2.2. Hydration Shell Modulation

It is noteworthy that while reducing the interlayer spacing of two-dimensional channels can enhance their ion sieving performance, it is often accompanied by a

decrease in ion transport efficiency [35,36]. This occurs because hydrated ions undergoing transport through channels with severely restricted height experience “dehydration” or “deformation” effects in their hydration layers. Different ions require varying energy barriers for dehydration [17]. Multivalent ions typically possess larger hydration shells due to higher charge density, necessitating the overcoming of higher energy barriers to enter the two-dimensional channel [37]. Therefore, regulating channel height based on ion hydration layer size can effectively enhance the ion sieving capability of two-dimensional channel membranes (Figure 2.4a). To address the reduced ion transport efficiency caused by narrowing the interlayer spacing, Zhang et al. designed and simulated biological ion channels [38]. By introducing specific ion-selective imidazole groups into the interlayers of the i-GO membrane, they precisely controlled the physical constraints of the two-dimensional ion transport channel, ensuring the exclusion of divalent ions. Simultaneously, the introduction of ion-selective sulfonic acid groups facilitated the permeation of monovalent ions (Figure 2.4b).

2.2.3. Electrical Double Layer (EDL) Controlled

Beyond from steric constraints, ion transport in sub-nanometer 2D channels is primarily governed by interfacial interactions. As the channel height decreases, the surface-to-volume ratio increases dramatically, rendering surface charge the dominant determinant of ion selectivity. Fixed charges on the lamellae structure control the formation of the double electric layer (EDL) [39]. This EDL-governed mechanism is of great scientific significance and shows substantial application potential in fields such as ion separation [40], nanosensors, and energy storage and transport [41].

The electrical double layer (EDL) is the fundamental interfacial structure governing ion transport in charged two-dimensional nanochannels. The influence of the EDL strongly depends on the relationship between channel dimensions and the Debye length [42]. When the channel width is much larger than the electrical double layer thickness, counterions remain localized near the channel walls while the channel center behaves similarly to the bulk electrolyte, resulting in relatively weak ion selectivity. Conversely, when the channel dimensions are close to or less than twice the Debye length, overlapping electrical double layers occupy most of the confined space, forcing ions to migrate in a highly ordered electrostatic environment (Figure 2.4c). Under these conditions, the repulsion between co-ion ions is significantly strengthened, and ion

transport is increasingly dominated by interfacial electrostatic interactions rather than bulk diffusion. Consequently, EDL overlap transforms heterogeneous ion distributions into continuous counterion-rich transport pathways[43].

Numerous studies have demonstrated that regulating channel dimensions provides an effective strategy for enhancing EDL controlled ion transport [44,45]. When the height of a two-dimensional channel is less than 100 nm, the EDL on the charged channel surfaces overlap. leading to ion transport behaviors within the channel that differ significantly from those in macroscopic systems[46]. The effective range of EDL thickness typically lies between 0.2 and 20 nm[47,48], referred to as the Debye length (λ_D). The value of the λ_D depends on the solution's ion concentration and dielectric constant, and can be expressed as:

$$\lambda_D = \sqrt{\frac{(\varepsilon_0 RT)}{(2F^2 Ic)}}$$

Where ε_0, R, T, F, I_c, represent the dielectric constant of the solution, the universal gas constant, the absolute temperature, the Faraday constant, and the ion strength, respectively. In addition, $Ic = \frac{1}{2}\sum_i C_i Z_i^2$, where C_i, and Z_i represent the volume concentration and charge of the ions, respectively. According to this equation, the dielectric constant of the solution and the ion strength are the main factors influencing the Debye length of the electric double layer.

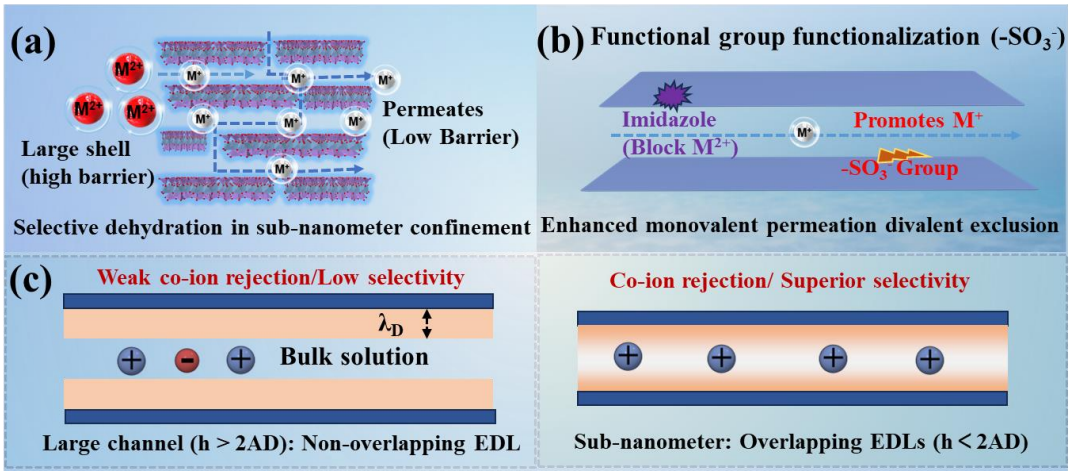


Figure 2.4 Schematic illustration of hydration shell regulation and electrical double layer (EDL) overlap mechanisms in 2D nanofluidic channels. (a) Hydration shell dehydration, (b) Functional group functionalization, (c) Electrical double layer (EDL) Overlap and surface charge dominated transport.

2.2.4. Surface Charge and Diffusion Mechanism

Surface charge is one of the most fundamental interfacial characteristics governing ion transport inside two-dimensional layered nanochannels. Unlike structural confinement, which defines the 2D layered nanochannel structure of the transport pathway. 2D layered nanochannels establish a long-range electrostatic field based on the fixed surface charges on the nanosheet base and edge positions, which continuously modulates the interaction between the transported ions and the channel walls throughout the transport process [49]. These surface charges typically originate from structures such as isomorphic ion substitutions, oxygen-containing functional groups, and structural defects within the material [50]. The resulting surface charge density (σs) determines the ζ-potential and, through the formation of an electric double layer (EDL) near the channel walls, governs the distribution of counterion enrichment and like-ion repulsion within the nanochannel.

The influence of surface charge extends beyond electrostatic attraction or repulsion. It can also influence the hydration and interfacial adsorption of ions during transport through the action of local electric fields. When hydrated ions approach charged channel walls, electrostatic interactions modify the stability of the hydration shell and alter the free energy distribution associated with adsorption, partial dehydration, and subsequent migration. For example, Xu et al. found that introducing uniformly distributed chelating groups into EDTA-functionalized MXene membranes reorganizes the local electrostatic environment, enhancing the preferential adsorption and transport of Li^+ while suppressing strongly hydrated Mg^{2+} through combined electrostatic and coordination interactions [51]. Similarly, sulfonated graphene oxide membranes create highly negative channel surfaces that stabilize hydrated proton species and facilitate proton migration through continuous hydrogen-bonding networks [52]. Although these systems employ different chemical functionalities, both demonstrate that surface charge governs ion transport by reshaping the interfacial energy landscape rather than simply increasing the number of charged sites.

Unlike bulk diffusion, where ions migrate through the entire confined solution, surface diffusion describes the preferential movement of ions along the charged channel walls under the combined influence of electrostatic attraction, hydration interactions, and interfacial chemical affinity [53]. Because ions remain partially associated with the surface during migration, the transport process is governed primarily by the physicochemical properties of the solid-liquid interface rather than by the bulk

electrolyte [54]. Consequently, the efficiency of surface diffusion strongly depends on whether the channel surface provides a spatially continuous and chemically homogeneous transport environment [55].

2.3. Regulation strategies for two-dimensional layered nanochannels

The characteristics of two-dimensional nanochannel structures determines the geometric boundaries and transport paths of confined ions and water molecules. In layered membranes formed by the assembly of two-dimensional nanosheets, structural order primarily refers to the controlled arrangement of structural parameters such as interlayer spacing [56], sheet orientation [57], stacking configuration [58], channel orientation [59], tortuosity [60], and local defects [8]. These factors collectively determine whether the channels exhibit uniform, continuous, and low-resistance transport characteristics, and further influence size exclusion, ion dehydration energy barriers, diffusion path length, and transmembrane transport efficiency. Unlike the disordered, tortuous, and difficult-to-control three-dimensional free-volume channels found in traditional polymer membranes, two-dimensional layered membranes can form relatively well-defined slit-like channels through the assembly of nanoplates, providing a foundation for the design of channel structures. This section will discuss the controlled structural ordering of two-dimensional channels in terms of interlayer spacing regulation, layer orientation and stacking order, horizontal/vertical channel orientation, as well as transport mediated by defects, wrinkles, and voids.

2.3.1. Interlayer spacing regulation

Interlayer spacing is the most direct structural parameter governing transport in two-dimensional laminar membranes. When nanosheets are stacked into a layered architecture, the interlayer galleries define slit-like nanochannels through which ions, water molecules, and other permeants migrate [61]. Therefore, regulating the interlayer spacing provides the geometric boundary for size exclusion [62]. However, in real hydrated membranes, the role of interlayer spacing is far more complex than a static pore-size descriptor. The experimentally measured d-spacing represents an averaged periodic distance, while the effective transport space is further affected by nanosheet thickness, surface functional groups, intercalated species, confined water, and solvent-induced swelling [63]. Therefore, interlayer spacing regulation should be understood as a structural ordering strategy that determines not only the accessible channel size, but

also the dehydration barrier, local ion distribution, water structure, and interfacial transport resistance within 2D nanochannels.

As shown in Figure 2.5a, the interlayer spacing strategy was first clearly demonstrated in graphene oxide membranes, where the intrinsic swelling of hydrophilic GO laminates severely weakens ion-sieving accuracy. Abraham et al [64] provided a classical example by physically confining GO membranes after humidity-controlled adjustment of the interlayer distance. By fixing the hydrated GO channels within an angstrom-scale window, the authors showed that ion permeation decreased sharply as the channel size approached or became smaller than the hydrated ion diameter, whereas water transport was much less affected. This result established a fundamental relationship between interlayer spacing and dehydration-controlled ion transport: when the 2D slit becomes sufficiently narrow, hydrated ions must partially shed their hydration shells before entering the channel, and even a small change in spacing can lead to a large variation in ion flux. Thus, physical confinement transformed the swelling-prone GO laminate into an ordered subnanometer channel system, linking geometric regulation directly with transport-energy-barrier regulation.

Following this physical confinement concept, cation-mediated GO membranes introduced an internal route to stabilize interlayer spacing [65]. In this strategy, hydrated cations are incorporated between GO nanosheets and interact with oxygen-containing groups on the GO surface (Figure 2.5b). These cations act as interlayer spacers and coordination nodes, limiting excessive swelling and maintaining a more stable channel dimension in aqueous environments. Compared with external encapsulation, cationic intercalation is more chemically integrated with the laminar framework, because the regulating species are located inside the transport pathway itself. This work indicates that interlayer spacing can be fixed not only by external mechanical restriction, but also by ion-nanosheet interactions within the channel. More importantly, it shifts the role of ions from transported species to structural regulators of 2D nanochannels. Wang et al [66] reported a $Ti_3C_2T_x$ alginate lamellar membrane in which alginate served as an interlayer stabilizer to suppress swelling and maintain ion-sieving channels (Figure 2.5c). In this case, interlayer regulation is no longer limited to defining a narrow channel size. It also reinforces the mechanical and chemical integrity of the laminar architecture. Such polymer-assisted stabilization is particularly important for aqueous ion separation, where long-term exposure to electrolytes can otherwise lead to gradual channel expansion, nanosheet restacking disorder, or loss of selectivity.

A more precise form of MXene spacing regulation was achieved through polycationic pillaring. Zhu et al [67] used Al_{13} polycations to tune $Ti_3C_2T_x$ interlayer channels, providing a representative example of multivalent intercalation for subnanometer channel engineering (Figure 2.5d). Unlike simple hydrated ions, Al_{13} polycations possess multiple interaction sites and stronger binding capability with MXene surface terminations, enabling more robust interlayer fixation. This type of regulation combines three effects in one structure: it adjusts the channel height, strengthens interlayer coupling, and stabilizes the hydrated laminar membrane against swelling. Therefore, polycationic intercalation represents a transition from empirical spacing control to more programmable interlayer engineering, where the inserted species are selected according to size, charge, coordination ability, and their influence on the local transport environment [68].

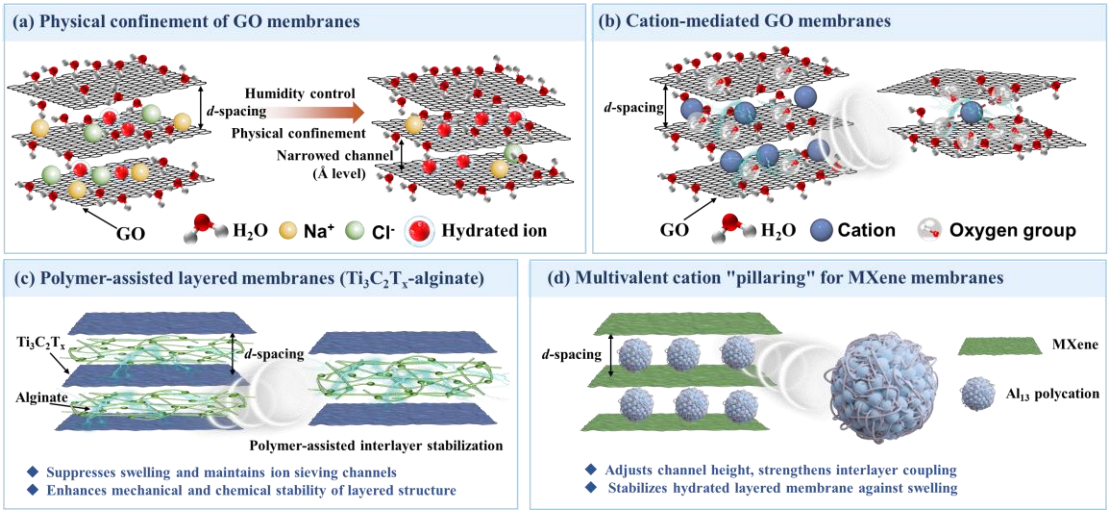


Figure 2.5 Schematic illustration of interlayer spacing regulation. (a) Physical confinement of GO membranes, (b) Cation-mediated GO membranes, (c) Polymer-assisted layered membranes ($Ti_3C_2T_x$-alginate). (d) Multivalent cation pillaring for MXene membranes

2.3.2. Nanosheet alignment regulation

Randomly stacked nanosheets may still contain interstitial voids, but such voids are usually spatially heterogeneous, discontinuous, and difficult to correlate with selective transport [69]. In contrast, aligned nanosheets can generate more coherent slit-like channels, reduce uncontrolled grain-boundary gaps, and improve the predictability of ion and water migration [70]. The alignment of nanosheets is largely determined by the assembly pathway. Pressure or vacuum assisted filtration is the most widely used

method in laboratory scale preparation of two-dimensional laminar membranes [71]. As displayed in Figure 2.6a, during filtration, directional solvent flow drives nanosheets toward the substrate, where sheets larger than the substrate pores are retained and gradually accumulate into horizontally aligned layers. This process produces near parallel slit like interlayer channels and allows membrane thickness to be regulated by the concentration or volume of nanosheet dispersion. However, filtration driven assembly is not always equivalent to ideal ordering [72]. The final membrane structure can be affected by driving pressure, suction rate, substrate type, dispersion stability, and deposition kinetics. Excessive or uneven accumulation may lead to locally dense regions, loose upper layers, cavities, or stacking defects, which weaken the correlation between membrane structure and actual transport performance.

To improve long range orientation and scalability, shear-assisted assembly has been developed as an important alternative[73] . Unlike drop coating or spray coating, which are easier to scale but often provide insufficient in-plane alignment, shear-assisted assembly introduces a directional force parallel to the substrate surface. Under such a shear field, anisotropic nanosheets tend to rotate and align along the flow direction, especially in high-viscosity or liquid-crystalline dispersions. This strategy has been demonstrated for graphene oxide and has been extended to other two-dimensional materials such as MXene and metal organic framework nanosheets [74]. The shear alignment provides a route to convert randomly distributed nanosheets into ordered transport pathways with better spatial continuity.

Interface-mediated assembly, layer-by-layer deposition, and electrophoretic assembly further expand the Methods of regulating nanosheet orientation and stacking sequence. At liquid air interfaces, graphene and MXene nanosheets can assemble rapidly under interfacial flow and Marangoni forces, leading to few-layer or laminar films with ordered structures [75]. Layer-by-layer assembly uses the sequential deposition of oppositely charged nanosheets or guest components to regulate membrane thickness, composition, and interlayer interactions [76]. This approach is particularly useful when the structural order must be coupled with charge distribution, swelling resistance, or chemical functionality. Electrophoretic assembly provides another rapid and controllable route, in which charged nanosheets migrate under an electric field and deposit onto a substrate with tunable thickness and relatively uniform structure [77]. These methods show that nanosheet alignment is not an isolated morphological issue, but a controllable assembly process involving hydrodynamic force, interfacial force,

electrostatic interaction, and electric-field-directed deposition.

2.3.3. Horizontal and vertical channel ordering

Channel orientation ordering provides an effective structural strategy to regulate the balance between selective confinement and transport resistance in two-dimensional laminar membranes. As displayed in Figure 2.6b, in conventional laminar membranes, two-dimensional nanosheets tend to stack parallel to the substrate, forming horizontal interlayer channels. Such horizontally channeled lamellar membranes provide confined slit-like galleries with tunable interlayer spacing, chemical environment, and surface charge, which are beneficial for selective ion or molecular sieving. For example, Akbari et al used the discotic nematic phase of GO to produce large-area membranes with high in-plane stacking order [78]. The shear-alignment process introduced organized horizontal GO channels and enabled continuous large-area films of about 13×14 cm^2 within less than 5 s. These membranes showed high retention above 90% for charged and uncharged organic molecules with hydrated radii larger than 5 Å.

The benefit of horizontal channel ordering comes from its ability to impose repeated confinement along the lateral migration path, but the same geometry also creates an intrinsic transport penalty. Instead, permeants usually migrate through a zigzag route composed of horizontal interlayer channels and vertical inter-sheet gaps. As a result, horizontal channel ordering provides strong confinement and selectivity, but it may also increase diffusion length and tortuosity, especially when the membrane is thick or when nanosheets have large lateral dimensions. Nie et al. provided a clear example using small-flake graphene oxide membranes for organic solvent nanofiltration [79]. Instead of changing the chemical identity of GO, they controlled the lateral dimension of GO nanosheets to construct shorter and less tortuous horizontal transport pathways. After La^{3+} crosslinking and spacing stabilization, the small-flake GO membrane achieved size-dependent ultrafast molecular transport, with methanol permeance up to 2.9 times higher than that of the large-flake GO counterpart while maintaining high selectivity toward organic dyes. This result demonstrates that horizontal channel ordering is not determined only by whether nanosheets are parallel; the continuity, length, and tortuosity of the in-plane channels can be further engineered through lateral-size regulation.

Vertical channel ordering offers a complementary route to overcome the long-pathway limitation of horizontal lamellar membranes. By orienting channels more

perpendicular to the membrane plane, vertical structures can shorten the effective transmembrane diffusion distance and reduce tortuosity while retaining the interfacial advantages of two-dimensional materials. Zhang et al. found that compared with conventional horizontally transported GO membranes, the vertically oriented GO architecture exposed shorter ion-transport pathways and larger accessible channel openings, resulting in ion permeation enhanced by about three orders of magnitude while maintaining ion selectivity [80]. In osmotic energy conversion, this vertical GO membrane achieved a power density of 10.6 W m^{-2} under artificial seawater/river water conditions. Therefore, horizontal channel ordering represents a selectivity-oriented form of structural order in two-dimensional laminar membranes. Shear alignment can improve the in-plane ordering and continuity of lamellar channels, while lateral-size engineering can shorten the horizontal diffusion pathway and reduce tortuosity [81].

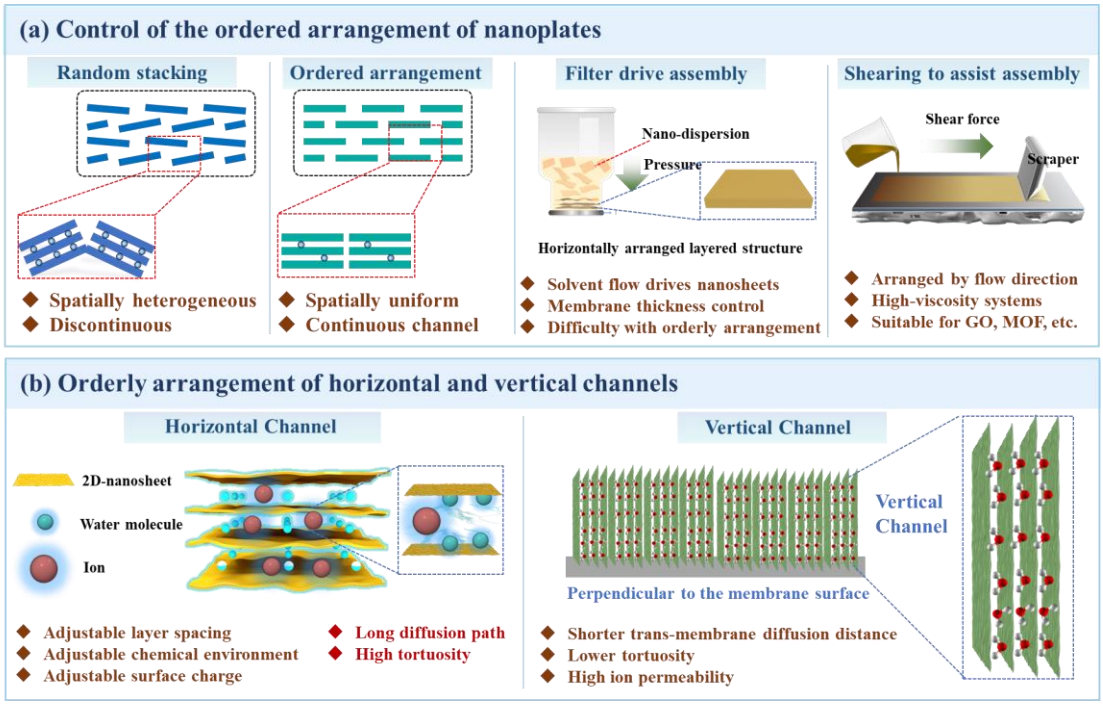


Figure 2.6 Schematic illustration of regulation strategies for two-dimensional layered nanochannels. (a) Control of the ordered arrangement of nanoplates, (b) Orderly arrangement of horizontal and vertical channels.

2.4. Conclusions and perspectives

Advanced membrane materials are critical functional materials for energy conversion, resource recovery, environmental remediation, and high-efficiency

separation. The separation efficiency, transport properties, and operational stability directly influence their energy consumption, economic viability, and practical applicability. As energy and resource utilization increasingly demands higher efficiency, lower carbon emissions, and greater separation precision, the development of advanced membranes that combine high selectivity, high permeance, and long-term stability has become scientifically and technologically important. With their ultrathin structures, tunable nanochannels, and versatile surface chemistry, two-dimensional (2D) functional membranes provide an advanced materials platform for precise ion and molecular transport, selective separation, and efficient energy conversion.

Current 2D functional membranes are primarily constructed from graphene and its derivatives, MXenes, metal-organic frameworks (MOFs), and layered clay minerals, which offer distinct advantages in structural stability, surface chemistry, channel tunability, and fabrication cost. Compared with certain 2D materials that require complex synthesis procedures or relatively high production costs, naturally layered clay minerals, such as montmorillonite and vermiculite, offer abundant reserves, low cost, intrinsic layered structures, and ion-exchange capabilities, making them promising building blocks for economical and sustainable membranes with selective ion-transport properties. Nevertheless, 2D clay membranes still face several limitations, including disordered nanosheet stacking, insufficiently precise control over interlayer spacing, interfacial defects and nonselective transport pathways, as well as swelling and structural instability in aqueous environments, which collectively hinder the simultaneous improvement of transport efficiency, selectivity, and long-term operational performance.

The central challenge in advancing 2D functional membranes lies in achieving the coordinated control of nanosheet alignment, precise construction of interlayer nanochannels, and interfacial chemistry, while establishing clear structure–property relationships linking membrane microstructure to ion-transport mechanisms and macroscopic separation performance. This lays the theoretical and technological foundations for their applications in proton conduction, ion separation, and the efficient utilization of energy and mineral resources.

2.5. References

[1] Logan B E, Elimelech M. Membrane-based processes for sustainable power generation using water, Nature 2012, 488(7411): 313-319.

[2] Zhang Z, Wen L, Jiang L. Nanofluidics for osmotic energy conversion. Nature Reviews Materials, 2021, 6(7): 622-639.

[3] Wu Z S, Feng X, Cheng H M. Recent advances in graphene-based planar micro-supercapacitors for on-chip energy storage. National Science Review, 2014, 1(2): 277-292.

[4] Liu G, Jin W, Xu N. Two-dimensional-material membranes: a new family of high-performance separation membranes. Angewandte Chemie International Edition, 2016, 55(43): 13384-13397.

[5] Kang Y, Xia Y, Wang H, et al. 2D laminar membranes for selective water and ion transport. Advanced Functional Materials, 2019, 29(29): 1902014.

[6] Kim S, Choi H, Kim B, et al. Extreme Ion-Transport Inorganic 2D Membranes for Nanofluidic Applications. Advanced Materials, 2023, 35(43): 2206354.

[7] Lozada-Hidalgo M, Hu S, Marshall O, et al. Sieving hydrogen isotopes through two-dimensional crystals. Science, 2016, 351(6268): 68-70.

[8] Wahab O J, Daviddi E, Xin B, et al. Proton transport through nanoscale corrugations in two-dimensional crystals. Nature, 2023, 620(7975): 782-786.

[9] Li X, Zuo P, Ge X, et al. Constructing new-generation ion exchange membranes under confinement regime. National Science Review, 2025, 12(2): nwae439.

[10] Wang A, Breakwell C, Foglia F, et al. Selective ion transport through hydrated micropores in polymer membranes. Nature, 2024, 635(8038): 353-358.

[11] Kang Y, Wang Y, Zhang H, et al. Functionalized 2D membranes for separations at the 1-nm scale. Chemical Society Reviews, 2024, 53(15): 7939-7959.

[12] Lu Y, Wei L, Xie Z, et al. Graphene oxide-polydopamine membranes with controlled interlayer spacing. Nature, 2026: 1-7.

[13] Nair R R, Wu H A, Jayaram P N, et al. Unimpeded permeation of water through helium-leak–tight graphene-based membranes. Science, 2012, 335(6067): 442-444.

[14] Joshi R K, Carbone P, Wang F C, et al. Precise and ultrafast molecular sieving through graphene oxide membranes. science, 2014, 343(6172): 752-754.

[15] Chen L, Shi G, Shen J, et al. Ion sieving in graphene oxide membranes via cationic control of interlayer spacing. Nature, 2017, 550(7676): 380-383.

[16] Chen C, Chen J, Peng Y, et al. Multifunctional coatings of graphene oxide: New membranes for proton permeation and salt rejection. Matter, 2024, 7(3): 1259-1274.

[17] Mo R J, Chen S, Huang L Q, et al. Regulating ion affinity and dehydration of metal-organic framework sub-nanochannels for high-precision ion separation. Nature Communications, 2024, 15(1): 2145.

[18] Zhang L, Huang Z, Chen Y, et al. Highly selective lithium-ion separation by regulating ion transport energy barriers of vermiculite membranes. ACS nano, 2026, 20(1): 1345-1356.

[19] Yi F, Huang L B, Kong L, et al. Artificial water channels-MXene membranes for enhanced desalination. CCS Chemistry, 2025, 7(10): 3050-3062.

[20] Li Y, Zhao J, Zhang J, et al. Smart and solvent-switchable graphene-based membrane for graded molecular sieving. Nature Communications, 2025, 16(1): 5363.

[21] Jiang L, Jin P, Yuan S, et al. Solvent dehydration with structurally engineered nanoporous graphene oxide membranes. Nature Communications, 2026, 17: 6006.

[22] Zhu X, Guan K, Yang F, et al. Interplay of charge composition and nanochannel confinement in ion separation through graphene oxide membranes. Water Research, 2025: 124748.

[23] Ni F, Yang Y, Zhao S, et al. Ultranarrow nanochannels in a staggered two-dimensional polymer membrane enhance electric double-layer coverage for osmotic energy harvesting. Nature communications, 2026, 17(1): 5460.

[24] Ren J, Chen X, Tong X. Microstructure-dependent ion selectivity in graphene oxide-based membranes. ACS Applied Materials & Interfaces, 2025, 17(22): 32806-32815.

[25] Zou Y, Zhang Y, Zhang J, et al. Cooperative steric modulation of flexibility, disorder, and pore size in two-dimensional covalent organic framework membranes for enhanced selective ion sieving. Journal of the American Chemical Society, 2025, 147(36): 32580-32590.

[26] Wang M, Xiong Q, Wang M, et al. Lanthanide transport in angstrom-scale MoS2-based two-dimensional channels. Science advances, 2024, 10(11): eadh1330.

[27] Zhang Y, Chen M, Zhang T, et al. Water-Mediated Ion Selectivity in 2D MXene Channels. Journal of the American Chemical Society, 2026.

[28] Liao S, Liu Y, Li L, et al. Theoretical framework for confined ion transport in two-dimensional nanochannels. Nature Communications, 2025, 16(1): 6675.

[29] Wang M, Sadhukhan T, Lewis N H C, et al. Anomalously enhanced ion transport and uptake in functionalized angstrom-scale two-dimensional channels. Proceedings of the National Academy of Sciences, 2024, 121(2): e2313616121.

[30] Kalon G, Hu S, Esfandiar A, et al. Complete steric exclusion of ions and proton transport in two - dimensional water, Science, 2019. 363, 145-148.

[31] Wu W, Cai X, Yang X, et al. Accurate stacking engineering of MOF nanosheets as membranes for precise H2 sieving. Nature Communications, 2024, 15(1): 10730.

[32] Wang J, Zhang X, Yu Z, et al. Fast water transport and ionic sieving in ultrathin stacked nanoporous 2D membranes. National Science Review, 2025, 12(3): nwae482.

[33] Wang S, Huang Y, Qiang Y, et al. Nanoconfined electrostatic interaction for efficient anion sieving in graphene oxide membranes. Water Research, 2025, 270: 122855.

[34] Li H N, Xin J H, Xu G C, et al. Gel-Locked Lamellar Membranes: Overcoming the Limitations of Permeance, Selectivity, and Stability. Advanced Materials,

2026, 38(2): e11410.

[35] Yang Y, Zhao W L, Liu Y, et al. Polyoxometalate clusters confined in reduced graphene oxide membranes for effective ion sieving and desalination. Advanced Science, 2024, 11(36): 2402018.

[36] Wang L, Zhang M, Deng K, et al. Non-intrusive regulation of interlayer spacing in MoS2 membranes for selective ion separation. Journal of Membrane Science, 2026: 125379.

[37] Zhang Y Y, Zhang Z Y, Peng H K, et al. Bridging Hydration-Shell Exchange Kinetics and Ion Translocation Energy Barriers across Graphene Nanopores. Nano Letters, 2026, 26(9): 3188-3194.

[38] Zhang M, Zhao P, Li P, et al. Designing biomimic two-dimensional ionic transport channels for efficient ion sieving. ACS nano, 2021, 15(3): 5209-5220.

[39] Bonnet N, Marzari N. Ion sieving in two-dimensional membranes from first principles. ACS Nano, 2025, 19(9): 8552.

[40] Chen C, Wu X, Chen J, et al. Built-in Electric Fields in Heterostructured Lamellar Membranes Enable Highly Efficient Rejection of Charged Mass. Angewandte Chemie International Edition, 2024, 63(29): e202406113.

[41] Guo J, Liu T, Xin W, et al. Biomimetic dual asymmetric MXene-based nanofluidics for advancing osmotic power generation. Journal of the American Chemical Society, 2025, 147(40): 36329-36338.

[42] Huang X Y, Cui Y, Ying C, et al. Scaling behavior and conductance mechanisms of ion transport in atomically thin graphene nano/subnanopores. Nano Letters, 2025, 25(4): 1722-1728.

[43] Zhang M, Jing Y, Tang J, et al. Unveiling ion-transport dynamics in 2D nanofluidic anion-selective membranes toward osmotic energy harvesting. Nano Letters, 2025, 25(37): 13857-13865.

[44] Yeom J, Choe A, Lee J, et al. Photosensitive ion channels in layered MXene membranes modified with plasmonic gold nanostars and cellulose nanofibers. Nature communications, 2023, 14(1): 359.

[45] Zou K, Ling H, Wang Q, et al. Turing-type nanochannel membranes with extrinsic ion transport pathways for high-efficiency osmotic energy harvesting. Nature Communications, 2024, 15(1): 10231.

[46] Zhang J, Liu W, Dai J, et al. Nanoionics from biological to artificial systems: An alternative beyond nanoelectronics. Advanced Science, 2022, 9(23): 2200534.

[47] Vacic A, Criscione J M, Rajan N K, et al. Determination of molecular configuration by debye length modulation. Journal of the American Chemical Society, 2011, 133(35): 13886-13889.

[48] Stern E, Wagner R, Sigworth F J, et al. Importance of the Debye screening length on nanowire field effect transistor sensors. Nano letters, 2007, 7(11): 3405.

[49] Wang Q, Zhang X, Zhu H, et al. Nanochannel-Based Ion Transport and Its Application in Osmotic Energy Conversion: A Critical Review. Advanced Physics Research, 2023, 2(9): 2300016.

[50] Nebol'Sin V A, Galstyan V, Silina Y E. Graphene oxide and its chemical nature: Multi-stage interactions between the oxygen and graphene. Surfaces and Interfaces, 2020, 21: 100763.

[51] Xu R, Kang Y, Zhang W, et al. Two-dimensional MXene membranes with biomimetic sub-nanochannels for enhanced cation sieving. Nature Communications, 2023, 14(1): 4907.

[52] Barik B, Yun Y, Kumar A, et al. Highly enhanced proton conductivity of single-step-functionalized graphene oxide/nafion electrolyte membrane towards improved hydrogen fuel cell performance. International Journal of Hydrogen Energy, 2023, 48(29): 11029-11044.

[53] Yu X, Ren W. Ion and water transport in 2D nanofluidic channels. Advanced Functional Materials, 2024, 34(30): 2313968.

[54] Xu W L, Fang C, Zhou F, et al. Self-assembly: a facile way of forming ultrathin, high-performance graphene oxide membranes for water purification. Nano letters, 2017, 17(5): 2928-2933.

[55] Long Y, Wang K, Xiang G, et al. Molecule channels directed by cation-decorated graphene oxide nanosheets and their application as membrane reactors. Advanced materials, 2017, 29(16).

[56] Wang Z, Yang J, Yong M, et al. From layered crystals to permselective membranes: history, fundamentals, and opportunities. Chemical Reviews, 2025, 125(14): 6753-6818.

[57] Wang M, Song Y J, Jiang W, et al. Layer-by-layer assembly of nanosheets with matching size and shape for more stable membrane structure than nanosheet-polymer assembly. ACS Applied Materials & Interfaces, 2024, 16(20): 26568.

[58] Cheng L, Liu G, Zhao J, et al. Two-dimensional-material membranes: manipulating the transport pathway for molecular separation. Accounts of Materials Research, 2021, 2(2): 114-128.

[59] Yang J, Fan Y, Zhang Q, et al. Two-dimensional horizontal and vertical array-based laminar membranes: An overview of synthesis, modification, and application in water treatment. Separation and Purification Technology, 2025, 365: 132666.

[60] Nie L, Goh K, Wang Y, et al. Realizing small-flake graphene oxide membranes for ultrafast size-dependent organic solvent nanofiltration. Science advances, 2020, 6(17): eaaz9184.

[61] Yang L, Qian S, Wang X, et al. Energy-efficient separation alternatives: metal–organic frameworks and membranes for hydrocarbon separation. Chemical Society Reviews, 2020, 49(15): 5359-5406.

[62] Wang Y, Lian T, Tarakina N V, et al. Lamellar carbon nitride membrane for enhanced ion sieving and water desalination. Nature Communications, 2022, 13(1): 7339.

[63] Chen B, Jiang H, Liu X, et al. Molecular insight into water desalination across multilayer graphene oxide membranes. ACS applied materials & interfaces,

2017, 9(27): 22826-22836.

[64] Abraham J, Vasu K S, Williams C D, et al. Tunable sieving of ions using graphene oxide membranes. Nature nanotechnology, 2017, 12(6): 546-550.

[65] Joshi R K, Carbone P, Wang F C, et al. Precise and ultrafast molecular sieving through graphene oxide membranes. science, 2014, 343(6172): 752-754.

[66] Wang J, Zhang Z, Zhu J, et al. Ion sieving by a two-dimensional $Ti_3C_2T_x$ alginate lamellar membrane with stable interlayer spacing, Nature communications, 2020, 11(1): 3540.

[67] Zhu J, Wang L, Wang J, et al. Precisely tunable ion sieving with an Al_{13}–$Ti_3C_2T_x$ lamellar membrane by controlling interlayer spacing. ACS nano, 2020, 14(11): 15306-15316.

[68] Pang S, Peng D, Hao Y, et al. Regulating interlayer spacing of aminated graphene oxide membranes for efficient flow reactions. Matter, 2023, 6(4): 1173-1187.

[69] Saraswat V, Jacobberger R M, Ostrander J S, et al. Invariance of water permeance through size-differentiated graphene oxide laminates. ACS nano, 2018, 12(8): 7855-7865.

[70] Shen J, Liu G, Ji Y, et al. 2D MXene nanofilms with tunable gas transport channels. Advanced Functional Materials, 2018, 28(31): 1801511.

[71] Alhammadi Y, Hai A, Taher H, et al. Enhancing heavy metals filtration: Synergistic effects of banana peel-derived activated carbon and layered double hydroxides in ultrafiltration membranes. Separation and Purification Technology, 2025, 362: 131875.

[72] Wang J, Zhou H, Li S, et al. Selective ion transport in two-dimensional lamellar nanochannel membranes. Angewandte Chemie International Edition, 2023, 62(19): e202218321.

[73] Park J, Bang K R, Cho E S. Facile fabrication of defect-controlled graphene oxide membrane through shear-induced alignment for regulating ion transport. ACS omega, 2022, 7(19): 16568.

[74] Huang L, Wu H, Ding L, et al. Shearing liquid-crystalline MXene into lamellar membranes with super-aligned nanochannels for Ion Sieving. Angewandte Chemie International Edition, 2024, 63(6): e202314638.

[75] Shim J, Yun J M, Yun T, et al. Two-minute assembly of pristine large-area graphene based films. Nano letters, 2014, 14(3): 1388-1393.

[76] Liu G, Jin W, Xu N. Two-dimensional-material membranes: a new family of high-performance separation membranes. Angewandte Chemie International Edition, 2016, 55(43): 13384-13397.

[77] Namvari M, Chakrabarti B K. Electrophoretic deposition of MXenes and their composites: Toward a scalable approach. Advances in Colloid and Interface Science, 2024, 331: 103208.

[78] Akbari A, Sheath P, Martin S T, et al. Large-area graphene-based nanofiltration membranes by shear alignment of discotic nematic liquid crystals of graphene

oxide. Nature communications, 2016, 7(1): 10891.

[79] Chuah C Y, Goh K, Yang Y, et al. Harnessing filler materials for enhancing biogas separation membranes. Chemical reviews, 2018, 118(18): 8655-8769.

[80] Zhang Z, Shen W, Lin L, et al. Vertically transported graphene oxide for high-performance osmotic energy conversion. Advanced Science, 2020, 7(12): 2000286.

[81] Li H, Lv Y, Tang Z, et al. Molecular separation applications of next-generation graphene oxide composite membranes with enhanced properties: Current status and future prospects. Separation and Purification Technology, 2025, 358: 130451.

Chapter 3.

Bioinspired Tunable Sub-Nanochannels in Two-Dimensional Montmorillonite Membranes for Fast and Stable Proton Transport

Chapter 2 showed that the order and chemistry of interlayer channels govern ion transport in 2D membranes. Before modifying those channels, it is necessary to understand how pristine MMT membranes conduct protons. This chapter studies membranes assembled from three natural montmorillonites with different layer charge density (LCD). It examines how this intrinsic property of the clay controls channel orientation, proton concentration and surface charge, and therefore proton conductivity. It addresses specific objective 1. Its main finding, that nanosheet alignment limits proton mobility, motivates the assembly strategy of Chapter 4.

3.1. Introduction

Proton transfer plays omnipresent roles process in biological processes as well as electrochemical energy storage and conversion devices [1–3]. Biological proton channels are protein-based pores that superbly regulate proton transport in living cells with high efficiency and low energy consumption [4,5]. Well-studied biological proton channels are structurally diverse, while their impeccable proton transport properties are believed to originate from the primary reasons: (i) nanoconfinement effect of sub-nanochannels and (ii) abundance of hydrophilic groups arrayed on the channels (Figure 3.1a) [6]. Such properties contribute to the orderly arrangement of proton and then rapid hopping transport through the Grotthuss mechanism on hydrogen-bond (H-bond) wires formed between water molecules and hydrophilic groups [7–9]. Inspired by biological proton channels, the design of artificial proton exchange membranes (PEMs) with sub-nano dimensions and abundant hydrophilic groups, can act as highways for rapid proton transport (Figure 3.1b).

To this end, various strategies have been developed to construct artificial proton channels by the artificial foldamers and stacking of macrocyclic blocks (e.g., metal organic frameworks (MOFs), covalent organic frameworks (COFs), cucurbit[n]urils) to

form narrow polymer pores [10–13]. However, those polymer channels tend to suffer from poor thermal stability or tortuous ion transport channels, resulting in inevitably limited proton conductivity, additionally difficult to fabricate in bulk quantities. Lately, constructing laminated architectures using two-dimensional (2D) materials have been widely explored [14–16]. Benefitting from the atomic thickness and charge-rich properties of nanosheets, the laminar membranes with well-ordered nanochannels can be readily obtained by self-assembly [17]. Graphene oxide (GO) and MXene etc. have demonstrated advanced proton transport properties [18,19]. Notably, the small and tight nanochannel structure favors H-bonds shrinks and the formation of short strong H-bonds, lowering the barrier energy experienced by the proton along the H-bonds. However, majority of above laminar membranes suffer from the channel sizes typically larger than 6 Å, failing to maximize their proton conduction potential [20,21]. Also, there are challenges of suboptimal thermal stability, e.g., GO starts to deoxidize at 200 °C [22], which limits their applications.

Montmorillonites (MMT), a class 2D nanoclays with abundant reserves, hydroxyl-rich hygroscopic surfaces and thermal stability, are promising building blocks for bioinspired proton channels [23]. MMT nanosheets feature negative charges, known as layer charge density (LCD), owing to isomorphic substitution of lower valent cations for higher valent cations in tetrahedra or octahedra or both during natural mineralization [24,25]. To maintain electroneutrality, MMT nanosheets bear inherent ion-exchange properties. During the reassembly, except for van der Waals interactions, there are the special internal sheet-ion-sheet attraction interactions between MMT nanosheets with uniformly distributed negative charges and numerous exchangeable cations in the interlayer, which is not available in GO and MXene nanosheets. Such dual interactions enable MMT membranes with aligned and stable sub-nanochannels of ~3 Å, yielding dimensions and structures comparable to those of biological proton channels for fast and robust proton transport (Figure 3.1c) [26]. Moreover, various MMTs are naturally characterized by different LCD due to geochemical differences (Figure 3.1d). As the intrinsic property of MMT nanosheets, the LCD has a distinct effect on spatial arrangement, ion exchange capacities, and surface charges of reassembled sub-nanochannels. Hence, the spatial microstructure and chemical microenvironment of lamellar membranes might be readily tuned by controlling the LCD, which further optimizes proton transport (Figure 3.1e). To date, the LCD effect of building blocks on the ionic conductivity in sub-nanochannels remains unexplored.

In this work, we constructed series of MMT membranes with bioinspired proton channels of 3.5 Å. The proton transport ability of MMT sub-nanochannels was investigated systematically, which showed excellent and robust proton conductivity. Following this, an "internal regulation" strategy based on the intrinsic LCD properties of nanosheets was developed. Characterization and simulations revealed the tunable spatial orientation, proton concentration, and surface charge of such sub-nanochannels controlled by the LCD. Consequently, the optimal membrane had a proton conductivity of 79.11 mS cm^{-1} in the absence of "external regulation" to provide external proton carriers. Therefore, this work inspires the design of artificial channel membranes and offers a unique strategy for construction of high-performance PEMs.

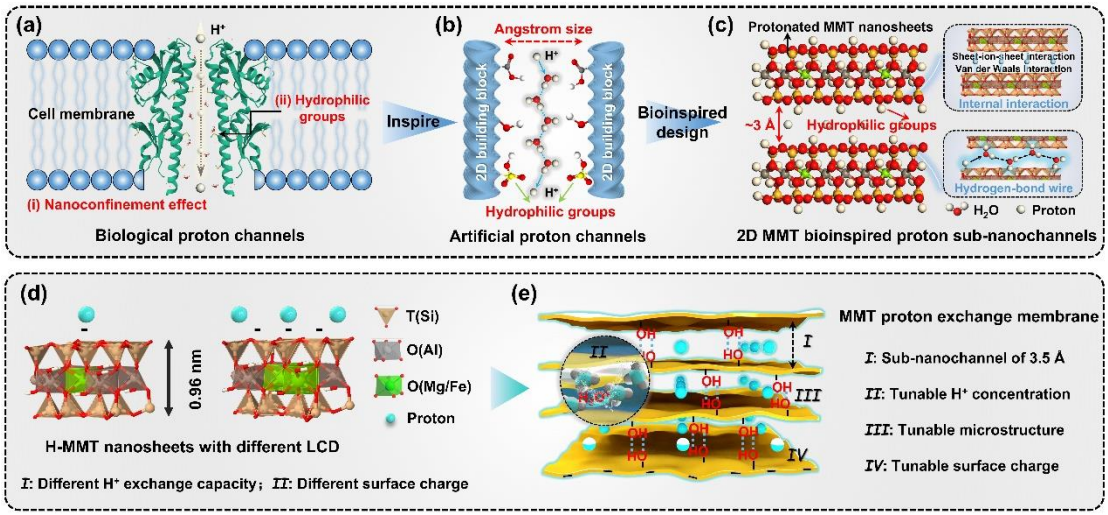


Figure 3.1 Design and preparation of the bioinspired proton channels. Schematic of (a) biological proton channels with sub-nanometer hopping sites (histidine residues) and (b) artificial proton channels. (c) Schematic of MMT bioinspired sub-nanochannels for fast proton transport. Schematic and corresponding properties of (d) MMT nanosheets and (e) MMT membranes.

3.2. Experimental section

3.2.1. Material synthesis

Materials: Lithium chloride, magnesium chloride, aluminum chloride hexahydrate, and dodecyl trimethyl ammonium chloride were purchased from Shanghai Aladdin Biochemical Technology Co., Ltd. Sodium chloride, potassium chloride, methanol, ethanol, acetone, dimethylformamide, dimethylacetamide, and N-methyl-pyrrolidone were obtained from Sinopharm Chemical Reagent Co., Ltd. Nafion 117

membrane was purchased from Sigma-Aldrich Co., Ltd.

Preparation of nanosheets and membranes: MMT is a layered aluminosilicate compound consisting of one octahedral alumina sheet sandwiched by two tetrahedral silica sheets. Isomorphic substitutional Mg^{2+} and Fe^{2+} in the octahedral sheets feature the negative charges on aluminosilicate tetrahedral-octahedral-tetrahedral layers (TOT), which are balanced by exchangeable cations between TOT [27]. The unit cell structure formula of TOT indicates $M^{n+}_{(a+b)/n}(Al_{4-a}N^{2+}_a)(Si_{8-b}Al_b)O_{20}(OH)_4$, and the tetrahedral substitution and octahedral substitution chemical formulas are as follows:

T-substitution: $M^{n+}_{a/n}[Al_{4-a}N^{2+}_a]_4[Si_8]_8O_{20}(OH)_4$

O-substitution: $M^{n+}_{b/n}[Al_4]_4[Si_{8-b}Al_b]_8O_{20}(OH)_4$

where M are interlayer exchangeable cations for electroneutrality; N^{2+} represent substitutional ions (e.g. Mg^{2+} and Fe^{2+}); n denote cation valence states. Due to different degrees of isocrystalline substitution by low valence metal ions during natural mineralization, MMT in different regions normally feature different LCDs. Herein, the three kinds of raw MMT minerals were obtained from different regions of China, which exhibited different layer charge density (LCD).

The complete preparation of MMT nanosheets involving purification, ion exchange, and exfoliation. Briefly, the MMT mineral was washed and centrifuged to remove impurities, and then resultant MMT suspension was added with NaCl to process the ion exchange to prepared Na-based MMT (Na-MMT). Then, Na-MMT was stripped by sonication (output power of 450 W), and the nanosheets with different LCD were acquired. Finally, the Na-MMT nanosheets were protonated with 1 mM HCl for 12h to prepared H-MMT nanosheets, accompanied by activation of surface hydroxyl groups, labeled as l-MMT, m-MMT, and h-MMT in the order of LCD from low to high, respectively [28].

The nanosheets with various size were obtained by changing the sonication time to realize the controlled exfoliation. The detailed methods could refer to our previous study [29]. Further, the self-standing MMT proton exchange membranes were prepared by filtering the MMT nanosheet suspensions using a polyethersulfone (PES) filter.

3.2.2. Characterizations

The interlayer spacing and composition analyses of raw minerals, nanosheets, and membranes were carried out by X-ray diffraction (XRD, Empyrean). The morphologies of MMT nanosheets and membranes were obtained by atomic force microscopy (AFM,

Multimode8), transmission electron microscopy (TEM, JEM-JEOL-2100), and field-emission scanning electron microscopy (FESEM, Gemini SEM 300). Diameter distributions and zeta potential of nanosheets were conducted by Mastersizer 2000 Laser Particle Analyzer and Malvern Zetasizer ZetaNano (Malvern). The nanosheet stacking within membranes was analyzed by a wide-angle X-ray diffractometer (WAXS, Xeuss 2.0) with Cu Kα radiation (λ=1.54189Å). N_2 adsorption-desorption isotherms were measured by ASAP2460 aperture analyzer. Contact angle (CA) of membranes was taken by micro-scopic contact angle meter (JY-JC2000C). Thermogravimetric analysis (TGA) was performed by using STA449F3 thermal synthesis analyzer with a heating rate of 10 °C min^{-1} under an N_2 atmosphere. The solid-state ^1H nuclear magnetic resonance (NMR) spectra of membranes were recorded by Bruker AVANCE III spectrometer.

3.2.3. Layer charge density and surface charge density calculation

MMT laminates exist with both fixed (permanent) and variable charges. Therein, the former density is the layer charge density (LCD) of MMT, which is related to its structure, stems from the isocrystalline substitution, and remains unchanged with reaction conditions. The latter density is the surface charge density (SCD), and the variable charge originates from the specific functional groups at the edge of MMT, the amount is closely related to the pH of the solution.

The interlayer spacing (d001, Å) of swelling clay minerals of type 2:1 (e.g., MMT) exchanged by dodecyl trimethyl ammonium chloride ($C_{12}H_{25}NH_3^+$) are linearly related to their layer charges density due to the special carbon chain structure and charge property of $C_{12}H_{25}NH_3^+$. The LCD is computed using the following equation:

$$LCD = \frac{d_{001} - 5.52}{32.98} \tag{3.1}$$

The surface charge density (zscd, C m^{-2}) is calculated based on the zeta potential [21]:

$$z_{\mathrm{scd}} = \frac{\varepsilon_0 \varepsilon_r \xi}{\lambda_D} \tag{3.2}$$

where εr and ε_0 are the dielectric constant (78.5 C^2 N^{-1} M^{-2}) and vacuum dielectric constant (8.854187817 × 10^{-12} F m^{-1}), respectively; ξ (mV) is the zeta potential, and λ_D (nm) represents the Debye length, which can be acquired according to following equation:

$$\lambda_D = \sqrt{\frac{(\varepsilon_0 \varepsilon_r k_B T)}{(2 n_{\mathrm{bulk}} z^2 e^2)}} \tag{3.3}$$

where k_B is the Boltzmann constant; T (K) refers the absolute temperature; n_{bulk}

indicates the concentration of bulk solution; z and e are the valence charge and elementary charge, respectively. Owing to the membranes bearing same ions, the λ_D only depends the ions concentration within nanochannels. Thus, the calculation of λ_D under test conditions can be simplified to the following equation [30]:

$$\lambda_D = \frac{0.304}{\sqrt{C_0}} \quad (3.4)$$

where C_0 (mol L^{-1}) is the ion concentration within nanochannels of membranes.

3.2.4. Ion exchange capacity determination

The ion exchange capacities of MMT with various LCD were measured by the barium chloride exchange method based on the Standard of the People's Republic of China for bentonite (GB/T 20773-2007).

3.2.5. Vapor uptake and swelling measurement

The membranes were cut into 2.0 cm × 2.0 cm blocks and dried in a vacuum oven at 60 °C for 24 h, and recorded the mass (W_{dry}, g), area (A_{dry}, cm^2), thickness (T_{dry}, μm). Then, the membrane was put into the thermostatic humidity chamber to measure the vapor uptake and swelling ratio. For the effect of temperature, the relative humidity was set to 98% RH, and the temperature was controlled from 30 to 80 °C. After 12 h at a specific temperature, the water was fully absorbed, and the membrane surface water was dried with filter paper and quickly tested for its mass (W_{wet}, g), area (A_{wet}, cm^2) thickness (T_{wet}, μm). Similarly, for the effect of relative humidity, the temperature was set to 60 °C, and relative humidity was controlled from 30% to 98% RH. Other procedures were the same as for the temperature effect. The vapor uptake (%), in-plane swelling ratio (%), and through-plane swelling ratio (%) were calculated according to following equation:

$$\text{Water uptake} = (W_{wet} - W_{dry}) / W_{dry} \times 100\% \quad (3.5)$$

$$\text{In-plane swelling} = (A_{wet} - A_{dry}) / A_{dry} \times 100\% \quad (3.6)$$

$$\text{Through-plane swelling} = (T_{wet} - T_{dry}) / T_{dry} \times 100\% \quad (3.7)$$

3.2.6. Conductivity measurement of membranes

Electrochemical impedance spectroscopy (EIS): The conductivity of Na^+ in MMT membranes was measured by standard two-electrode alternating current impedance method using a CHI 604E electrochemical workstation over a frequency range from 1 MHz to 0.1 Hz. The MMT membranes were mounted across two platinum electrodes and then put in the thermostatic humidity chamber. The conductivity (σ, mS

cm^{-1}) of MMT membranes was calculated by the equation $\sigma = l/AR$, where R (kΩ) represents the membrane sample resistance, l (cm) and A (cm^2) are the distance between the two electrodes and cross-sectional area of the membrane, respectively. After each change of examination conditions, the measurement is carried out after reaching the measurement conditions and stabilizing for 1 h.

Linear scan voltammetry (LSV): The LSV method was applied to measure the *I-V* curves of proton transport in the sub-nanochannels at a scanning voltage from -0.5 V to 0.5 V with the scanning rate of 0.01 V s^{-1}, in which the Ag/AgCl electrode was used as both the working electrode and reference electrode. The σ could be calculated by the following equation:

$$\sigma = Kl/wh \tag{3.8}$$

where σ (S cm^{-1}) is the ion conductivity, l (cm), w (cm), and h (cm) represent the channel length, channel width, and channel height, respectively. K refers to the slope of the *I-V* curves.

Quantitative analysis of the horizontal orientation: The horizontal orientation of MMT nanosheets stacked in MMT membranes was quantitatively analyzed using the Hermans orientation function [31]:

$$f = \frac{1}{2}(3\langle\cos^2\theta\text{-}1\rangle) \tag{3.9}$$

$$\langle\cos^2\theta\rangle = \frac{\int_0^{\pi/2} I(\theta)\cos^2\theta\sin\theta\,d\theta}{\int_0^{\pi/2} I(\theta)\sin\theta\,d\theta} \tag{3.10}$$

where f is the orientation factor; $I(\theta)$ indicates the azimuthal dependence of the X-ray scattered intensity. A perfect orientation corresponds to f value of 1, whereas a completely random orientation possesses an f value of 0.

Calculation of ion concentrations: The ion concentrations (a, mmol cm^{-3}) under different conditions were calculated by following equation [32]:

$$a = \frac{\mathrm{IEC} \times W_{\mathrm{dry}}}{V} \tag{3.11}$$

where V (cm^3) is the volume of the membrane under the tested condition.

3.2.7. Molecular dynamics simulation

Molecular dynamics (MD) simulations were carried out using the Forcite module and Amorphous Cell (AC) module of Materials Studio (MS 8.1, Accelrys, San Diego, CA) [33]. The predicted structure models of MMT membranes with ordered and sub-ordered channels were built by ClayFF force field. Specifically, MMT model were

imported, then geometrically optimized and flattened into the (001) configuration. the channels size of ions was set according to the results of XRD, and the channels structure was set based on WAXS. Then, a water module with 1000 water molecules was built by AC construction and used to combine with MMT membranes. The combined systems were further conducted geometry optimization.

Then, the proton transport and H_2O molecules were theoretically investigated by MD simulation. After NVT (N: number of particles, v: volume, t: temperature) of 100 ps and NPT (N: number of particles, p: pressure, t: temperature) of 100 ps performed to relax the structure of systems, the final 100 ps NVT process was carried out at 298 K temperature and 0.1 MPa with 0.1 fs time step to measure the mean square displacement (MSD) curve. During the whole MD simulation, the Atom based Van der Waals interaction and Ewald electrostatic summation method were employed. The diffusion coefficient ($cm^2\ s^{-1}$) was further obtained using the following equation [34]:

$$\text{Diffusion coefficient} = \frac{\lim_{t\to\infty} \text{MSD(t)}}{6t} \tag{3.12}$$

3.3. Results and discussion

3.3.1. Preparation and characterization of membranes with different LCD

MMT nanosheets were prepared by controlled exfoliation to eliminate the inevitable effect of building blocks size on proton transport. The resultant nanosheet suspensions showed a typical UV-vis spectral characteristic and Tyndall effect, and remained transparent for several months in large scale, demonstrating the homogeneous dispersion of nanosheets in water (Figure 3.2a-d). Atomic force microscopy (AFM) images indicated that the three as-obtained MMT flakes showed similar nanosheet sizes (~200 nm) with typical monolayer thickness of ~1.4 nm (Figure 3.2e-g). Transmission electron microscopy (TEM) image pattern confirmed the single-layer morphology of nanosheets with high crystallinity (Figure 3.2h). Such properties of homogeneous dispersion and high aspect ratio of nanosheets favored to fabricate sub-nanochannels. Further, layer charge densities were calculated based on Weiss equation (Figure 3.2i) [35]. The results indicated that the LCDs of MMT nanosheets (termed l-MMT, m-MMT, and h-MMT) were 0.372, 0.409, and 0.448 eq FU-1, respectively (Figure 3.2j). The outcome agrees with the color of colloidal suspensions (Figure 3.2b-d), i.e., higher LCD, greater substitution of O(Fe) for O(Si), and more yellow color of nanosheets. Then, flexible self-standing MMT membranes were easily fabricated by vacuum-assisted self-

assembly of nanosheets with the same size but different LCD, and named as l@MMT, m@MMT, and h@MMT. Due to the variation of LCDs, the resultant membranes exhibit different ion exchange capacity (IEC) values: h@MMT (0.942 mmol g^{-1}) > m@MMT (0.898 mmol g^{-1}) > l@MMT (0.718 mmol g^{-1}) (Figure 3.2k). All MMT membranes presented a relatively smooth surface with few wrinkles and devoid of any cracks or pinholes. The cross-sectional field-emission scanning electron microscopy (FESEM) image demonstrated that MMT membranes showed highly ordered lamellar and homogeneous microstructures (Figure 2 l).

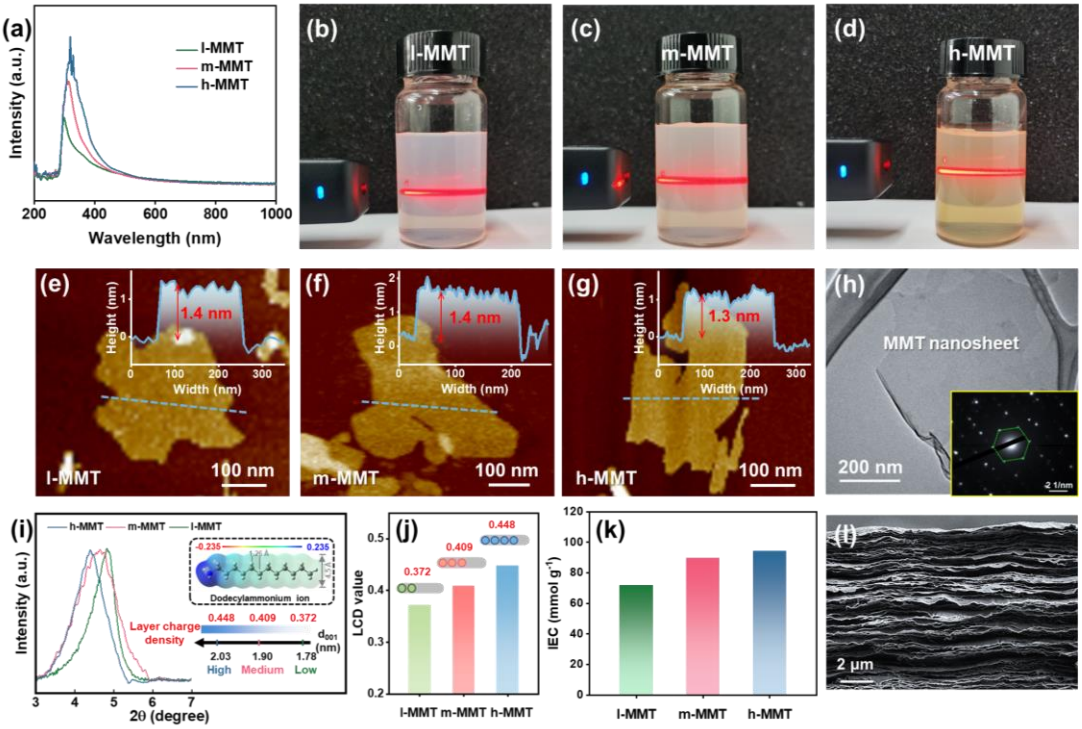


Figure 3.2 (a) UV-vis spectra of the MMT nanosheets. (b-d) Photographs of the MMT nanosheets under a red laser beam. (e-g) AFM images of MMT nanosheets. (h) TEM image and selected area electron diffraction pattern of m-MMT nanosheet. (i) The electrostatic potential distributions of dodecyl trimethyl ammonium chloride and XRD patterns of dodecyl trimethyl ammonium chloride intercalated MMT. (j) The calculated layer charge density of MMT by Weiss equation. (k) IEC values of MMT membranes. (l) The cross-sectional FESEM image of m@MMT membrane.

The high-solution TEM images unveiled the well-defined sub-nanochannels, where the lattice fringes assigned to the (001) plane of MMT membrane with a lattice constant of 1.264 nm were found (Figure 3.3 a-c). The single sharp peak corresponding to the (001) plane was also observed at 2θ of 6.78° in small-angle X-ray diffraction (SAXRD) patterns (Figure 3.3d), suggesting that exfoliation-reassembled MMT

membranes featured aligned lamellar structures with well-defined sub-nanochannels of ~3.50 Å (d-spacing of MMT membrane ≈ 13.1 Å, platelet thickness of MMT ≈ 9.60 Å, i.e., the interlayer free spacing ≈ 3.50 Å) [36,37], Such small sub-nanochannels might be attributed to the unique sheet-ion-sheet attraction interaction between nanosheets with uniformly negatively charged surfaces and interlayer exchangeable cations, which facilitates the orderly arrangement of proton and the formation of short strong H-bonds, providing a proton transport highway. This was confirmed by FTIR spectra, where water presented an absorption bond at ~3510 cm^{-1} corresponding to the H-bond stretching vibration, while was shifted to ~3300 cm^{-1} in MMT membranes, unveiling significantly enhanced H-bond in MMT sub-nanochannels (Figure 3.3e) [11]. Moreover, the horizontal orientation of nanosheets was also characterized by using wide-angle X-ray scattering (WAXS) patterns, in which MMT membranes presented an obvious plane peak and a typical point-shaped diffraction pattern without obvious splitting in the junction zone, illustrating the layer-by-layer assembly and cross-linking effect of preferentially oriented nanosheets along the (001) direction of the c-axis (Figure 3.3f) [38].

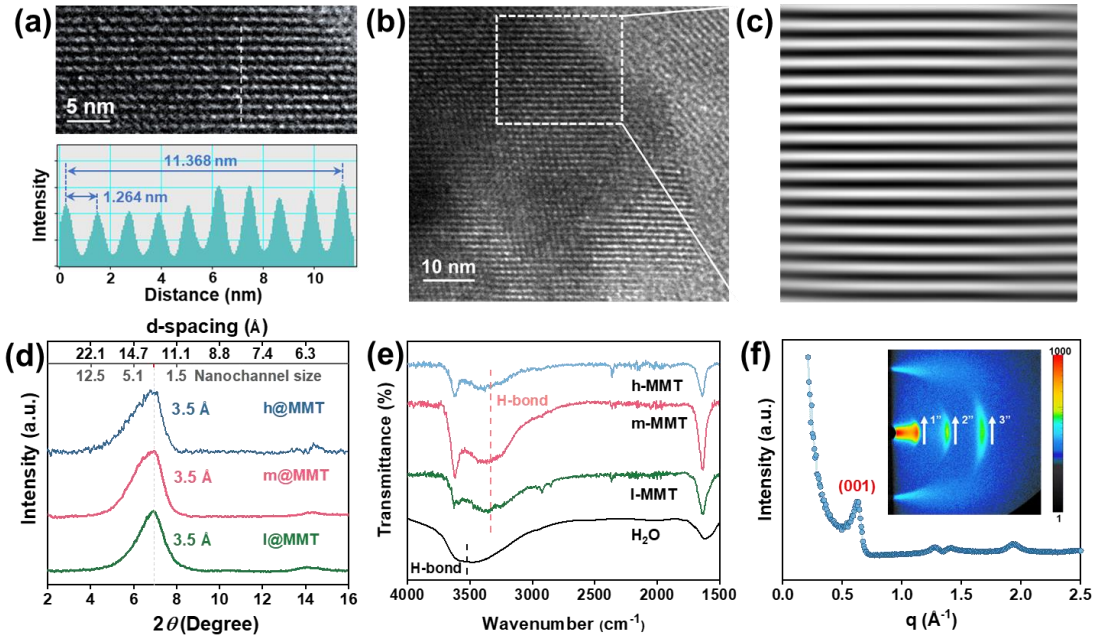


Figure 3.3 (a) The HR-TEM image of m@MMT membrane and the corresponding interlayer spacing between adjacent nanosheets. (b, c) TEM image and the corresponding inverse Fourier transform (IFT) image of the m@MMT membrane. (d) XRD patterns of MMT membranes. (e) FTIR spectra of water and MMT membranes. (f) WAXS diffraction pattern and 2D image of m@MMT membrane.

3.3.2. Layer charge density-dependent ions conductivity

Further, the intrinsic proton transport behaviors in MMT sub-nanochannels were evaluated. The water uptake and anti-swelling behavior is closely related to proton conduction. It is highly desirable to allow water channels to form hydrogen-bond pathways for proton conduction without suffering from performance attenuation due to dimensional swelling of membranes [39]. As displayed in Figure 3.4a, all MMT membranes presented the superior hydrophilicity, which favored absorbing water vapor. Vapor adsorption-desorption curves showed the outstanding water retention capability of MMT membranes under the experimented relative humidity (Figure 3.4b), which was attributed to the capillary effect of sub-nanochannels, favoring proton conductivity. Further, the dimensional stability was also assessed (Figure 3.4c). It could be found that MMT membranes showed excellent dimensional stability with through-plane swelling in the range of 6.1-8.7% and in-plane swelling below 2.7%.

We determined proton conductivities of MMT membranes by impedance measurements using a homemade dual-electrode device. l@MMT, m@MMT and h@MMT exhibited proton conductivities of 9.66, 12.47, and 13.52 mS cm^{-1} at 30 °C, in accordance with the order of their LCD (Figure 3.4d). With rising temperature, their proton conductivities gradually increased and reached maximum values of 45.02, 79.11, and 69.77 mS cm^{-1} at 80 °C. Although slightly inferior to that of commercial Nafion 117 (110.91 mS cm^{-1}), the intrinsic proton conductivities of MMT membranes without external proton carrier groups were very impressive, which was attributed to the formation of short H-bond wire due to aligned sub-nanochannels containing numerous hydroxyl groups, water molecules and protons. This was confirmed by the kinetic isotope effect (KIE), where conductivities of the MMT membrane in H_2O system was 1.49 times higher than that in D_2O system, exceeding the value of $(m_D/m_H)^{0.5}$, which unveiled the proton transport governed by Grotthuss mechanism (Figure 3.4e). We also found the delay in proton conductivities of MMT membranes when the relative humidity decreased from 98% to 30% RH, which resulted from the reduction of water molecules required for constructing H-bond networks (Figure 3.4f) [40].

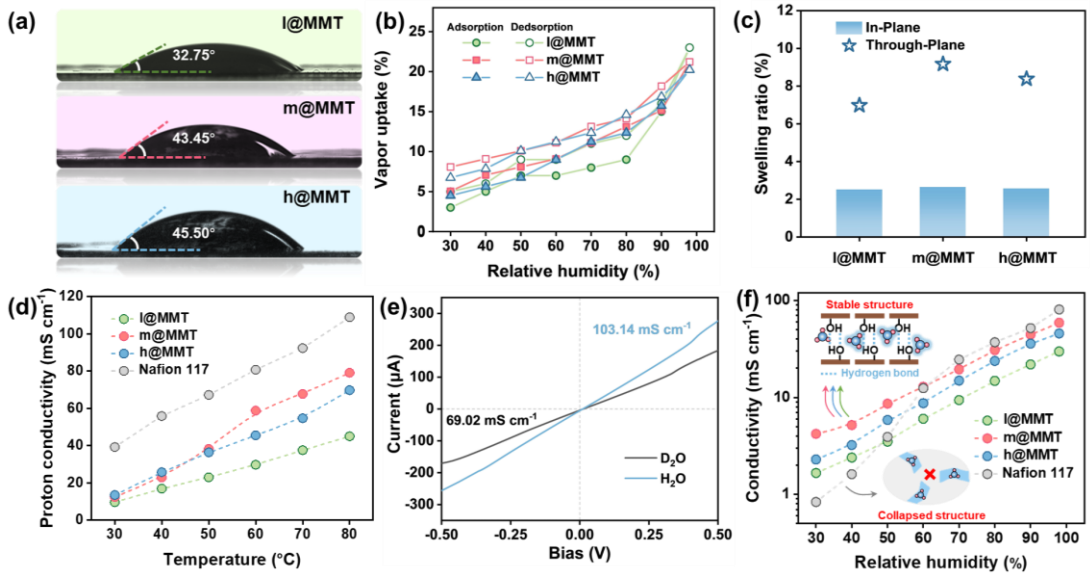


Figure 3.4 (a) The initial water contact angle images of MMT membranes. (b) Humidity-dependent vapor adsorption-desorption curves of MMT membranes. (c) The dimensional swelling of MMT PEM at 80°C and 98% RH. (d) The proton conductivity of Nafion 117 and MMT membranes at 98% RH with different temperatures. (e) The *I/V* curves of the MMT membranes recorded in HCl-D_2O and HCl-H_2O solution of 0.1 mol L^{-1}. (f) The proton conductivity of Nafion 117 and MMT membranes at 60 °C with different humidities.

Notably, the conductivity decline of Nafion 117 was more dramatic due to its transport channel shrinkage and collapse [41], surpassing that of MMT by almost one order of magnitude. The conductivities of MMT membranes were 2-5 times higher than that of Nafion under ultra-low humidity of 30% RH, which was contributed to water locking effect of stable sub-nanochannel capillaries (Figure 3.5a-c), demonstrating the potential as promising PEMs. We collected the swelling ratio values and proton conductivities of recently reported PEMs under comparable test conditions and IEC values (Figure 3.5d). Encouragingly, MMT membranes showed well-balanced performance due to the unique chemical microenvironment and spatial microstructure. We also evaluate the conductivity stability of sub-nanochannels. MMT membranes showed the unaffected proton conductivity during the continuous cooling-heating cycle of 100 h, suggesting the long-term stability and durability (Figure 3.5e). Beyond that, whether in organic solvents, annealed at 300 °C or defrosted at -20 °C, MMT membranes demonstrated excellent durability with almost overlapping Nyquist plots of impedance data, slow weight loss and intact microstructures (Figure 3.5f-h), which is difficult to achieve with Nafion, emerging organic framework-based and graphene-

based membranes. Surprisingly, we observed that proton conductivities of MMT membranes were not positively correlated to LCDs. Specifically, the m@MMT exhibited a higher proton conductivity than that of h@MMT at the high-temperature range, despite the worth noting lower IEC value and surface charge than the latter, which was incompatible with our common cognition. Such phenomena suggested that the augmentation of LCDs, although it improved IECs of membranes and hence favored proton transport, might affect the spatial microstructures of the nanosheets within the membrane, which ultimately exhibited a “volcanic” tendency of proton conductivity (Figure 3.5i).

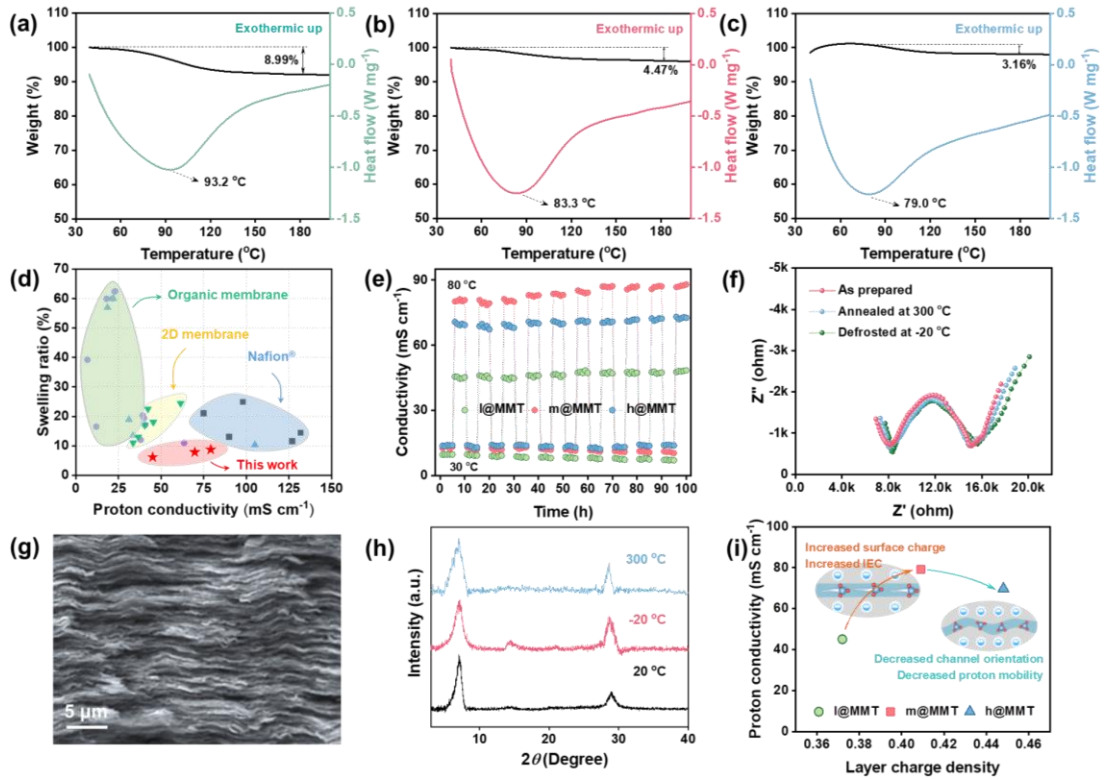


Figure 3.5 Thermogravimetric (TG) analysis and differential scanning calorimetry (DSC) patterns of (a) l@MMT, (b) m@MMT, and (c) h@MMT treated at 30% RH and 30 °C for 24 h. (d) Swelling ratio versus proton conductivity from MMT membranes and state-of-the-art PEMs reported in the literature. (e) Conducting stability of MMT membranes under the cooling-heating cycle from 30 to 80 °C at 98% RH. (f) Nyquist plots of m@MMT before and after annealing at 300 °C and defrosting at -20 °C for 12h under 98% RH and 80 °C. (g) Cross-section SEM images of MMT membrane at 300 °C and defrosting at -20 °C for 12h. (h) XRD patterns of h@MMT before and after annealing at 300 °C and defrosting at -20 °C for 12h. (i) The relationship between proton conductivity of MMT membranes and the layer charge density.

3.3.3. Ion transport mechanisms modulated by LCD in 2D sub-nanochannels

Therefore, we used 2D-WAXS measurements to profile the structural difference arising from stacking of nanosheets with different LCDs. Accordingly, a more dispersed and weaker scattering for the (001) plane of the MMT membrane was observed as LCD increased (Figures 3.6a-c). To quantitatively compare the nanosheets alignment in membranes, WAXS data was converted to 1D azimuthal plots, in which h@MMT exhibited a broader and more dispersed azimuthal distribution with the larger full width at half peak (FWHM) of 36.9°. Meanwhile, we also quantified the degree of the horizontal orientation of MMT nanosheets in membranes using the Herman's orientation facter (*f*), where h@MMT exhibited the lowest level of alignment ($f = 0.94$) [31]. These results suggested that the nanosheets became less oriented within the membrane with increasing LCD, which was detrimental to proton transport. Such outcomes were consistent with the results of FWHM in SAXRD patterns (Figure 3.6g). Also, both the AFM images and the corresponding zoning images intuitively showed the topographical differences between MMT membranes, where the membranes became more undulated and rougher with increasing LCD (Figure 3.6d-f). The results could be explained by the fact that the increased LCD would inevitably cause the soared surface charge of MMT nanosheets, strengthening electrostatic repulsion between nanosheets, discouraging self-assembly of nanosheets into sub-nanochannels. According to the Laplace pressure (equation 3.13), $cos\ \theta_\alpha$ is proportional to surface radius of membrane (R) owing to the almost constant Δp for three membranes [42].

$$P_c = \Delta p = -2\gamma\ cos\ \theta_\alpha\ /\ R \tag{3.13}$$

where P_c is the capillary driving pressure; γ refers the surface tension of water. Because of the high hydrophilicity of MMT membranes ($\theta_\alpha < 90°$), that is, the value of $cos\ \theta_\alpha$ decreases with $\theta\alpha$ increasing, suggesting that the higher θ, the smaller R of the membrane. The results reconfirmed the reduced orientation of MMT sub-nanochannels as LCDs increased (Figure 3.6h).

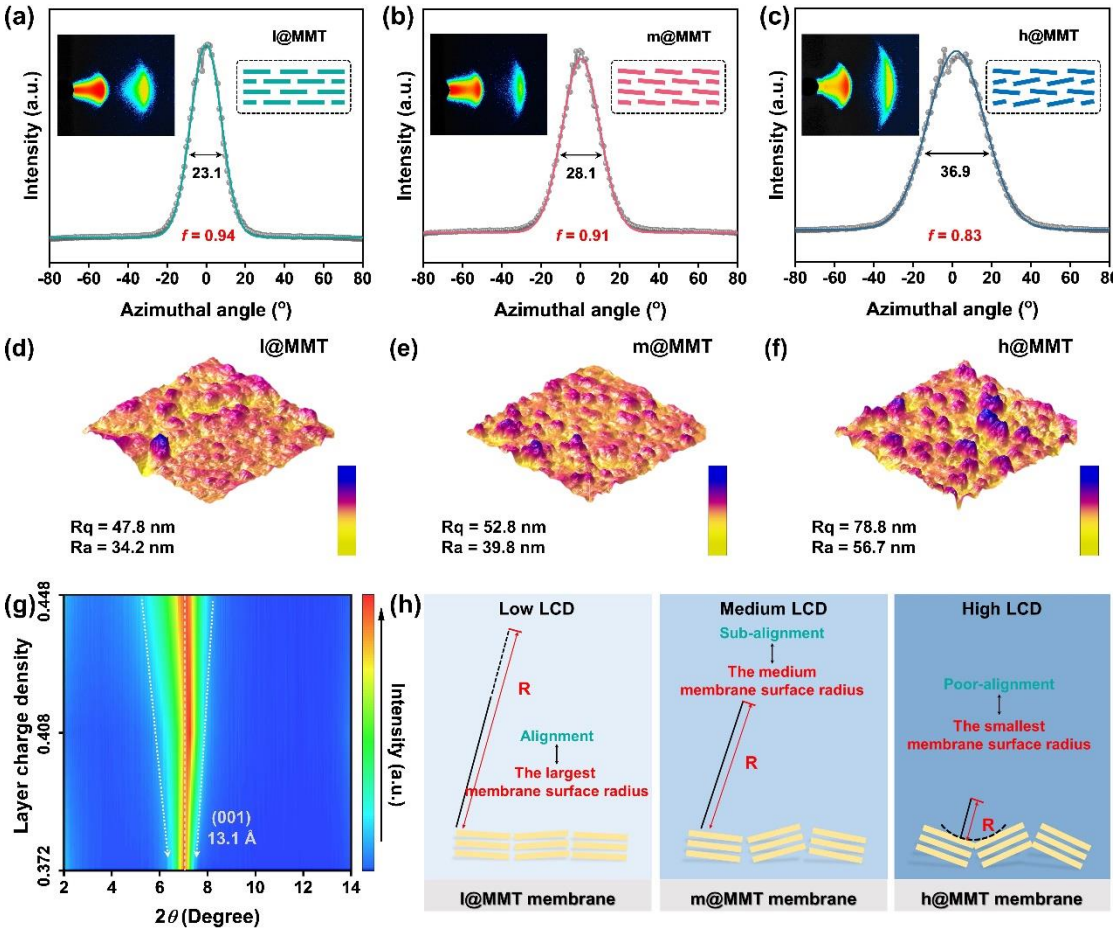


Figure 3.6 (a-c) WAXS patterns for an incident Cu Kα x-ray beam parallel and corresponding azimuthal scan profiles of MMT membranes. (d-f) AFM images and roughness analysis of MMT membranes. (g) Contour plots of SAXRD patterns of MMT membranes. (h) Schematic of the surface radius of MMT membranes.

In order to thoroughly reveal the roles of LCD control in the modulation of proton transport within sub-nanochannels, we comprehensively investigated the effect on the chemical microenvironment and spatial microstructure of MMT membranes. Generally, proton transfer within PEMs through dissociation and movement of hydrated hydrogen ions, which is dominated by Grotthuss and Vehicle mechanisms, thus H^+ concentration and effective mobility play critical roles [43]. For nanochannel membranes, moreover, when the electrical double layer (EDL) thickness (Debye length, λ_D) of nanosheets can completely overlap the channels size, the proton transport within nanochannel is also controlled by the surface-charge-governed transporting mechanism [44,45]. According to IEC and water uptake of membranes, the H^+ concentration within nanochannels was calculated to be 0.77 to 1.91 mmol cm^{-3} (Figure 3.7a). Further, the double λ_D of nanosheets in MMT membranes was determined in the range of 4.4 to 6.9 Å based on

Debye-Hückel equation, which were larger than the channels size (3.5 Å). It can be concluded that proton transport in all the sub-nanochannels occurred under the overlapping EDL region. Thus, the proton conductance in the sub-nanochannels included the contribution of Grotthuss- and Vehicle-driven channel conductance (σ_c) and surface charge determined conductance (σ_{scd}). The proton conductivity (σ) can be accessed as [30,46]:

$$\sigma = \sigma_c + \sigma_{scd} \tag{3.14}$$

$$\sigma_{scd} = 2\mu z_{scd}(w/l) \tag{3.15}$$

where z_{scd} (mC m^{-2}) is the surface charge density of nanosheets; l (cm) and w (cm) are the length and width of channels, respectively. The proton conductivity is positively related with proton concentration and surface charge density (z_{scd}) of nanosheets. Specifically, the increase in LCDs would cause increased IEC and hence proton concentration (Figure 3.5a), improving the channel bulk conductance. Also, z_{scd} would increase with the increasing LCDs (Figure 3.7b), facilitating surface charge determined conductance. Therefore, the proton conductivity of m@MMT was higher than that of l@MMT.

Additionally, the proton conductivity is closely dependent on the effective mobility (μ, m^2 s^{-1} V^{-1}) of H^+ following the Nernst-Einstein relationship ($\sigma = Fa\mu$, where F is Faraday's constant and a is ion concentration) [47]. The effective mobility refers to the average speed of ions within channels, demonstrating the intrinsic mobility of ions and the morphological properties of channels (including channel tortuosity, connectivity, and spatial proximity of neighboring ion groups, and so forth). Unexpectedly, the effective mobility of protons showed the opposite behavior to LCDs, *i.e.,* the effective mobility of h@MMT was the lowest among all the membranes (Figure 3.7c). This might ascribe to the decreased channel orientation and connectivity of MMT membranes with increasing LCDs (Figure 3.6), consequently resulting in a lower conductivity of h@MMT than that of m@MMT.

We demonstrated the effect of orientation degree of sub-nanochannels on effective mobility behavior of proton by molecular dynamic (MD) simulations, where two typical well-ordered and poor-ordered channels were modeled, labeled as l@MMT and h@MMT, respectively. The mean square displacement (MSD) curves of hydrated proton (H_3O^+) and H_2O molecule within MMT membranes were exhibited in Figure 3.7d and f. It can be found that the transport rates of both protons and H_2O were linearly

related to the simulation time, suggesting the existence of stable and continuous water transport channels, and the rates in l@MMT significantly exceeded those in h@MMT. The corresponding diffusion coefficients obtained from slopes of the MSD curves revealed that l@MMT with aligned sub-nanochannels features a more hydrophilic microenvironment (Figure 3.7g), favoring the Grotthuss mechanism for the faster mobility and transport of protons, which was consistent with the results of previous reports [48].

Further, we carried out a detailed study of proton concentration and mobility for different LCDs to deeply unveil the anomalies affected by LCDs. Through the established linear analysis between LCDs and proton concentration as well as effective mobility, it is clear that as the nanosheet LCD increases, the proton concentration (a) increases, while the channel orientation and effective mobility (μ) decreases, presenting distinct competitive relation (Figure 3.7h). The pristine state describes the case of MMT without exchangeable ions in the interlayer, in which the LCD is 0, whose proton conductivity is not available. States 1-3 feature low LCDs, representing the slightly stronger concentration-improving effect than mobility-diminishing effect, contributing increased proton conductivity. State 4 refers to an optimum LCD that concentration-improving effect dominates over mobility-diminishing effect, allowing much enhanced proton conductivity. State 5 stands for the cases with high LCD, where the mobility-diminishing effect becomes intensified more than concentration-improving effect, thus the conductivity tends to decrease. A comprehensive schematic was given in Figure 3.7i to visualize the competition between the concentration-improving effect and mobility-diminishing effect. Therefore, taking into account the proton concentration, surface charge, and proton mobility, m@MMT with a moderate LCD exhibited the highest proton conductivity (Figure 3.5i).

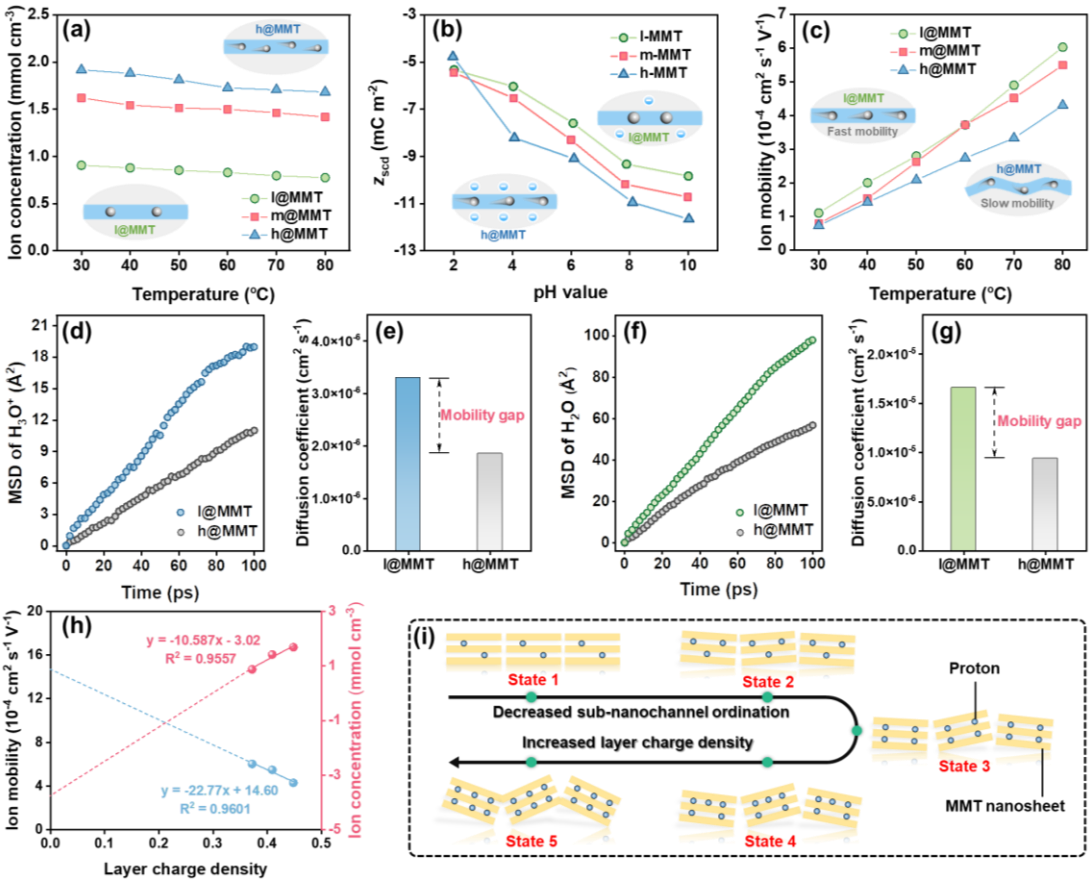


Figure 3.7 (a) Proton concentrations and (c) effective mobilities in within membranes at 98% RH with different temperatures. (b) Surface charge densities of MMT membranes under different pH values. Mean square displacement (MSD) curves of (d) protons and (f) H_2O molecules within MMT membranes. Diffusion coefficients of (e) protons and (g) H_2O molecules within MMT membranes. (h) Relationship between layer charge density and proton concentration as well as effective mobility. (i) Schematic of sub-nanochannels with different LCDs.

3.4. Conclusions

In summary, inspired by biological proton channels, we developed biomimetic sub-nanochannels arrays via restacking of exfoliated nanoclays. The as-assembled atomically small hydrophilic capillaries of ~3.5 Å yielded fast and robust proton highways. The spatial microstructure, proton concentration, and electrostatic effect of sub-nanochannels were readily tuned by modulating the intrinsic LCD properties of nanosheets. Characterization and simulations demonstrated that controlling the LCD to construct well-ordered sub-nanochannels with considerable proton concentration was the key for efficient proton transport. Consequently, the optimal membranes without

external proton carriers presented a superior proton conductivity of 79.11 mS cm^{-1} and long-term operational stability. Such strategy is cost-effective and sustainable, facilitates additional modification and thus, holds promise in scalability.

3.5. References

[1] Wiley B, Largo E, Nabais L, et al. Structural Bases for the Unconventional Activity of a Viroporin Channel. Biochemistry, 2026, 65(13): 2108.

[2] Zhu L, Ye P, Zhang L, et al. Bioinspired heterogeneous construction of lignocellulose-reinforced COF membranes for efficient proton conduction. Small, 2024, 20(3): 2304575.

[3] Cai L, Yang J, Lai Y, et al. Dynamics and proton conduction of heterogeneously confined imidazole in porous coordination polymers. Angewandte Chemie, 2023, 135(10): e202211741.

[4] Qian Y, Wu Y, Qiu S, et al. A Bioinspired Free-Standing 2D Crown-Ether-Based Polyimine Membrane for Selective Proton Transport. Angewandte Chemie International Edition, 2023, 62(18): e202300167.

[5] Hou X, Guo W, Jiang L. Biomimetic smart nanopores and nanochannels. Chemical Society Reviews, 2011, 40(5): 2385-2401.

[6] Tunuguntla R H, Allen F I, Kim K, et al. Ultrafast proton transport in sub-1-nm diameter carbon nanotube porins. Nature nanotechnology, 2016, 11(7): 639-644.

[7] DeCoursey T E, Hosler J. Philosophy of voltage-gated proton channels. Journal of The Royal Society Interface, 2014, 11(92): 20130799.

[8] Li Q, Gao H, Zhao Y, et al. Covalent organic framework interlayer spacings as perfectly selective artificial proton channels. Angewandte Chemie International Edition, 2024, 63(23): e202402094.

[9] Xu W, Wang Y, Wu Y, et al. Sub-2-nm channels within covalent triazine framework enable fast proton-selective transport in flow battery membrane. Advanced Functional Materials, 2023, 33(21): 2300138.

[10] Yang P, Xu L, Trogadas P, et al. Bioinspired supramolecular macrocycle hybrid membranes with enhanced proton conductivity. Nano Research, 2024, 17(2): 797-805.

[11] Shi B, Pang X, Li S, et al. Short hydrogen-bond network confined on COF surfaces enables ultrahigh proton conductivity. Nature Communications, 2022, 13(1): 6666.

[12] Shen J, Ye R, Liu Z, et al. Hybrid Pyridine–Pyridone Foldamer Channels as M2-Like Artificial Proton Channels. Angewandte Chemie International Edition, 2022, 61(28): e202200259.

[13] Yan T, Liu S, Xu J, et al. Unimolecular Helix-Based Transmembrane Nanochannel with a Smallest Luminal Cavity of 1 Å Expressing High Proton Selectivity and Transport Activity. Nano Letters, 2021, 21(24): 10462-10468.

[14] Tian M, Liu Y, Zhang S, et al. Overcoming the permeability-selectivity

challenge in water purification using two-dimensional cobalt-functionalized vermiculite membrane. Nature communications, 2024, 15(1): 391.

[15] Shi B, Pang X, Lyu B, et al. Spacer-Engineered Ionic Channels in Covalent Organic Framework Membranes Toward Ultrafast Proton Transport. Advanced Materials, 2023, 35(16): 2211004.

[16] Xu R, Kang Y, Zhang W, et al. Two-dimensional MXene membranes with biomimetic sub-nanochannels for enhanced cation sieving. Nature Communications, 2023, 14(1): 4907.

[17] Kang Y, Xia Y, Wang H, et al. 2D laminar membranes for selective water and ion transport. Advanced Functional Materials, 2019, 29(29): 1902014.

[18] He G, Xu M, Zhao J, et al. Bioinspired ultrastrong solid electrolytes with fast proton conduction along 2D channels. Advanced Materials, 2017, 29(28): 1605898.

[19] Solangi N H, Mubarak N M, Karri R R, et al. Recent development of graphene and MXene-based nanomaterials for proton exchange membrane fuel cells. International Journal of Hydrogen Energy, 2024, 73: 905-931.

[20] Qin R, Tang J, Wu C, et al. Nanofiber-reinforced clay-based 2D nanofluidics for highly efficient osmotic energy harvesting. Nano Energy, 2022, 100: 107526.

[21] Tang J, Wang Y, Yang H, et al. All-natural 2D nanofluidics as highly-efficient osmotic energy generators. Nature Communications, 2024, 15(1): 3649.

[22] Shao J J, Raidongia K, Koltonow A R, et al. Self-assembled two-dimensional nanofluidic proton channels with high thermal stability. Nature communications, 2015, 6(1): 7602.

[23] Guan Q F, Yang H B, Han Z M, et al. An all-natural bioinspired structural material for plastic replacement. Nature communications, 2020, 11(1): 5401.

[24] Cao L, Wu H, He X, et al. Flexible, transparent ion-conducting membranes from two-dimensional nanoclays of intrinsic conductivity. Journal of Materials Chemistry A, 2019, 7(44): 25657-25664.

[25] Jiang X, Zhang L, Miao Y, et al. Intrinsic roles of nanosheet characteristics in two-dimensional montmorillonite membranes for efficient Li^{+}/Mg^{2+} separation. Water Research, 2025, 276: 123291.

[26] Gogoi R K, Raidongia K. Strategic shuffling of clay layers to imbue them with responsiveness. Advanced Materials, 2017, 29(24): 1701164.

[27] Zou Y C, Mogg L, Clark N, et al. Ion exchange in atomically thin clays and micas. Nature materials, 2021, 20(12): 1677-1682.

[28] Zheng Y, Zhou Z, Jiao M, et al. Lamellar membrane with orderly aligned glycine molecules for efficient proton conduction. Journal of Membrane Science, 2023, 672: 121433.

[29] Zhong L, Hu S, Yang X, et al. Difference in the preparation of two-dimensional nanosheets of montmorillonite from different regions: Role of the layer charge density. Colloids and Surfaces A: Physicochemical and Engineering Aspects, 2021, 617: 126364.

[30] Wei C, Zhou Y, Yang X, et al. Parallel arrays of clay nanosheets sandwiched in two-dimensional nanofluidic membrane for enhanced ion transport properties. Journal of Membrane Science, 2023, 680: 121744.

[31] Yang J, Li M, Fang S, et al. Water-induced strong isotropic MXene-bridged graphene sheets for electrochemical energy storage. Science, 2024, 383(6684): 771-777.

[32] Li Z, Wang W, Chen Y, et al. Constructing efficient ion nanochannels in alkaline anion exchange membranes by the in situ assembly of a poly (ionic liquid) in metal–organic frameworks. Journal of Materials Chemistry A, 2016, 4(6): 2340-2348.

[33] Sun Q, Ma H, Wu L, et al. Molecular simulation for guiding the design and optimization of mixed matrix membranes (MMMs) in the pervaporation process. Langmuir, 2023, 39(14): 5199-5210.

[34] Kong Y, Lyu B, Fan C, et al. Manipulation of cationic group density in covalent organic framework membranes for efficient anion transport. Journal of the American Chemical Society, 2023, 145(51): 27984-27992.

[35] Olis A C, Malla P B, Douglas L A. The rapid estimation of the layer charges of 2: 1 expanding clays from a single alkylammonium ion expansion. Clay Minerals, 1990, 25(1): 39-50.

[36] Zhang T, Ren B, Bai H, et al. Subnanometer-scale control of channel height in two-dimensional montmorillonite membrane for ion separation. Journal of Membrane Science, 2023, 675: 121573.

[37] Ding L, Li L, Liu Y, et al. Effective ion sieving with $Ti_3C_2T_x$ MXene membranes for production of drinking water from seawater, Nature Sustainability, 2020, 3(4): 296-302.

[38] Xin W, Lin C, Fu L, et al. Nacre-like mechanically robust heterojunction for lithium-ion extraction. Matter, 2021, 4(2): 737-754.

[39] He X, Yang Y, Wu H, et al. De novo design of covalent organic framework membranes toward ultrafast anion transport. Advanced Materials, 2020, 32(36): 2001284.

[40] Lin S, Kedzior S A, Zhang J, et al. A superprotonic membrane derived from proton-conducting metal-organic frameworks and cellulose nanocrystals. Chem, 2023, 9(9): 2547-2560.

[41] Cao L, Wu H, Cao Y, et al. Weakly humidity-dependent proton-conducting COF membranes. Advanced Materials, 2020, 32(52): 2005565.

[42] Yang H, Yang L, Wang H, et al. Covalent organic framework membranes through a mixed-dimensional assembly for molecular separations. Nature communications, 2019, 10(1): 2101.

[43] Luduena G A, Kühne T D, Sebastiani D. Mixed Grotthuss and vehicle transport mechanism in proton conducting polymers from ab initio molecular dynamics simulations. Chemistry of Materials, 2011, 23(6): 1424-1429.

[44] Siria A, Bocquet M L, Bocquet L. New avenues for the large-scale harvesting of

blue energy. Nature Reviews Chemistry, 2017, 1(11): 0091.
[45] Wen T, Zhao Y, Wang X, et al. Efficient and ultrafast separation of Li+ and Mg2+ by the porous two-dimensional nanochannel of perm-selective montmorillonite membrane. Chemical Engineering Journal, 2023, 475: 146101.
[46] Wu X, Chen W, Yan X, et al. Enhancement of hydroxide conductivity by the di-quaternization strategy for poly (ether ether ketone) based anion exchange membranes. Journal of Materials Chemistry A, 2014, 2(31): 12222-12231.
[47] Peckham T J, Holdcroft S. Structure-morphology-property relationships of non-perfluorinated proton-conducting membranes. Advanced Materials, 2010, 22(42): 4667-4690.
[48] Yu W, Zhang K, Zhang J, et al. Efficient lamellar two-dimensional proton channels derived from dipole interactions in a polyelectrolyte membrane. AIChE Journal, 2022, 68(8): e17731.

This chapter was published in ACS Materials Lett., 2025, 7, 2835-2843. (JCR Q1).

Chapter 4.

A Dual-constrained Assembly Strategy of Highly Aligned Two-dimensional Montmorillonite Membrane For Efficient Proton Transport

Chapter 3 showed that the alignment of MMT nanosheets is a key factor for fast proton transport. This chapter therefore seeks to improve channel alignment during membrane assembly. MMT nanosheets are modified with sulfonated poly(vinyl alcohol) (SPVA), which acts both on the dispersion of the nanosheets and on their stacking during drying (the dual-constrained assembly strategy).

4.1. Introduction

Efficient transport of proton through proton exchange membranes (PEMs) plays a crucial role in biological processes, and energy storage/conversion devices [1–3]. Currently, commercially available PEMs such as Nafion membranes face great challenges of severe decline in conductivity and efficiency due to ready dehydration under high temperature and/or low humidity [4,5]. In contrast to amorphous polymers, nanofluidic channels constructed using two-dimensional (2D) nanosheets exhibited excellent stability, and the huge capillary-like force created inside nanochannels can substantially facilitate proton transport, which enables them to be considered as promising candidates for PEMs [6–8]. Notably, the fast proton transport in aqueous systems is usually governed by the Grotthuss mechanism that occurs on the hydrogen bond networks and induces a collective proton motion analogous to a Newton's cradle [9,10]. Such Grotthuss-type proton transport mainly depends on proton bridging of continuous hydrogen bonds, making it important to construct well-aligned nanofluidic channels [11].

The high aspect ratio (i.e. the ratio of lateral size to thickness) of nanosheets enables them to spontaneously and preferentially stack by face-to-face to form lamellar nanochannel structure, however, the edge-to-edge interactions between randomly spatially oriented nanosheets in suspension inevitably cause undesirable pre-assembly of 2D building blocks [12–14]. Subsequent the pre-assembled nanochannels are removed water to enhance stacking of nanosheets and assemble lamellar membranes

[15]. During the assembly process, the capillary forces drive the lateral contraction of nanosheets, resulting in further deterioration of the nanochannel alignment [16–18], which fails to fully exploit the proton transport potential of nanofluidic channels of lamellar membranes. Therefore, it is imperative to regulate the stacking and assembly behaviors of nanosheets to construct highly aligned and ordered nanofluidic channels for optimizing proton transport in PEMs.

Currently, several strategies have been developed to fabricate lamellar membrane with highly aligned nanochannels, which mainly involve: i) enhancement in spatial orientation of nanosheet dispersion [14,19,20], ii) optimization in assembly approaches of nanosheets [21–23], and iii) externally assisted nanosheet alignment [24–26]. Based on these strategies, methods such as nanosheet property modulation, shear-induced ordered assembly, chemical cross-linking, and stretch-induced alignment, have been developed. While these methods are able to improve the alignment of nanochannels to some extent, are limited by the complex procedures or negative effects on ion transport [27]. Tailoring nanosheets to nanofluidic channels with high alignment and rapid proton transport properties through facile and scalable way is still very challenging.

Herein, we proposed a dual-constrained assembly strategy that strengthened electrostatic confinement effect between nanosheets and offered capillary force compensation effect to construct highly aligned nanofluidic channels for efficient proton transport. Montmorillonite (MMT), a natural layered silicate mineral, was selected to represent 2D nanomaterials due to abundant reserves and exceptional stability [28,29]. The exfoliated MMT nanosheets were modified with sulfonated polyvinyl alcohol (SPVA), where SPVA acted as a negatively charged coating, cross-linking agent and proton carrier. Consequently, SPVA-modified MMT (SMMT) nanosheets featured the higher negative charge to enhance the electrostatic repulsion and thereby constrain the edge-to-edge interactions, contributing the improved spatial orientation degree of nanosheets dispersion. During the assembly process, hydrogen bond interaction between SPVA and MMT nanosheets generated tensile forces to compensate for capillary forces, thus restraining the nanochannels disordering. Further, SPVA provided additional sulfonic acid groups within the aligned nanochannels to enhance Grotthuss proton transport mechanism. Benefiting from the dual-constrained assembly strategy, the prepared SMMT membrane presented ultra-high proton conductivity of 134.58 mS cm^{-1} at 30 °C, ultra-low activation energy of 9.19 kJ mol^{-1}, and outstanding stability. This work provided a universal and scalable strategy for

constructing advanced PEMs, which can be extended to the development and design of other aligned 2D lamellar membranes.

4.2. Experimental section

4.2.1. Material synthesis

Materials: Natural MMT was obtained from Xinjiang, China. Poly (vinyl alcohol) (PVA, Mw 200000) and disodium 4-formyl-1,3-benzenedisulfonate (BADSA, 37%) were purchased from Sinopharm Chemical Reagent Co., Ltd. Sodium chloride (NaCl, ≥ 99%), potassium chloride (KCl, ≥ 99%), and hydrochloric acid (HCl, 37%) were purchased from Shanghai Aladdin Biochemical Technology Co., Ltd.

Preparation of SMMT nanosheets and membranes: Dispersion of MMT nanosheets was prepared according to our previous report, including purification, ion exchange and exfoliation. Briefly, the raw MMT mineral was crushed, cleaned and centrifuged at high speed to remove impurities. The resulting MMT suspension was then ion exchanged with NaCl to prepare Na-based MMT and then was exfoliated by sonication (output power of 450 W) to obtain MMT nanosheets. Further, sulfonated polyvinyl alcohol (SPVA) equivalent to 15% of the mass of MMT nanosheets was taken and homogeneously mixed with MMT nanosheets for 24 h to obtain SPVA-modified SMMT nanosheets. MMT and SMMT membranes were assembled by vacuum filtration of the nanosheet dispersion using a PES filter (4.0 cm diameter, 0.02 μm pore size, Whatman). The MMT membrane was easily peeled off from the filter membrane after natural air drying. The obtained MMT membrane are white and translucent, and could be easily cut into the required shapes using a razor blade. Large scale membranes were prepared using a PES filter of 10 mm diameter.

Preparation of Sulfonated polyvinyl alcohol (SPVA): The SPVA was prepared via an acid-catalyzed reaction between PVA and BADSA [30]. The specific experimental procedure was as follows: BADSA (50 mmol) and HCl solution (10 mL, 1 mol L^{-1}) were added to aqueous PVA solution (100 mL, 5 wt%). The reaction was carried out in a water bath at 60 °C for 96 h. The product was then precipitated in excess ethanol. Finally, the resulting white precipitates were washed three times with anhydrous ethanol and dried in a blast oven at 60 °C for 36 h to obtain SPVA.

Preparation of the nanofluidic devices: The MMT and SMMT membranes were cut into rectangular pieces and immersed into a mixture of polydimethylsiloxane (PDMS) and curing agent to cure. Two reservoirs were excavated in the area at the ends

of the membrane to expose the membrane to the electrolyte solutions. Before each test, the conduit device was immersed in a certain concentration of electrolyte for 24 h to ensure fully hydration of the nanochannels. Two Ag/AgCl electrodes used as the working electrode and reference electrode were inserted into the source and drain reservoirs to measure the ion current of the MMT conduits at different electrolyte concentrations.

4.2.2. Characterizations

The thickness of the nanosheets and the surface roughness of the membranes were measured by atomic force microscopy (AFM, Multimode 8). The morphologies of nanosheets and membranes were obtained by scanning electron microscopy (SEM, Gemini SEM 300). Malvern Zetasizer Zeta Nano (Malvern) was used to measure the zeta potential of the MMT colloidal dispersion. The X-ray Diffraction (XRD) pattern of membranes was performed by the powder X-ray diffraction (RU-200B/D/MAX-RB, Rigaku, Japan) with a Cu Kα radiation. The nanosheet stacking within membranes was investigated by a wide-angle X-ray scattering (WAXS, Xeuss 2.0) with Cu Kα radiation (λ=1.54189Å). Polarized optical microscopy (POM, Leica DM6 M) was used to observe the birefringence and dispersion degree of nanosheets and membranes. The tensile properties of membranes were measured on an Instron 5967 Tester. The X-ray Photoelectron Spectroscopy (XPS) was carried out by X-ray photoelectron spectroscopy ESCALAB 250Xi, Thermo Fisher Scientific, USA) for exploring the inner chemistry of nanosheets and membranes. The chemical composition and molecular structure of SPVA were analyzed by Fourier transform infrared spectroscopy (FTIR, Nicolet 6700, Thermofisher) and nuclear magnetic resonance (NMR, Bruker AVANCE III spectrometer).

4.2.3. Conductivity measurement of membranes

The proton conductivity of membranes was determined based on *I-V* tests. Specifically, the linear scan voltammetry (LSV) method was applied to measure the I-V curves of proton transport through nanochannels at a scanning voltage from -0.5 V to 0.5 V with the scanning rate of 0.01 V s^{-1}. The ion conductivity (σ, S cm^{-1}) of the membrane at different electrolyte concentrations could be calculated according to the following equation:

$$\sigma = Kl/wh \tag{4.1}$$

where *l* (cm), *w* (cm), and *h* (cm) are the length, width and height of the MMT channel, respectively. *K* refers to the slope of the *I-V* curves.

The activation energy (*Ea*) values for the MMT and SMMT membranes were obtained by least square fitting of the Arrhenius diagram. *Ea* was calculated using the following equation:

$$\sigma = \frac{\sigma_0}{T} \exp\left(\frac{-E_a}{kT}\right) \tag{4.2}$$

where σ_0 stands for the preexponential factor; *k* and *T* are the Boltzmann constant and the absolute temperature in kelvin, respectively.

4.2.4. Liquid nitrogen transient freeze-drying treatment

The MMT and SMMT nanosheet dispersions were magnetically stirred for 24h, respectively, to ensure uniform dispersion. The uniformly dispersed nanosheets were left to stand for 48 h, then poured onto aluminum disks, which were subsequently immersed in liquid nitrogen for transient freezing. Further, the frozen samples were freeze-dried for 24 h (-60 °C, 0.011 mBar). Finally, the suspension states of MMT and SMMT nanosheets were observed by scanning electron microscopy (SEM).

4.2.5. Orientation factor calculation

The orientation factor (*f*) was used to describe the orientation degree of the nanosheets within the membranes. Its range of values is from 0 to 1, with larger values resulting in more consistent relative orientations [22]. The Hermans orientation function was used to fit the azimuthal profile:

$$f = \frac{1}{2}(3\langle\cos^2\theta\rangle - 1) \tag{4.3}$$

$$\langle\cos^2\theta\rangle = \frac{\int_0^{\pi/2} I(\theta)\cos^2\theta\sin\theta\,d\theta}{\int_0^{\pi/2} I(\theta)\sin\theta\,d\theta} \tag{4.4}$$

where $I(\theta)$ refers the azimuthal dependence of the X-ray scattered intensity.

4.2.6. Ion exchange capacity determination

The ion exchange capacity (IEC) value of membranes was measured using a titration method [31]. Briefly, the dried membranes (0.2 g) were immersed in NaCl solution (0.1 g mL^{-1}, 20 mL) and stirred for 24 h to allow complete replacement of Na^+ and H^+. The solution was then titrated with 0.01 M NaOH solution, with phenolphthalein as an indicator. The IEC value (mmol g^{-1}) was defined as:

$$\mathrm{IEC} = \frac{0.01 \times V_{NaOH}}{W_{dry}} \times 1000 \quad (4.5)$$

where V_{NaOH} (L) is the consumed volume of the NaOH solution; W_{dry} (g) is the weight of the membrane.

4.2.7. Degree of sulfonation determination

The sulfonation degree (Ds) of the prepared SPVA is accurately determined by ^{1}H NMR. Specifically, the Ds is calculated based on the ratio of the integral areas of the methyl hydrogen atoms (Hp) and methylene hydrogen atoms (H_n) connected to the benzene ring on the hexagonal ring in the PVA chain repeat units, which can be calculated using the following equation.

$$\mathrm{Ds} = \frac{2A_{(Hp)}}{A_{(Hn)}} \times 100\% \quad (4.6)$$

4.2.8. Theoretical calculations

The density functional theory (DFT) calculations were carried out by the Materials Studio 8.0 software. The exchange-correlation interactions were described by the Perdew-Burke-Ernzerhof generalized gradient approximation (GGA-PBE) for structure optimization to minimize the energy. The cut-off energy was set to 580 eV and the k-point mesh with a size of 3 × 1 × 1 grid was used. The convergence criteria for energy, displacement, and force were 1×10^{-5} eV/atom, 0.001 Å, and 0.005 eV/Å, respectively. The binding energy (E_b) were calculated by:

$$E_b = E_{total} - E_{slab} - E_M \quad (4.7)$$

where E_{total} indicates the total energy of the system; E_{slab} and E_M are the energies of individual SO_3^- and M ions, respectively.

4.3. Results and discussion

4.3.1. Preparation of the spatially ordered SMMT nanosheets

The fabrication procedure of the well-aligned SMMT membrane was shown in Figure 4.1a. The MMT nanosheets were first produced through ultrasound-assisted exfoliation. The atomic force microscopy (AFM) image of MMT nanosheets revealed typical monolayer morphology with the average lateral size of 220 nm and thickness of 1.5 nm (Figure 4.1b and c). The as-prepared nanosheets colloidal solution presented homogeneous dispersion (Figure 4.1d). Further, the sulfonated SMMT nanosheets were

obtained by physical blending MMT with the aqueous solution of sulfonated poly(vinyl alcohol) (SPVA), which is an ideal hydrogen-bonding agent and proton carrier due to its numerous oxygen-containing polar groups (Figure 4.1e) [32]. The absorption peaks at 3419, 2923 and 2856 cm^{-1} were attributed to the asymmetric and symmetric stretching vibration peaks of $-CH_2$ and -OH in SPVA, and the characteristic peaks of S=O stretching vibration appeared at 1123 and 1039 cm^{-1}, and the infrared results indicated the successful synthesis of SPVA (Figure 4.1f). The chemical composition of SPVA was further confirmed by ^1H NMR spectroscopy, where peaks between 7.7 and 8.2 ppm corresponded to the signals (d_1-d_3) of aromatic protons in BADSA (Figure 4.1g). Further, the sulfonation degree (Ds) of SPVA is 17.2% according to the Equation 4.6, indicating that the prepared SPVA has a high sulfonation degree.

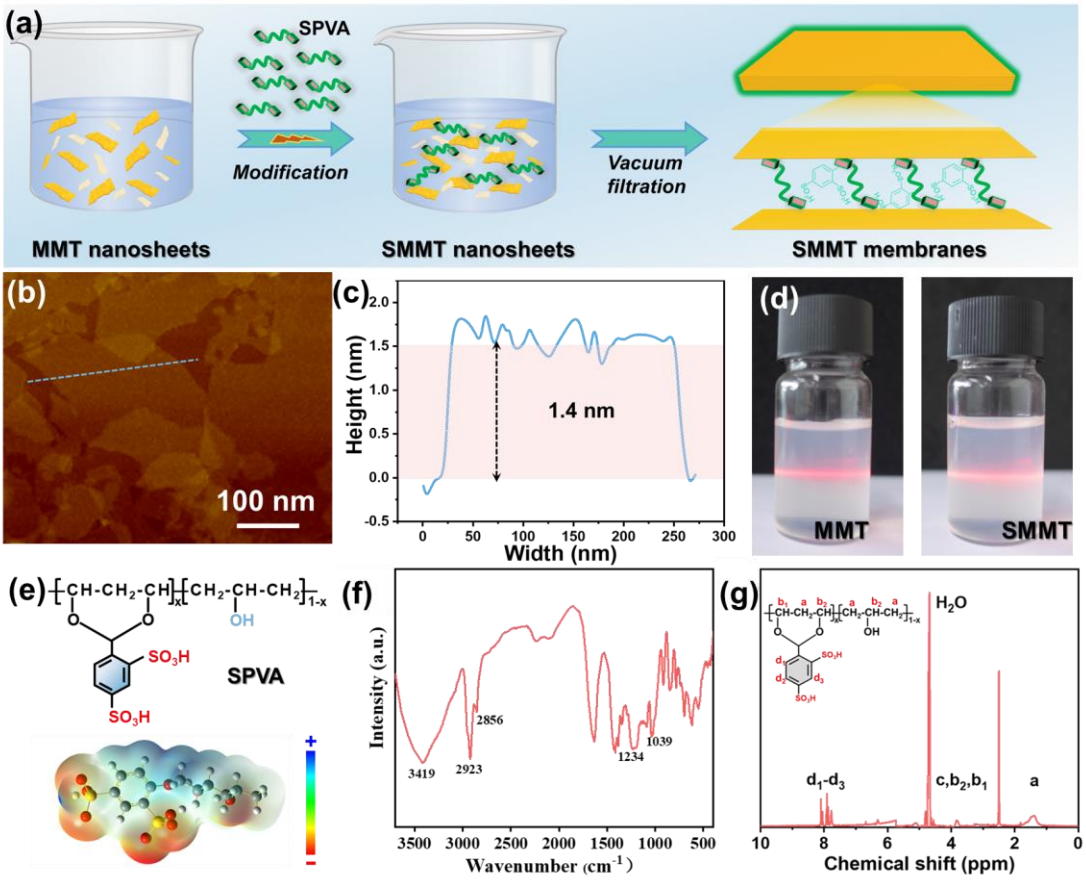


Figure 4.1 (a) Schematic illustration of the preparation process of the SMMT membrane. (b, c) The atomic force microscopy (AFM) image and corresponding monocrystal diameter of the typical MMT nanosheets. (d) Photographs of the MMT nanosheets before and after SPVA modification under a red laser beam. (e) Molecular structure and electrostatic potential of the SPVA molecule. (f) FTIR and (g) ^1H NMR spectra of SPVA.

As MMT nanosheets are mixed with the SPVA solution, SPVA molecules readily coat onto MMT surface via hydrogen bonds, causing sandwich-structural nanosheets [33]. This was revealed by UV-vis absorption spectra, where the peaks corresponding to MMT and SPVA were significantly shifted and integrated into a new peak after mixing, suggesting the hydrogen bond interaction between the hydroxyl groups of MMT and sulfonic acid groups (Figure 4.2a) [34]. Such interaction was further verified by the blue shift of X-ray photoelectron spectroscopy (XPS) spectra for O 1s core level (Figure 4.2b, c). After sulfonation modification, the zeta potential of nanosheets shifted from -36.7 mV to -49.4 mV, which also provided another proof for the coating of SPVA on the MMT surface (Figure 4.2d). The molecular structure of SPVA includes numerous polar functional groups (i.e., -OH and -SO_3H) with rich lone pair electrons, featuring negative electrostatic potential (ESP), which enhanced the negative charge of MMT nanosheets (Figure 4.1e).

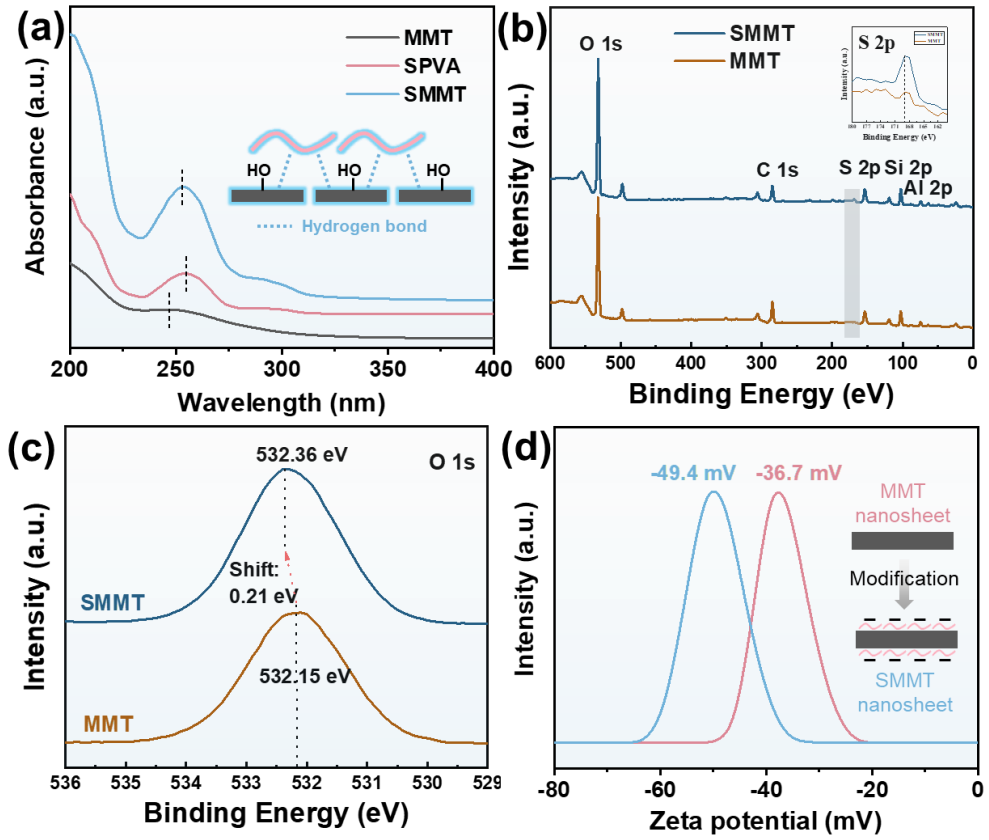


Figure 4.2 (a) UV-vis absorption spectra of the SPVA solution, MMT nanosheet, and SMMT nanosheet. XPS spectra of full spectra (b) and O 1s (c) for MMT nanosheets before and after SPVA modification. (d) Zeta potential of MMT nanosheets before and after SPVA modification.

Expectedly, the dramatic change variation in the surface potential of nanosheets are susceptible to affect their spatial arrangement. We investigated the spatial microstructure of MMT and SMMT nanosheets in colloidal solutions using liquid nitrogen transient freeze-drying technology. The scanning electron microscopy (SEM) images demonstrated the chaotic waviness and wrinkle in MMT nanosheets, suggesting that MMT had a randomly spatial orientation degree in the suspension, which readily induced the edge-to-edge interactions between nanosheets [13], resulting in edge overlapping and self-folding (Figure 4.3a). In contrast, SMMT exhibited a markedly flatter morphology with less wrinkles, which revealed the higher spatial orientation degree of SMMT nanosheets in the suspension after sulfonation (Figure 4.3b). Further, we also experimentally identified the spatial arrangement of nanosheet dispersions by polarized optical microscopy (POM). As shown in Figure 4.3c, the birefringence of the both nanosheets became more distinct as the concentration of the suspension increased, indicating the transition of the nanosheets from the isotropic to the nematic phase [20]. It is noteworthy that the birefringence of SMMT nanosheets was significantly stronger than that of MMT at the same concentration, proving that SPVA coating of MMT improved the arrangement of nanosheets in the suspension. It might ascribe to that the higher negative charge of nanosheets originated from negatively charged SPVA generated an electrostatic confinement effect, which constrained the random dispersion and engagement of nanosheets driven by the edge-to-edge interaction between nanosheets [35]. As the result, SMMT nanosheets presented the more stable and ordered dispersion in the suspension, favoring the aligned stacking and assembly of nanosheets into 2D lamellar membranes (Figure 4.3d).

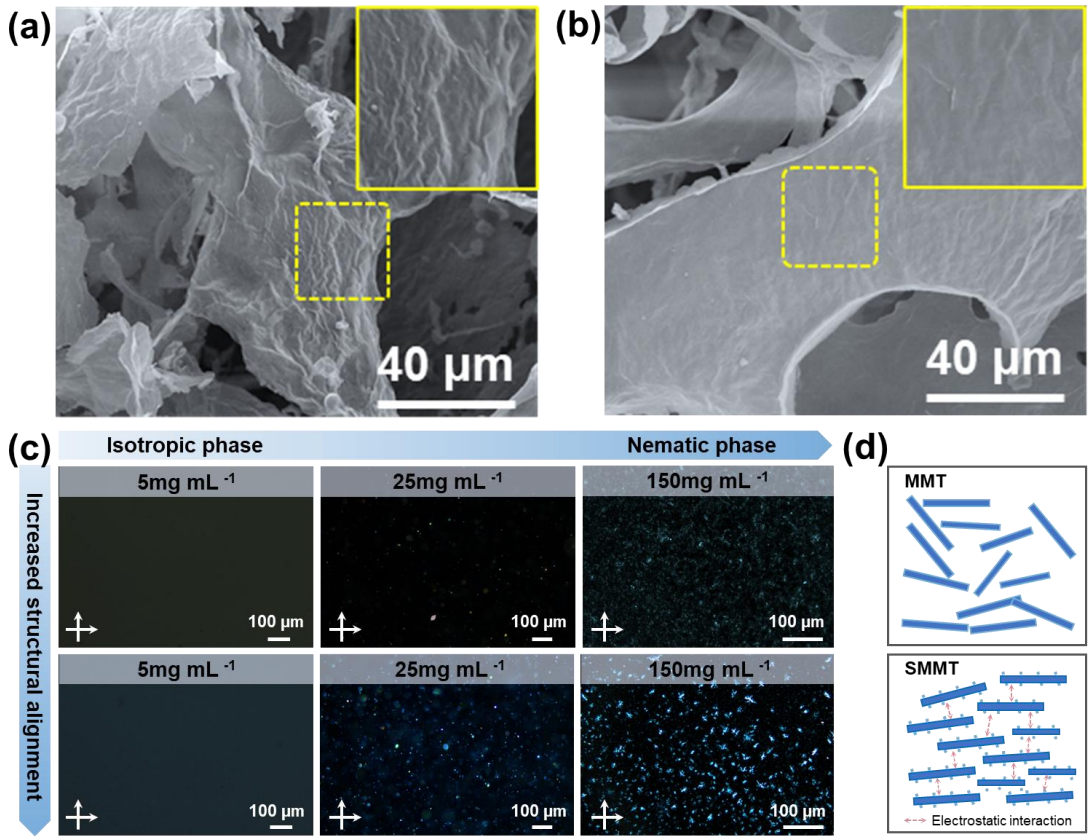


Figure 4.3 SEM images of (a) MMT nanosheets and (b) SMMT nanosheets after liquid nitrogen transient freeze-drying treatment. (c) POM images of MMT and SMMT nanosheets in dispersions with different concentrations. (d) Schematic illustration of the effect of SPVA modification on the spatial distribution of nanosheets in dispersions.

4.3.2. Fabrication of the in-plane aligned SMMT membrane

MMT and SMMT nanosheets were readily self-assembled into lamellar membranes with nanofluidic channels by vacuum filtration (Figure 4.1a), which were self-supporting and flexible. The three-dimensional AFM images presented visually the topographical differences between MMT and SMMT membranes, where the latter had arithmetic mean roughness (Ra) as low as 10.7 nm, far lower than that of the former membrane with a Ra of 45.7 nm (Figure 4.4a-b). This was verified by the increased water contact angle of the SMMT membrane surface (Figure 4.4c).

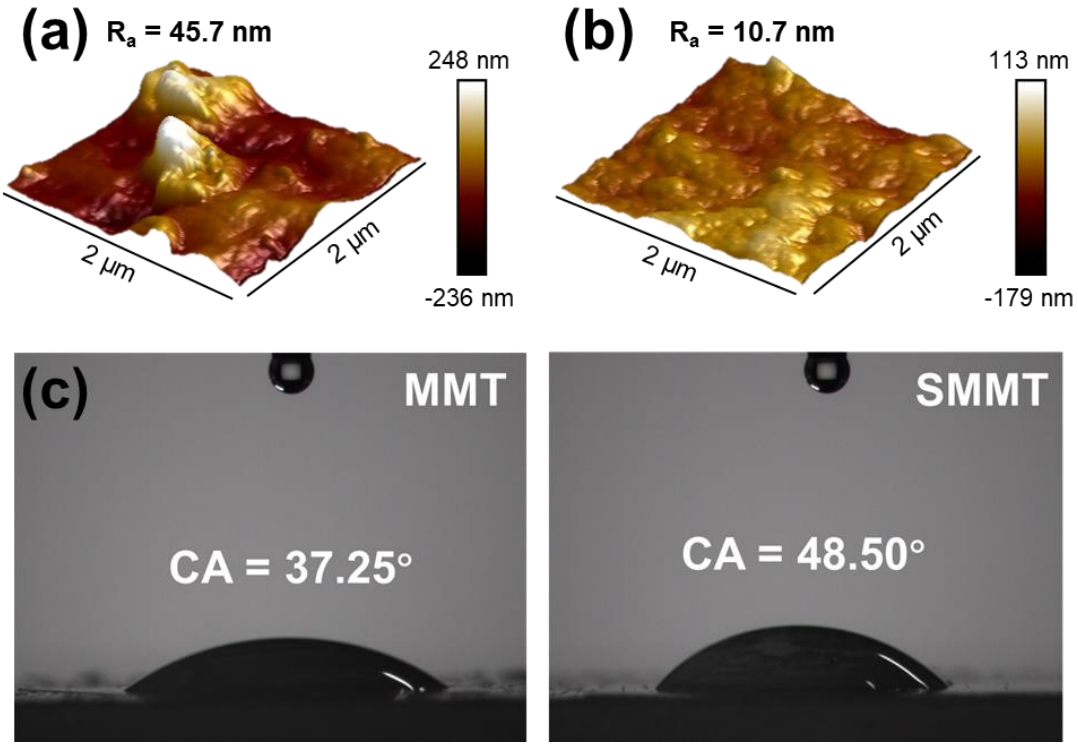


Figure 4.4 Three-dimensional AFM images of (a) MMT and (b) SMMT membranes. (c) Water contact angle images of MMT membrane and SMMT membrane.

As well, the SEM images displayed that SMMT membrane featured a smoother surface with less wrinkles compared to the MMT membrane (Figure 4.5a-d). The cross-sectional images revealed the higher alignment of SMMT membrane with ordered nanochannels originated from the layer-by-layer stacking of SMMT nanosheets, and SPVA was uniformly distributed in the membrane, while the twisted wrinkles in MMT membrane suggested the disordered stacking of nanosheets (Figure 4.5e-f).

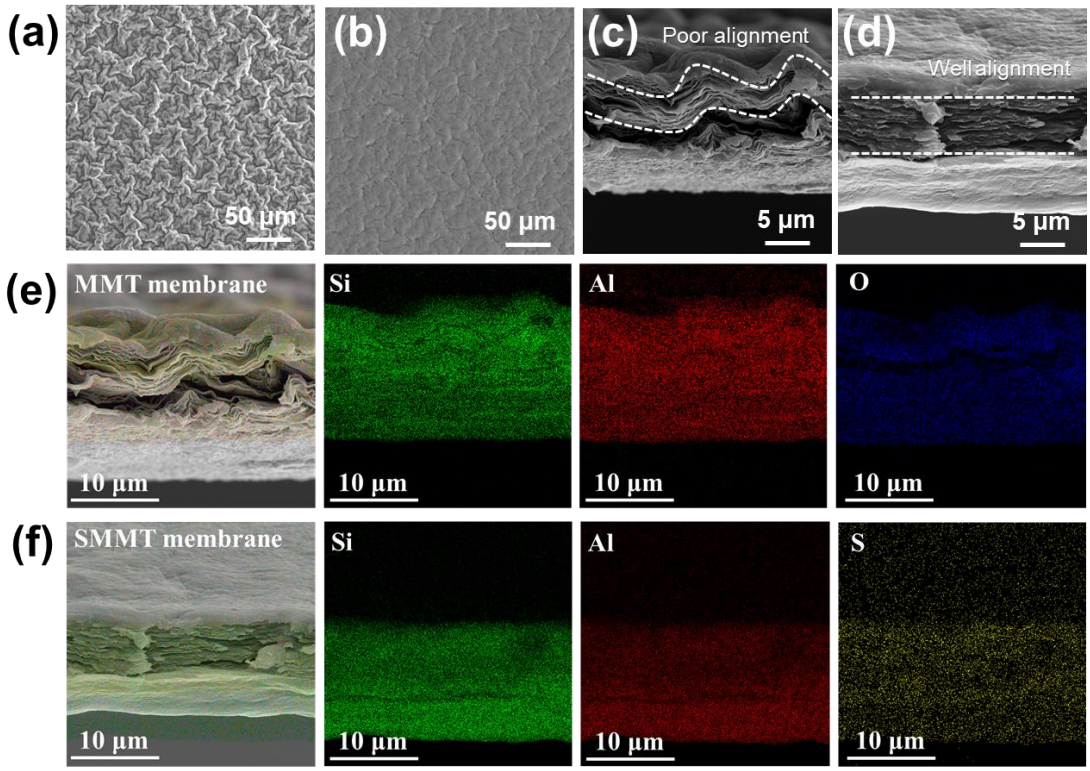


Figure 4.5 Surface SEM images of (a) MMT and (b) SMMT membranes. Cross-sectional SEM images of (c) MMT and (d) SMMT membranes. The EDS mapping of the cross section of the (e) MMT and (f) SMMT membrane.

Moreover, the microstructure of nanochannels was analyzed by X-ray diffraction (XRD) patterns of membranes (Figure 4.6a). It can be found that compared to the MMT membrane, SMMT membrane showed the narrower and stronger peak corresponding to (001) plane, demonstrating the more ordered nanochannels. In addition, the nanochannel size of the SMMT membrane was expanded from 0.29 nm to 0.34 nm (d-spacing of SMMT membrane ≈ 13.0 Å, platelet thickness of MMT ≈ 9.60 Å, namely, the interlayer free spacing ≈ 3.40 Å), which was caused by the SPVA coated on the MMT nanosheets being intercalated into the nanochannels as the assembly process proceeded [36]. Such expanded nanochannels were proved by the transmission electron microscopy (TEM) images of membranes, in which the lattice spacing of the SMMT membrane assigned to the (001) plane increased from 1.252 to 1.295 nm (Figure 4.6b, c). Further, combining with the XPS spectra for S 2p and O 1s core level, the hydrogen bond interaction between intercalated SPVA and MMT nanosheets was demonstrated (Figure 4.6d-f).

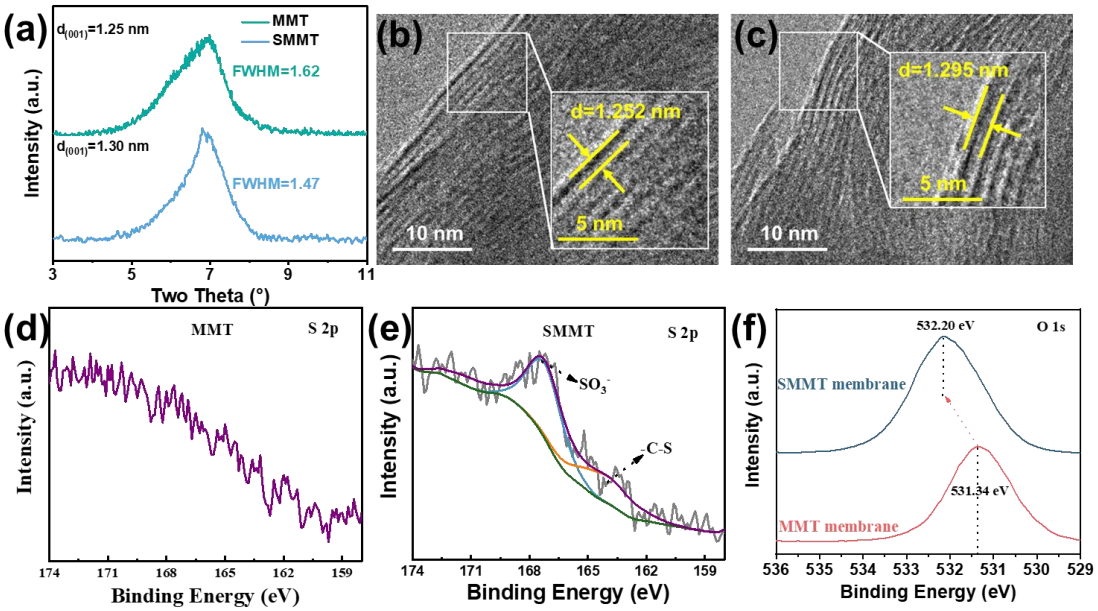


Figure 4.6 (a) XRD patterns of MMT and SMMT membranes. TEM images of (b) MMT and (c) SMMT membranes. S 2p core level XPS spectra for (d) MMT and (e) SMMT membranes. (f) O 1s XPS spectra for MMT and SMMT membranes.

Further, we applied POM and wide-angle X-ray diffraction (WAXS) to determine the stacking ordination of nanosheets in the membranes. As shown in Figure 4.7a, the MMT membrane exhibited distributed hue with dispersion degree of 31.87°, indicating the poor-aligned nanosheets. By contrast, the SMMT nanosheets showed the well in-plane stacking behavior in membranes according to the uniform hue over hundreds of micrometers and low dispersion degree (15.59°) of the POM image. The orientation degree of nanosheets in membranes was quantitatively analyzed via WAXS patterns. From 2D patterns, the SMMT membrane presented the more concentrated and intensive scattering compared to that of the MMT membrane, indicating the higher in-plane alignment of nanosheets (Figure 4.7b, c).

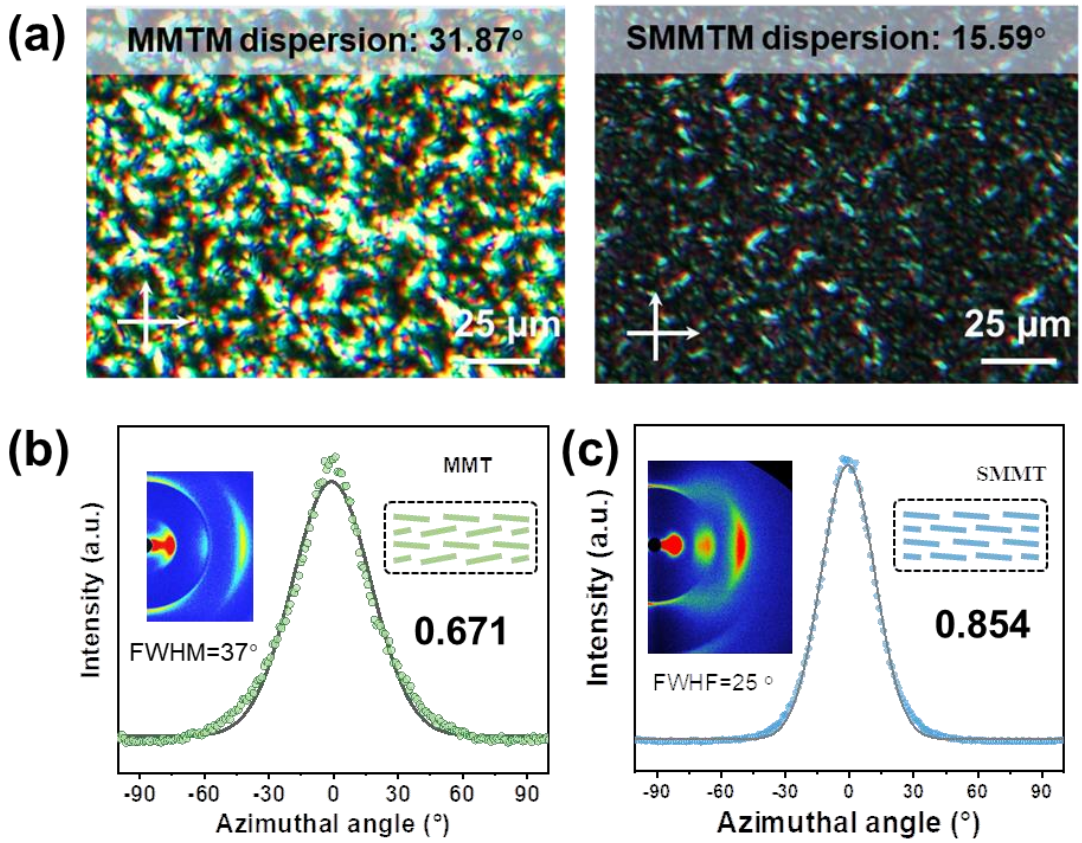


Figure 4.7 (a) POM images of MMT membrane and SMMT membrane. Analysis of nanosheet dispersion on different membrane surfaces by Fiji ImageJ software. WAXS patterns of (b) MMT and (c) SMMT membranes.

Furthermore, the WAXS data was converted into 1D azimuthal plots. The SMMT membrane (33°) had a narrower full width at half maximum (FWHM) than MMT membrane (37°), revealing that SPVA modification of MMT can effectively improve the nanosheet alignment. Also, we quantified the planar orientation degree of nanosheets in membranes through the Herman's orientation factor. The orientation factor was increased from 0.671 to 0.854 after modification (Figure 4.7 b, c). Such enhanced in-plane orientation of SMMT nanosheets illustrated the highly aligned and continuous nanochannels of the SMMT membrane.

The significantly improved alignment of the membrane and nanochannel structure due to our dual-constrained assembly strategy could be attributed to two reasons: i) Higher spatial orientation degree of SPVA-modified nanosheets allows for more aligned pre-assembly (Figure 4.3); ii) During the water removal of the pre-assembled network to induce stacking of nanosheets, the capillary force drives the lateral contraction of nanosheets, leading to the change of the formed nanochannels from flat

to wavy [15]. Whereas, the hydrogen bond interaction between interlayer SPVA and MMT nanosheets, exerts tensile forces to compensate for the capillary forces, thus restraining the disordering of the nanochannels (Figure 4.8) [17]. The high alignment of SMMT membrane is capable of facilitating proton transport.

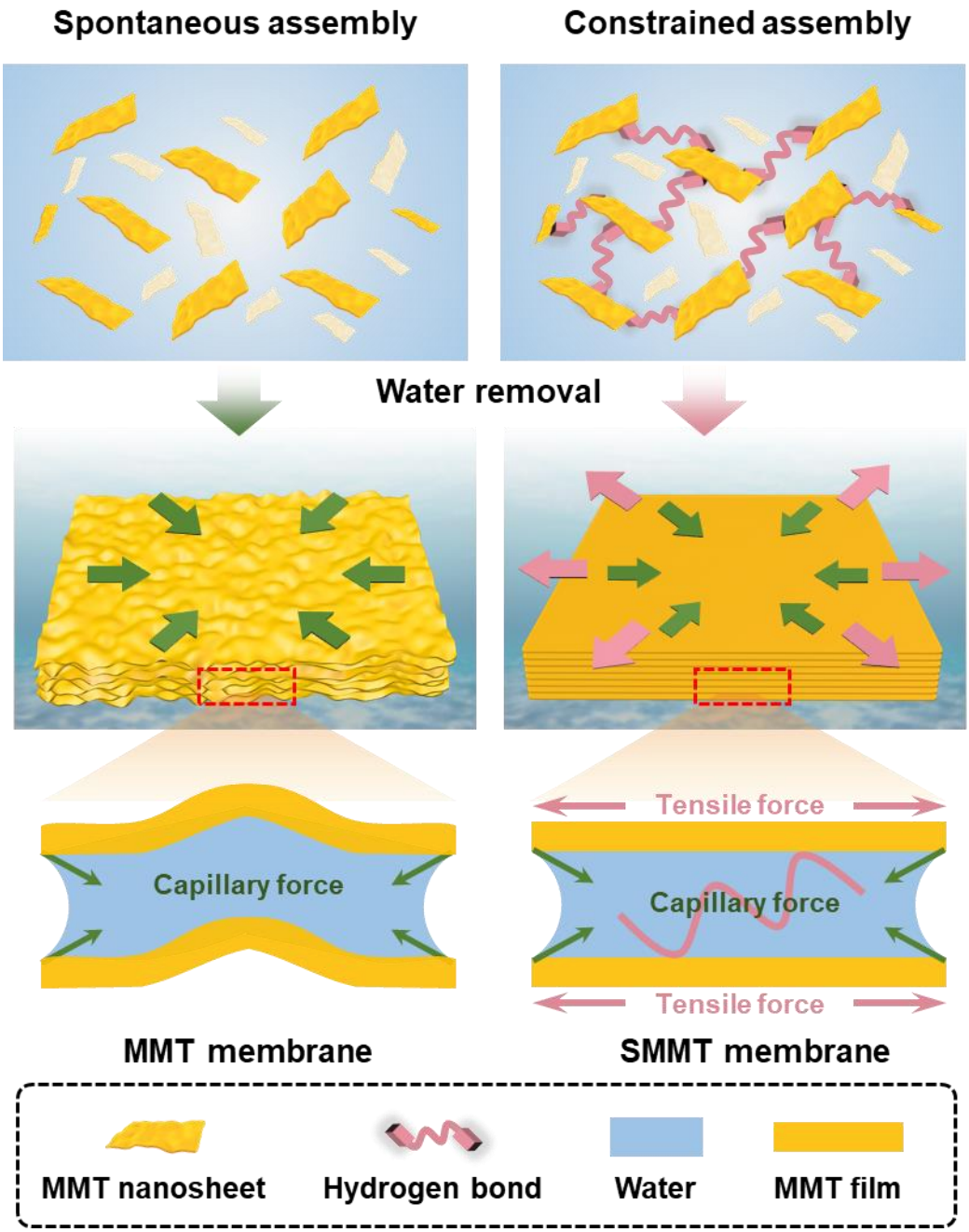


Figure 4.8 Schematic illustration of the hydrogen bonding interaction between interlayer SPVA and MMT nanosheets to generate tensile forces for compensating the capillary forces during water removal.

4.3.3. Proton conductivity of the SMMT membrane

To measure the proton conductivity of as-obtained membranes, we homemade a nanofluidic device, in which the MMT membranes were embedded in PDMS elastomer with their ends exposed to the HCl solution (Figure 4.9a). To avoid inadequate hydration of the MMT nanochannels (Figure 4.9b), and ensure the stable proton conductance tests, the membranes were wetted in HCl for 24 h prior to procedures. The representative current-voltage (I-V) curves of the SMMT membranes were determined in 0.1 M HCl solution (Figure 4.9c). The conductance (G) was then calculated from the slope of the I-V curve, and the proton conductivity (σ) was determined based on the dimensions of the 2D nanochannel. Figure 4.9d presented the temperature-dependent proton conductivity through the membranes. Both MMT and SMMT membranes showed a pronounced increase in conductivity with the elevating temperature from 30 °C to 80 °C due to the thermally activated behavior of the proton transport. The proton conductivity of SMMT was significantly higher than that of MMT. In particular, the conductivity of SMMT at 30 °C was high as 134.58 mS cm^{-1}, which showed an increase of 91.19% compared to MMT (70.39 mS cm^{-1}).

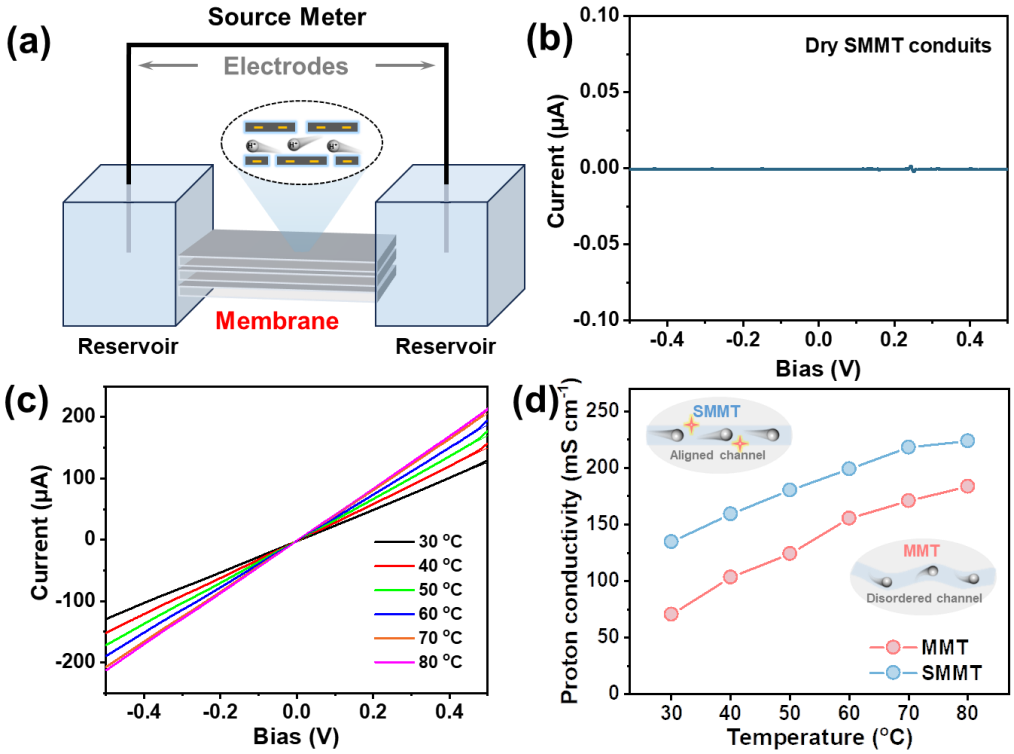


Figure 4.9 (a) Schematic illustration of the nanofluidic device. (b) I-V curves obtained on dry SMMT membranes. (c) The representative I-V curves of the SMMT membranes determined at different temperatures in 0.1 M HCl solution. (d) Temperature-dependent

proton conductivities of the MMT and SMMT membranes.

We further explored the mechanism of proton transport in membranes based on the Arrhenius analysis (Figure 4.10a). The activation energy (Ea) was estimated to be 16.78 and 9.19 kJ mol^{-1} for MMT and SMMT membranes, respectively, which were below 40 kJ mol^{-1}, suggesting the proton transport in membranes followed by the Grotthuss transport mechanism [37]. As well, we carried out the kinetic isotope effect (KIE) of SMMT membranes by soaking devices in deuterated electrolyte solution for exchanging H^+ with D^+. For the Grotthuss mechanism, the KIE value is required to exceed $(m_D/m_H)1/2 \sim 1.4$ since the mass of D atom (m_D) is twice that of H atom (m_H) [6]. In contrast, the KIE value for Vehicle mechanism is equal to the mass ratio of D_2O to H_2O, i.e., ~1.2. As exhibited in Figure 4.10b, the conductivity of the SMMT membrane in the H_2O system was 2.36 times higher than that in D_2O system, providing a solid proof for the proton transport governed by the Grotthuss mechanism. It is noted that the Ea of proton transport greatly reduced from 16.78 to 9.19 kJ mol^{-1} after SPVA modification, which also confirmed the enhanced proton transport in the SMMT membrane.

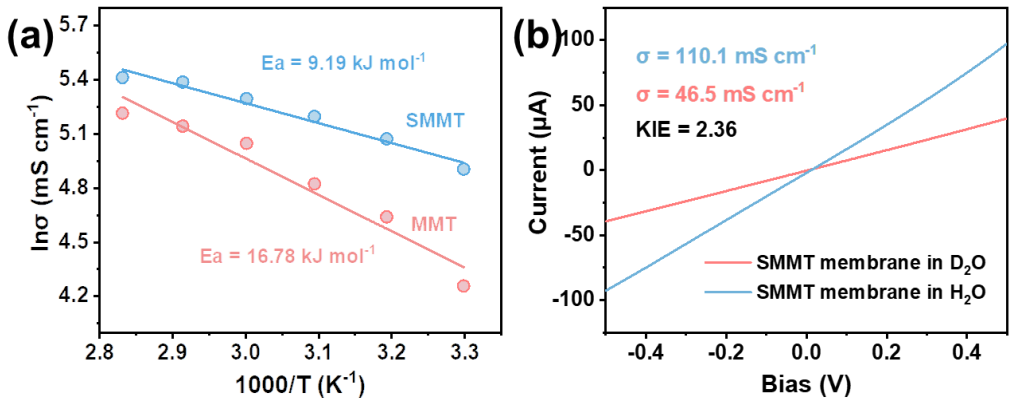


Figure 4.10 (a) Arrhenius plots of the MMT and SMMT membranes. (b) The I/V curves of the MMT and SMMT membranes recorded in HCl-D_2O and HCl-H_2O solution of 0.1 M at room temperature.

The improvement in proton transport might stem from two aspects: i) The nanosheets modified with SPVA feature the well spatial ordination and preferential planar alignment in membranes, enabling more ordered nanochannels for proton transport. Based on Nernst-Einstein relationship ($\sigma = Fa\mu$, where F is Faraday's constant, a refers ion concentration and μ represents the effective mobility of ions), the enhanced

alignment of nanochannels and thereby improved effect mobility of protons is able to facilitate proton conductivity [38]. ii) SPVA with -SO_3H groups can provide additional proton carriers to create rich hydrogen bond networks for accelerating proton transport. To this end, we determined the ion exchange capacity (IEC) of membranes before and after modification with SPVA (Figure 4.11). It can be found that the SMMT showed an increased IEC value compared to MMT, demonstrating the successful introduction of -SO3H groups. Notably, there was an increase in IEC of only 18.5% due to the low SPVA addition, making it hard for such a limited proton carriers to deliver a large increase in proton conductivity.

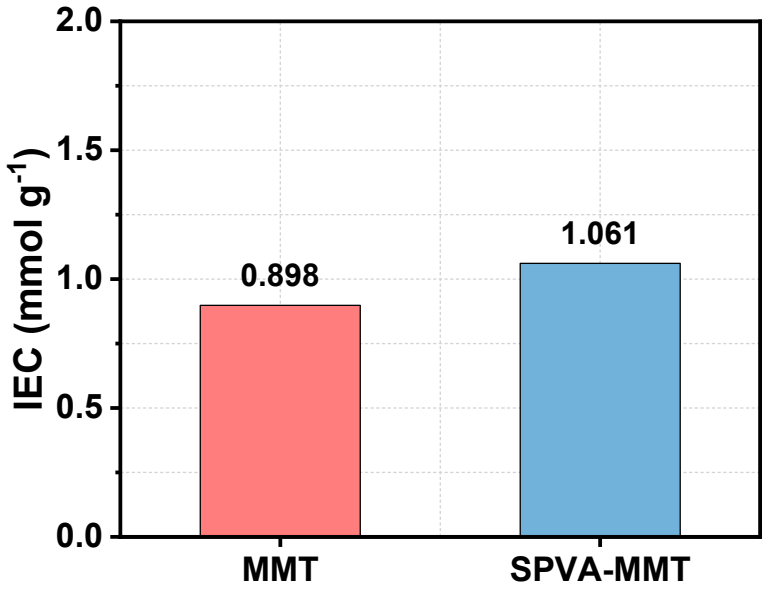


Figure 4.11 The IEC value of MMT and SMMT membranes.

As exhibited in the thermogravimetric analysis (TGA), compared to the pristine MMT membrane, an additional slight weight loss (6.06%) occurred at around 270 °C, corresponding to the decomposition of the SPVA, which affirmed the successful introduction of -SO_3H groups but in small amounts (Figure 4.12a, b). Therefore, it can be ruled that the enhanced proton conductivity of the SMMT membrane mainly depended on the increased orientation degree of nanochannels due to the electrostatic confinement effect (Figure 4.3d) and capillary force compensation effect (Figure 4.8) of SPVA, while additional proton carriers played a subsidiary role.

Further, we carried out conductivities of Na^+ and K^+ in MMT and SMMT membranes to determine the contribution of channel alignment (C_{align}) and contribution of proton carriers (C_c) of SPVA on proton conductivity (Figure 4.12c). Specifically, the transport of Na^+ and K^+ in membranes obeys the Vehicle mechanism, which desires

highly aligned channel structure [39]. The SPVA has a negative C_c on Na^+ and K^+ transport in membranes due to the stronger binding interaction between -SO_3H groups and cations (Figure 4.12d).

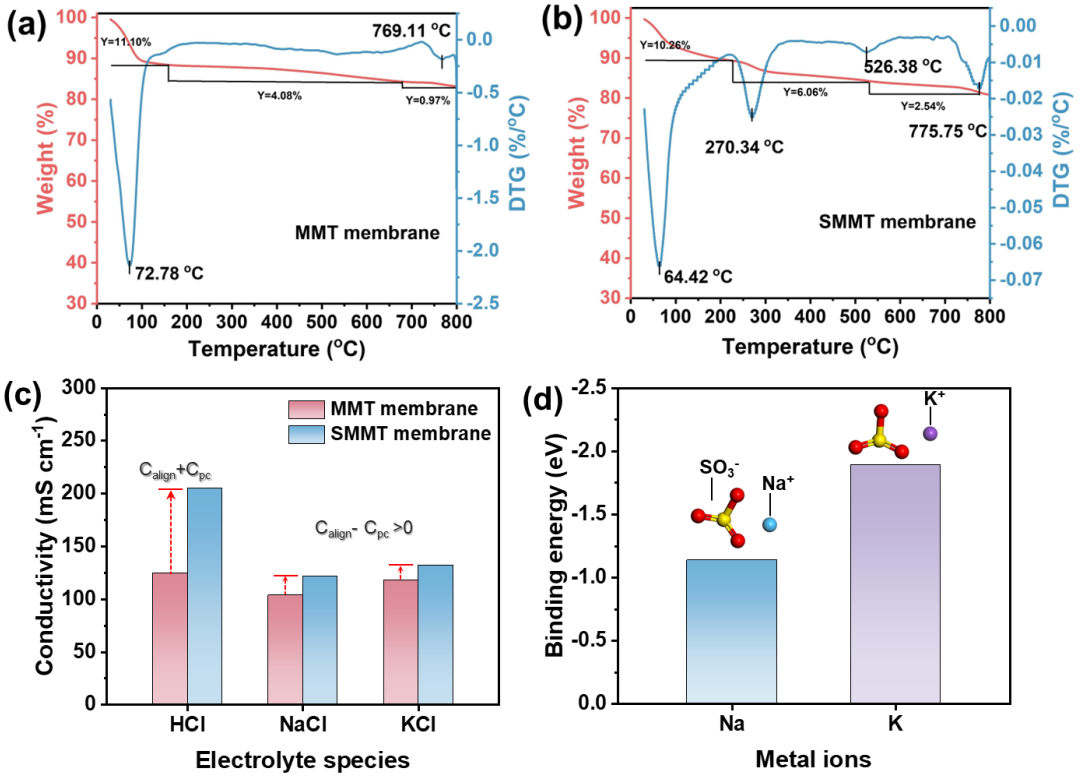


Figure 4.12 TGA curves of (a) MMT and (b) SMMT membranes. (c) The conductivities of MMT and SMMT membranes in different electrolytes of 1 M. (d) The binding energies between Na^+/K^+ and SO_3^-.

Unexpectedly, the Na^+ and K^+ conductivities of the SMMT membrane was higher than these of the MMT membrane, revealing the dominant effect of Calign in ion transport. Whereas the protons, in addition to Vehicle mechanism for diffusion and migration, are mainly hopping transport via Grotthuss mechanism [40]. As the strong acid, the -SO_3H groups can bind to protons released from hydrated hydrogen ions or free protons, and then dissociate to facilitate proton hopping transport. Thus, SPVA imparts a positive C_c to the SMMT membrane. Accordingly, the increased orientation degree of nanochannels and additional proton carriers jointly contributed to rapid proton conduction, where the former hold the primary role. Benefiting from these properties, the SMMT membrane exhibited low Ea and high conductivity, outperforming most of the state-of-the-art PEMs reported in the literature under the similar conditions (Figure 4.13).

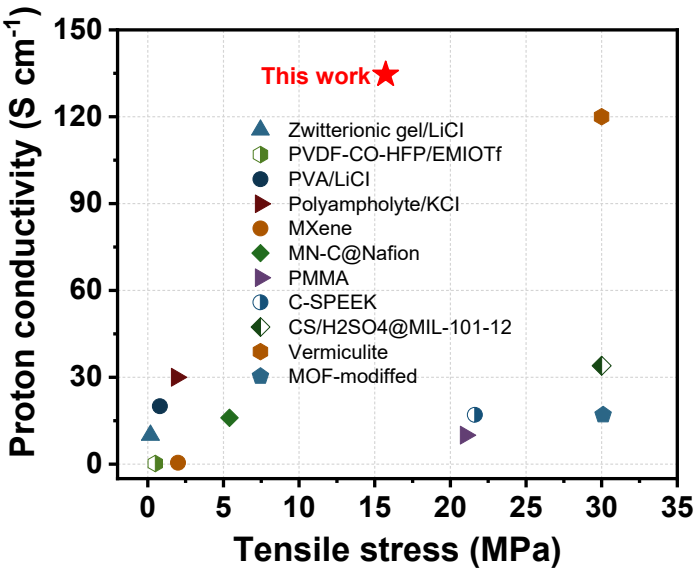


Figure 4.13 Proton conductivity and activation energy of the SMMT membrane compared with those of state-of-the-art PEMs reported in the literature.

As displayed in Figure 4.14a, with the raising concentration, the conductivity of both membranes significantly increased, which indicated that MMT-based membranes are capable of offering outstanding proton conductivity through 2D nanochannels once enough protons are available. Expectedly, SMMT with highly ordered nanochannels presented enhanced conductivity under the tested conditions. Furthermore, we compared the proton conductivity in the low (0.1 mM) and high (0.1 M) proton concentration with that of the reported PEMs in the literature (Figure 4.14b). The results exhibited the universal high-performance of the SMMT membrane, revealing the advancement of our dual-constrained assembly strategy in achieving the fast proton transport.

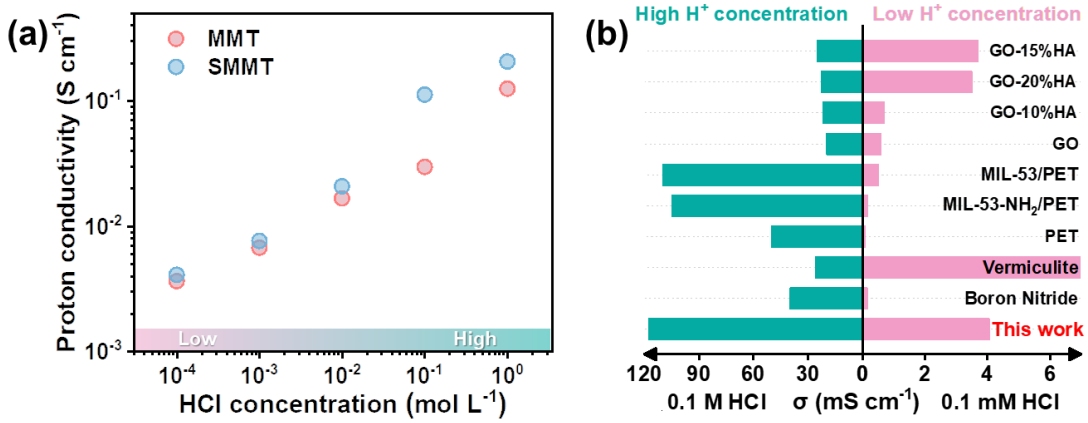


Figure 4.14 (a) Concentration-dependent proton conductivities of the MMT and SMMT membranes at room temperature. (b) Proton conductivities of the SMMT

membrane in the low (0.1 mM) and high (0.1 M) proton concentration compared with those of state-of-the-art PEMs reported in the literature

4.3.4. Conductivity Stability of the SMMT membrane

Stability is a common challenge for PEMs in practical applications in complex environments. Therefore, the stability of proton conductivity of the SMMT membrane was investigated comprehensively. It is stated that the SMMT membrane remained stable after 30 days of immersion in 0.1 M HCl solution, demonstrating the hydro-stability. The dimensional stability of SMMT membrane was also confirmed by the negligible in-plane (<3.2%) and through-plane (<5.0%) dimensional swelling under various temperatures at saturated relative humidity of 98% (Figure 4.15a, b). Furthermore, the conductivity of the SMMT membrane could maintain constant during a continuous long-term operation for nearly 1000 min under both room and high temperatures with negligible structural changes, indicating the admirable stability (Figure 4.15c). Such thermal stability was further confirmed by low and slow weight loss on heating to 250 °C that is the typically highest working temperature for PEMs (Figure 4.12a, b). Also, the SMMT membrane presented high tolerance during successive cooling-heating cycles from 30 to 80 °C. The conductivity did not exhibited decline at each cooling-heating cycle, which could assign to the intrinsic structural stability of nanochannels assembled by 2D nanoclays (Figure 4.15d).

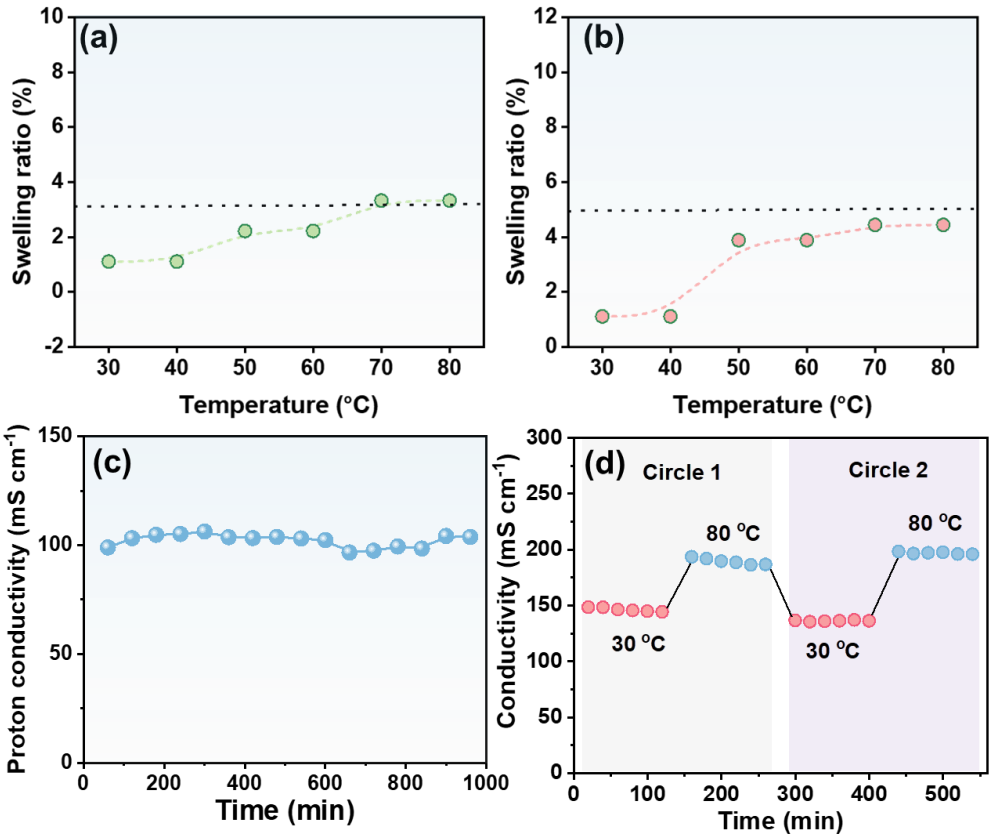


Figure 4.15 (a) The in-plane and (b) through-plane dimensional swelling of SMMT under different temperatures and 98% RH. (c) Proton conductivity stability of the SMMT membrane during the long-term test at room temperature. (d) Proton conductivity stability of the SMMT membrane under two heating-cooling cycles from 30 to 80 °C.

The XRD characteristic peaks and FWHM of the SMMT membrane remained essentially unchanged after long-term operation, illustrating the structural stability of the SMMT membranes (Figure 4.16a). Mechanical performance, another critical property for PEMs, was evaluated by stress-strain curves (Figure 4.16b). Due to the poor-aligned stacking and arrangement of nanosheets in the MMT membrane, reducing the inter-nanosheet stress transfer efficiency and causing about local stress concentration, the MMT membrane had the limited mechanical strength (3.61 MPa) [41]. In the case of the SMMT membrane, however, the Young's modulus (813 MPa) and tensile strength (15.72 MPa) were significantly improved owing to the more ordered stacking of the SMMT nanosheets and the inter-nanosheet bonding of hydrogen bonds. Compared with the PEMs reported in the literature, the SMMT membrane showed outstanding proton conduction and mechanical stability (Figure 4.16c). Further, the flexibility of the SMMT membrane was assessed. The membrane could maintain

the structural integrity after hundreds of bending cycles. We determined the proton conductivity of the curved SMMT membrane by bending the nanofluidic device to varying degrees (Figure 4.16d). It can be found that the I-V curves recorded in the curved and straightened states almost overlapped, that is, the conductivity maintained constant, which confirmed the robust nanochannels of SMMT membrane for proton transport.

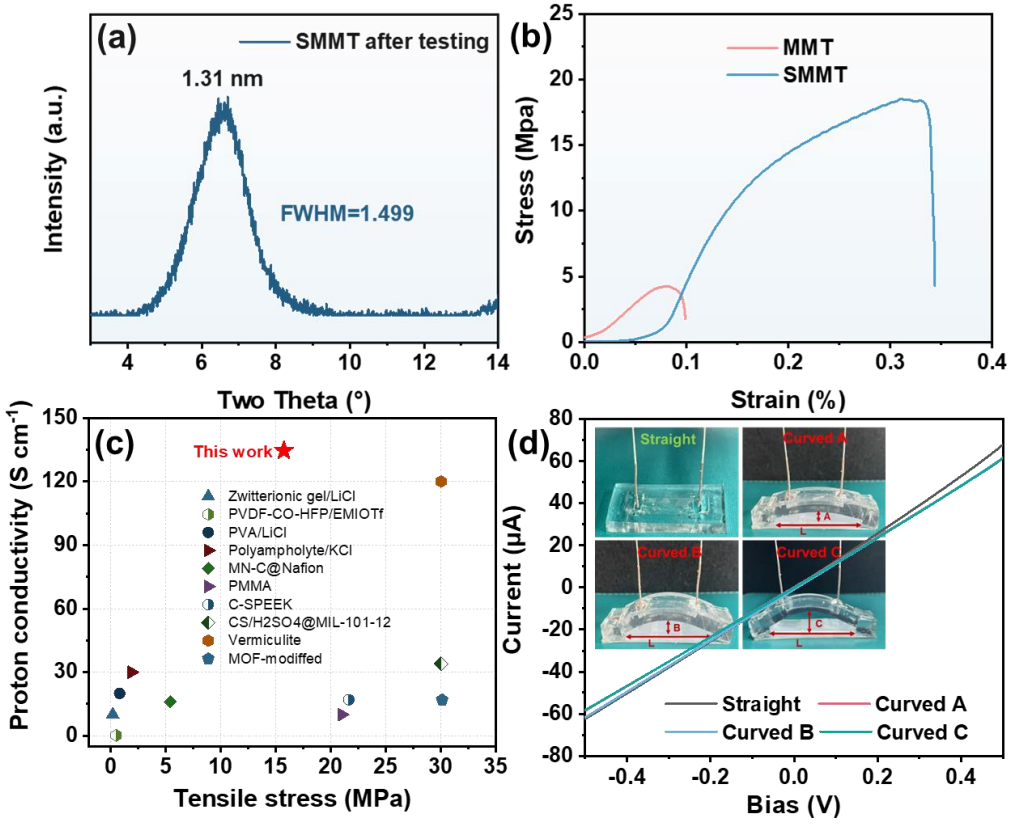


Figure 4.16 (a) The XRD pattern of the SMMT membranes after long-term operation at the room temperature. (b) The stress-strain curves of the MMT and SMMT membranes. (c) Proton conductivity and mechanical strength of the SMMT membrane compared with those of state-of-the-art PEMs reported in the literature. (d) Representative I-V curves of the SMMT membrane recorded at 0.1 M HCl concentration at the straight and different curved states.

To investigate the reversibility of the scaled-up membranes, we prepared two SMMT membranes with a diameter of 10 cm. Then the membrane was divided into nine regions for measuring the thickness (Figure 4.17a). It was displayed that all regions in the both membranes had almost the same thickness (~18 μm), illustrating that the scale-up of the SMMT membranes had well consistency and reversibility (Figure 4.17b). In addition, we randomly selected four sites for performing proton transport (Figure 4.17c).

As displayed in Figure 4.17d, conductivities of the four sites kept a great agreement, proving the excellent homogeneity of the SMMT membranes. It was noted that the size and thickness of the membrane could be flexibly tailored by controlling the preparation process and the amount of nanosheets, presenting the promise of simple large-scale manufacture in future.

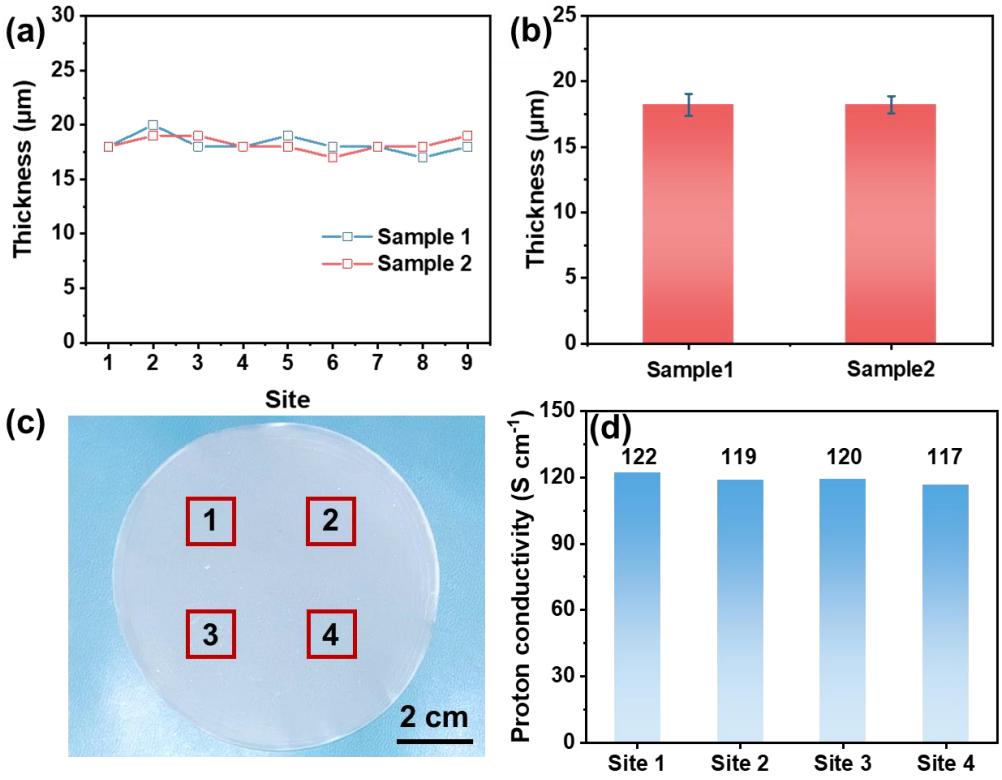


Figure 4.17 (a) The thickness of different sites from SMMT membranes. (b) Average thickness of different SMMT membranes. The error bars in the figure represent the standard deviations for nine measurements. (c) The photograph of the scaled-up free-standing SMMT membrane marked with four randomly selected test sites. (d) Proton conductivities at different sites of the scaled-up SMMT membrane.

4.4. Conclusions

In summary, to address the vulnerability of nanochannels to disorder during the construction of 2D lamellar PEMs, we developed a dual-constrained assembly strategy to induce the ordered stacking and assembly of nanosheets into aligned nanofluidic channels. Characterizations and experiments reveal that through facile modification with SPVA, MMT nanosheets were endowed with more negative charges and additional proton carriers, which created an electrostatic confinement effect to constrain the edge-to-edge interaction between nanosheets for the more stable and ordered dispersion.

Further, the hydrogen bond interaction between SPVA and nanosheets offered in-plane tensile forces to constrain nanochannels disordering driven by capillary forces. Benefiting from these emerging properties, SPVA-modified MMT membrane exhibited greatly increased alignment, thereby dramatically increasing the proton conductivity by 91.19% and lowering the energy barrier of proton transport by 82.5%, compared to the pristine MMT membranes. In addition, SMMT membrane featured excellent stability and scalability as well. Compared with other assembly strategies, our dual-constrained assembly strategy presented the advantages of universality, accessibility and sustainability in constructing high-performance PEMs with highly ordered nanochannels, which can be extended for the development of different lamellar membrane fields.

4.5. References

[1] Shi B, Pang X, Lyu B, et al. Spacer-Engineered Ionic Channels in Covalent Organic Framework Membranes Toward Ultrafast Proton Transport. Advanced Materials, 2023, 35(16): 2211004.

[2] Schnell J R, Chou J J. Structure and mechanism of the M2 proton channel of influenza A virus. Nature, 2008, 451(7178): 591-595.

[3] Jiao K, Xuan J, Du Q, et al. Designing the next generation of proton-exchange membrane fuel cells. Nature, 2021, 595(7867): 361-369.

[4] Wang C, Shen Y, Wang X, et al. Imparting stable and ultrahigh proton conductivity to a layered rare earth hydroxide via ion exchange. ACS Applied Materials & Interfaces, 2024, 16(17): 22648-22656.

[5] Cao X J, Cao L H, Bai X T, et al. An Ultra-Robust and 3D Proton Transport Pathways iHOF with Single-Crystal Superprotonic Conductivity Around 0.4 S cm^{-1}. Advanced Functional Materials, 2024, 34(49): 2409359.

[6] Qian X, Chen L, Yin L, et al. CdPS3 nanosheets-based membrane with high proton conductivity enabled by Cd vacancies. Science, 2020, 370(6516): 596-600.

[7] Chen C, Chen J, Peng Y, et al. Multifunctional coatings of graphene oxide: New membranes for proton permeation and salt rejection. Matter, 2024, 7(3): 1259-1274.

[8] Nair R R, Wu H A, Jayaram P N, et al. Unimpeded permeation of water through helium-leak–tight graphene-based membranes. Science, 2012, 335(6067): 442-444.

[9] Shi B, Pang X, Li S, et al. Short hydrogen-bond network confined on COF surfaces enables ultrahigh proton conductivity. Nature Communications, 2022, 13(1): 6666.

[10] Wolke C T, Fournier J A, Dzugan L C, et al. Spectroscopic snapshots of the

proton-transfer mechanism in water. Science, 2016, 354(6316): 1131-1135.
[11] Zhang Z, Liang L, Feng J, et al. Significant enhancement of proton conductivity in solid acid at the monolayer limit. Nature Communications, 2024, 15(1): 2706.
[12] Lu X, Gabinet U R, Ritt C L, et al. Relating selectivity and separation performance of lamellar two-dimensional molybdenum disulfide (MoS2) membranes to nanosheet stacking behavior. Environmental science & technology, 2020, 54(15): 9640-9651.
[13] Shen X, Lin X, Yousefi N, et al. Wrinkling in graphene sheets and graphene oxide papers. Carbon, 2014, 66: 84-92.
[14] Zhang S C, Hou Y Z, Chen S M, et al. Highly regular layered structure via dual-spatially–confined alignment of nanosheets enables high-performance nanocomposites. Advanced Materials, 2024, 36(35): 2405682.
[15] Putz K W, Compton O C, Segar C, et al. Evolution of order during vacuum-assisted self-assembly of graphene oxide paper and associated polymer nanocomposites. Acs Nano, 2011, 5(8): 6601-6609.
[16] Yang J, Li M, Fang S, et al. Water-induced strong isotropic MXene-bridged graphene sheets for electrochemical energy storage. Science, 2024, 383(6684): 771-777.
[17] Li H, Zhao J, Huang L, et al. A constrained assembly strategy for high-strength natural nanoclay film. ACS nano, 2022, 16(4): 6224-6232.
[18] Cheng H, Zhao F, Xue J, et al. One single graphene oxide film for responsive actuation. ACS nano, 2016, 10(10): 9529-9535.
[19] Zhang J, Uzun S, Seyedin S, et al. Additive-free MXene liquid crystals and fibers. ACS central science, 2020, 6(2): 254.
[20] Huang L, Wu H, Ding L, et al. Shearing liquid-crystalline MXene into lamellar membranes with super-aligned nanochannels for Ion Sieving. Angewandte Chemie International Edition, 2024, 63(6): e202314638.
[21] Zhong J, Sun W, Wei Q, et al. Efficient and scalable synthesis of highly aligned and compact two-dimensional nanosheet films with record performances. Nature Communications, 2018, 9(1): 3484.
[22] Zhao C, Zhang P, Zhou J, et al. Layered nanocomposites by shear-flow-induced alignment of nanosheets. Nature, 2020, 580(7802): 210-215.
[23] Xin G, Zhu W, Deng Y, et al. Microfluidics-enabled orientation and microstructure control of macroscopic graphene fibres. Nature nanotechnology, 2019, 14(2): 168-175.
[24] Tu H, Xie K, Lin X, et al. Superior strength and highly thermoconductive cellulose/boron nitride film by stretch-induced alignment. Journal of Materials Chemistry A, 2021, 9(16): 10304-10315.
[25] Li P, Yang M, Liu Y, et al. Continuous crystalline graphene papers with gigapascal strength by intercalation modulated plasticization. Nature communications, 2020, 11(1): 2645.
[26] Wan S, Chen Y, Fang S, et al. High-strength scalable graphene sheets by freezing

stretch-induced alignment. Nature Materials, 2021, 20(5): 624-631.
[27] Wan S, Li X, Wang Y, et al. Strong sequentially bridged MXene sheets. Proceedings of the National Academy of Sciences, 2020, 117(44): 27154-27161.
[28] Jiang X, Zhang L, Miao Y, et al. Intrinsic roles of nanosheet characteristics in two-dimensional montmorillonite membranes for efficient Li+/Mg2+ separation. Water Research, 2025, 276: 123291.
[29] Miao Y, Zhao Y, Zhang L, et al. Dewatering behavior and regulation mechanism of montmorillonite nanosheet in aqueous solution. Journal of Colloid and Interface Science, 2023, 652: 1620-1630.
[30] He G, Xu M, Zhao J, et al. Bioinspired ultrastrong solid electrolytes with fast proton conduction along 2D channels. Advanced Materials, 2017, 29(28): 1605898.
[31] Zhu L, Ye P, Zhang L, et al. Bioinspired heterogeneous construction of lignocellulose-reinforced COF membranes for efficient proton conduction. Small, 2024, 20(3): 2304575.
[32] Cao L, Wu H, Yang P, et al. Graphene oxide-based solid electrolytes with 3D prepercolating pathways for efficient proton transport. Advanced Functional Materials, 2018, 28(50): 1804944.
[33] Li Y Q, Yu T, Yang T Y, et al. Bio-inspired nacre-like composite films based on graphene with superior mechanical, electrical, and biocompatible properties. Advanced Materials, 2012, 24(25): 3426-3431.
[34] Yang P, Wu H, Khan N A, et al. Intrinsic proton conductive deoxyribonucleic acid (DNA) intercalated graphene oxide membrane for high-efficiency proton conduction. Journal of Membrane Science, 2020, 606: 118136.
[35] Chen J, Shen Z, Kang Q, et al. Chemical adsorption on 2D dielectric nanosheets for matrix free nanocomposites with ultrahigh electrical energy storage. Science Bulletin, 2022, 67(6): 609-618.
[36] Zhang T, Ren B, Bai H, et al. Subnanometer-scale control of channel height in two-dimensional montmorillonite membrane for ion separation. Journal of Membrane Science, 2023, 675: 121573.
[37] Qin S, Liu D, Wang G, et al. High and stable ionic conductivity in 2D nanofluidic ion channels between boron nitride layers. Journal of the American Chemical Society, 2017, 139(18): 6314-6320.
[38] Li Z, Wang W, Chen Y, et al. Constructing efficient ion nanochannels in alkaline anion exchange membranes by the in situ assembly of a poly (ionic liquid) in metal–organic frameworks. Journal of Materials Chemistry A, 2016, 4(6): 2340-2348.
[39] He X, Yang Y, Wu H, et al. De novo design of covalent organic framework membranes toward ultrafast anion transport. Advanced Materials, 2020, 32(36): 2001284.
[40] Kreuer K D, Paddison S J, Spohr E, et al. Transport in proton conductors for fuel-cell applications: simulations, elementary reactions, and phenomenology.

Chemical reviews, 2004, 104(10): 4637-4678.

[41] Jiang Y, Wang Y, Xu Z, et al. Conformation engineering of two-dimensional macromolecules: a case study with graphene oxide. Accounts of Materials Research, 2020, 1(3): 175-187.

This chapter was published in J. Mater. Chem. A, 2025, 13, 25489-25497. (JCR Q1

Chapter 5.

Conclusions

The development of high-performance two-dimensional functional membranes has become a key area of research in the fields of membrane science and materials engineering. Two-dimensional MMT provides a promising material platform for the construction of high-performance ion-transport membranes. However, two-dimensional MMT channel membranes still face several key challenges in practical applications: i) insufficient orderliness in the stacking of nanolayers, leading to an inhomogeneous channel structure that impairs ion transport; ii) the difficulty in precisely controlling interlayer interactions and hydrogen-bond networks, which limits proton conduction efficiency; iii) insufficient coordinated control over channel size, interfacial charge and specific recognition capability, which hinders the simultaneous improvement of ion separation performance and structural stability. To address these issues, this thesis focuses on the structural regulation and interfacial functionalization of two-dimensional MMT channels, systematically exploring strategies such as the regulation of spatial order, the engineering of interfacial hydrogen-bond networks, and ion recognition. It provides a theoretical basis and technical support for the design and application of high-performance two-dimensional MMT functional membranes. The main conclusions are summarized as follows:

1. A biomimetic sub-nanochannels array strategy has been developed to form a two-dimensional MMT channel membrane capable of rapid and robust proton transport. The spatial microstructure, proton concentration, and electrostatic effect of sub-nanochannels were readily tuned by modulating the intrinsic LCD properties of nanosheets. Characterization and simulations demonstrated that controlling the LCD to construct well-ordered sub-nanochannels with considerable proton concentration was the key for efficient proton transport. Consequently, the optimal membranes without external proton carriers presented a superior proton conductivity of 79.11 mS cm^{-1} and long-term operational stability.

2. The dual-constrained assembly strategy was developed to induce the ordered stacking and assembly of nanosheets into aligned nanofluidic channels. Through facile modification with SPVA, MMT nanosheets were endowed with more negative charges and additional proton carriers, which created an electrostatic confinement effect to

constrain the edge-to-edge interaction between nanosheets for the more stable and ordered dispersion. Further, the hydrogen bond interaction between SPVA and nanosheets offered in-plane tensile forces to constrain nanochannels disordering driven by capillary forces. Benefiting from these emerging properties, SPVA-modified MMT membrane exhibited greatly increased alignment, thereby dramatically increasing the proton conductivity by 91.19% and lowering the energy barrier of proton transport by 82.5%, compared to the pristine MMT membranes. In addition, SMMT membrane featured excellent stability and scalability as well.

3. The acid-base pairs configuration strategy was developed to fabricate structurally robust 2D MMT nanofluidic channel membranes for stable and fast proton transport. The acid-base functional groups within modifiers regulate the microenvironment of channels, increasing the number of proton carriers and effectively enhancing the proton conductivity of the membrane. Benefiting from the stable hydrogen-bonding structures, the HMAHP membrane exhibits superior proton conductivity, reaching 149.53 mS cm^{-1} at 30 °C.

4. The novel two-dimensional nanochannel edge-functionalization strategy was developed to fabricate an ASMMT/PA NF membrane with uniform and precisely controlled pore structures, achieving high separation of Li^+ and Mg^{2+}. APTES was selectively grafted onto the edges of two-dimensional MMT nanochannels, introducing positively charged amino groups at the nanochannel edges. Meanwhile, the amino-functionalized MMT provided additional positively charged ion-recognition sites, which effectively suppressed the transport of Mg^{2+} through electrostatic interactions. The synergistic effect of precise size sieving and selective ion recognition enable the ASMMT/PA membrane with outstanding Li^+/Mg^{2+} separation performance.

Conclusive remarks

The research presented systematically addresses the key challenges in two-dimensional MMT functional membranes, progressing from nanochannel spatial ordering to interfacial hydrogen-bond network engineering and ion-recognition regulation: i) the intrinsic layer charge density was regulated to construct ordered sub-nanochannel arrays for efficient proton transport; ii) dual-constrained assembly and iii) acid-base pair functionalization were employed to improve nanosheet alignment, regulate interfacial hydrogen-bond networks, and enhance proton conduction and structural stability; iv) the edge-selective functionalization was introduced to integrate precise size sieving with selective ion recognition, enabling efficient Li^{+}/Mg^{2+} separation. Collectively, these studies establish a systematic strategy for regulating channel structure, interfacial chemistry, and ion transport in two-dimensional MMT membranes.

Although these findings represent a significant advancement in the understanding of ion transport and separation mechanisms within 2D MMT channels, future research should focus on the coupling mechanisms among structural ordering, interfacial chemistry, and selective ion transport. In particular, it is essential to elucidate the "structure-transport" relationship, optimize membrane performance under complex operating conditions, and enhance both long-term stability and scalability of production. These efforts will further facilitate the practical application of 2D MMT-based functional membranes in ion transport and resource recovery.

Appendix I. Articles published during the Ph. D studies

(*indicates corresponding author.)

[1] **Zhenlei Wang**, Lianqiu Huang, Lingjie Zhang, Tingting Zhang, Jianglin Yan, Licai Chen, Xiongrui Jiang, Damiano Sarocchi, Shaoxian Song, Viridiana García Meza, Mildred Quintana, Yunliang Zhao. A dual-constrained assembly strategy of highly aligned two-dimensional montmorillonite membranes for efficient proton transport, ***J. Mater. Chem. A***, 2025, 13, 25489-25497. (JCR Q1)

[2] **Zhenlei Wang**, Tingting Zhang*, Yunliang Zhao*, Yanhui Miao, Lingjie Zhang, Damiano Sarocchi, Shaoxian Song, Qiwu Zhang. Immobilization of Cd in contaminated soil by mechanically activated calcite: Sustained release activity-depended performance and mechanisms. **Chemical Engineering Journal.,** 2024, 482 149024. (JCR Q1).

[3] **Zhenlei Wang**, Yinxing Zhao, Tingting Zhang, Sizhe Lai, Qiwu Zhang, Yunliang Zhao. Mechanochemical dolomite accurately modulating the activity of newly formed Fe-hydroxide for superior and stable arsenic removal. **Separation and Puriffcation Technology.,** 2025, 362, 131901. (JCR Q1).

[4] Lianqiu Huang, **Zhenlei Wang***, Haoyu Bai, Lingjie Zhang, Renbo Gao, Yanhui Miao, Tingting Zhang, Damiano Sarocchi, Yuhan Song, Yunliang Zhao. Interfacial bimolecular interlocking strategy for constructing robust two-dimensional montmorillonite nanochannels for efficient proton transport. **Journal of Membrane Science**., 2026, 125863. (JCR Q1).

[5] Tingting Zhang, Di Wu, **Zhenlei Wang***, Guangsen Son, Xinyu Cai, Yunliang Zhao. Highly stable removal of low concentration phosphorus by mechanically activated $FeCO_3$: In situ synergistic mechanisms. Separation and Puriffcation Technology., 2024, 344, 127291. (JCR Q1).

[6] Shuyang Tan, Tingting Zhang, Cheng Cheng, **Zhenlei Wang***, Haiyang Li, Yunliang Zhao. Efficient removal and stepwise recovery of various heavy metals from water by using calcium carbonate with different activity. **Separation and Purification Technology.,** 2025, 354, 129142. (JCR Q1).

[7] Lingjie Zhang & **Zhenlei Wang**, Tingting Zhang, Xiongrui Jiang, Licai Chen, Hiram Joazet Ojeda Galván, Mildred Quintana, Shaoxian Song, Sridhar Komarneni, Yunliang Zhao. Bioinspired Tunable Subnanochannels in Two-Dimensional Montmorillonite Membranes for Fast and Stable Proton Transport. ***ACS Materials Lett.***, 2025, 7, 2835-2843. (JCR Q1)

[8] Lingjie Zhang, Yunjia Ling, Jianglin Yan, **Zhenlei Wang**, Yanhui Miao, Haoyu Bai, Tingting Zhang, Shaoxian Song, Mildred Quintana, Yunliang Zhao. Charged two-dimensional nanochannels with high ion density enabling ultrafast monovalent and multivalent ion conductivity. ***Chem. Sci.***, 2026, 17, 1735-1744. (JCR Q1)

[9] Lingjie Zhang, Jianglin Yan, **Zhenlei Wang**, Tingting Zhang, Shaoxian Song, Mildred Quintana, Yunliang Zhao. Solar-Driven Direct Lithium Extraction from Low-Quality Brines. ***Adv. Mater.***, 2026, 38, e12998. (JCR Q1)

[10] Lingjie Zhang, Jianglin Yan, Shichang Kang, **Zhenlei Wang**, Yanhui Miao, Renbo Gao, Tingting Zhang, Hiram Joazet Ojeda-Galván, Mildred Quintana, Haoyu Bai, Shaoxian Song, Yunliang Zhao. Tailoring Multiple Functional Domains of Lithium-Ion Sieves for Sustainable Lithium Extraction from Low-Quality Brines. ***ACS NANO***, 2025, 19, 33620-33631. (JCR Q1)

Relationship Between the Research Parts

The chapter 3 establishes the basis for efficient ion transport by regulating the intrinsic charge density and spatial ordering of MMT nanosheets. Building on this structural foundation, the chapter 4 further improves channel alignment and structural stability through dual-constrained assembly. The chapter 5 extends the regulation from channel architecture to interfacial chemistry by engineering acid-base pairs and hydrogen-bond networks, thereby optimizing the proton-transport microenvironment. Finally, the chapter 6 builds upon the established principles of structural and interfacial regulation and extends them to selective ion separation through edge functionalization and specific ion recognition.

Overall, these studies progressively advance from spatial structural regulation to interfacial chemical engineering, and from efficient proton transport to selective ion separation, providing a systematic foundation for the design of high-performance two-dimensional MMT functional membranes.

Appendix II. Experimental data

Table II.1 The proton conductivity of Nafion 117 and MMT membranes at 98% RH with different temperatures.

Temperature (°C)	Proton conductivity (mS cm^{-1})			
	l@MMT	m@MMT	h@MMT	Nafion 117
30	9.6568	12.47178	13.5124	39.27967
40	16.96526	22.90101	25.77625	55.88996
50	23.0012	38.23507	36.37263	67.2608
60	29.75659	58.82007	45.54667	80.72328
70	37.57139	67.75068	54.72825	92.30372
80	45.02679	79.10516	69.7715	110.91065

Table II.2 The proton conductivity of Nafion 117 and MMT membranes at 60 °C with different humidities.

Humidities (%)	Proton conductivity (mS cm^{-1})			
	l@MMT	m@MMT	h@MMT	Nafion 117
30	1.66024	4.20558	2.29057	0.83363
40	2.39419	5.1789	3.22823	1.61437
50	3.49246	8.61717	5.84462	3.91313
60	6.02326	12.88277	8.70974	12.4454
70	9.38142	19.44321	14.89414	24.52543
80	14.80462	30.72178	23.7462	37.03841
90	21.84276	44.41297	35.86434	51.80274
98	29.75659	58.82007	45.54667	80.72328

Table II.3 Conducting stability of MMT membranes under the cooling-heating cycle from 30 to 80 °C at 98% RH.

Time (h)	Proton conductivity (mS cm^{-1})		
	l@MMT	m@MMT	h@MMT
1	9.56	12.5	13.71
5	9.7	13.24	13.92

10	45.21	80.77	69.32
15	9.3	12.04	13.02
20	44.71	79.28	67.32
25	9.27	12.04	14.02
30	44.81	79.98	68.02
35	8.27	13.04	13.82
40	46.01	82.98	70.02
45	8.07	11.84	13.42
50	7.92	11.44	13.02
55	9.32	12.42	13.77
60	47.21	84.18	70.95
65	7.71	11.06	12.18
70	47.02	87.18	70.83
75	7.31	10.87	13.21
80	47.38	87.11	71.83
85	7.48	10.67	13.69
90	47.44	87.09	72.24
95	7.02	10.39	13.91
100	48.43	87.98	72.64

Table II.4 Proton concentrations within membranes at 98% RH with different temperatures.

Temperature (°C)	Proton concentrations (mmol cm^{-3})		
	l@MMT	m@MMT	h@MMT
30	0.90557	1.62054	1.91705
40	0.87854	1.54365	1.88026
50	0.85308	1.51388	1.81074
60	0.82905	1.49949	1.72642
70	0.79544	1.46251	1.7059
80	0.7745	1.41755	1.68174

Table II.5 Effective mobilities in within membranes at 98% RH with different temperatures.

Temperature (°C)	Ion mobility (10^{-4} cm^2 s^{-1} V^{-1})		
	l@MMT	m@MMT	h@MMT
30	1.10522	0.79764	0.73053
40	2.00141	1.5376	1.42083
50	2.79448	2.61764	2.08188
60	3.72	3.71997	2.73432
70	4.89543	4.51776	3.32504
80	6.0254	5.49125	4.2999

Table II.6 Temperature-dependent proton conductivities of the MMT and SMMT membranes.

Temperature (°C)	Proton conductivity (mS cm^{-1})	
	MMT	SMMT
30	70.38947	134.57895
40	103.25789	159.13158
50	124.00526	180.18947
60	155.27368	198.94211
70	170.84211	218.08947
80	183.52105	223.66316

Table II.7 Arrhenius plots of the MMT and SMMT membranes.

Temperature (1000/T K^{-1})	Ln Proton conductivity (mS cm^{-1})	
	MMT	SMMT
3.2987	4.25404	4.90215
3.19336	4.63723	5.06973
3.09454	4.82032	5.19401
3.00165	5.04519	5.29301
2.91418	5.14074	5.38491

2.83166	5.21233	5.41014

Table II.8 Representative I-V curves of the SMMT membrane recorded at 0.1 M HCl concentration at the straight and different curved states.

Site	Proton conductivity (mS cm^{-1})
	SMMT
1	143.33333
2	132.22222
3	132.38889
4	136.22222

Table II.9 Proton conductivity stability of the SMMT membrane under two heating-cooling cycles from 30 to 80 °C.

Time (h)	Proton conductivity (mS cm^{-1})
	SMMT
0	118.23529
1	119.41176
2	121.76471
3	316.47059
4	317.05882
5	318.82353
6	111.76471
7	112.35294
8	114.11765
9	297.05882
10	298.23529
11	298.82353

Table II.10 Temperature-dependent proton conductivities of the HMMT and HMAHP membranes.

Temperature (°C)	Proton conductivity (mS cm^{-1})	
	HMMT	HMAHP

30	113.81	142.7
40	140.48	165.03
50	157.66	195.81
60	191.64	206.77
70	207.58	236.32
80	240.39	266.84

Table II.11 Concentration-dependent proton conductivities of the HMAHP membranes at room temperature.

Concentration (mol/L)	Proton conductivity (mS cm^{-1})
	HMAHP
1E-6	7.1
1E-5	9.32
1E-4	10.2
0.001	12.14
0.01	35.24
0.1	149.53
1	225.26
7	112.35294

Table II.12 Arrhenius plots of the HMMT and HMAHP membranes.

Temperature (1000/T K^{-1})	Ln Proton conductivity (mS cm^{-1})	
	HMMT	HMAHP
3.2987	4.96074	4.73453
3.19336	5.10613	4.94507
3.09454	5.27714	5.06044
3.00165	5.33161	5.25562
2.91418	5.46519	5.33552
2.83166	5.58665	5.48226

Table II.13 Proton conductivity stability of the HMAHP membrane under 30 °C.

Time (h)	Proton conductivity (mS cm^{-1})

	SMMT
2	129.53
4	129.75
6	130.29
8	130.62
10	131.43
12	131.76
14	131.91
16	132.16
18	132.17
20	132.47
22	133.38
24	133.93

Table II.14 The amount of PEI diffusing from the aqueous phase to the organic phase in MMT/PA and ASMMT/PA membrane systems (PEI concentration was determined by spectrophotometer characterization).

Time (s)	Absorbance (a.u.)			
	MMT/PA	MMT/PA-10	MMT/PA-20	MMT/PA-30
0	0	0	0	0
10	0.176	0.226	0.254	0.223
20	0.254	0.314	0.341	0.378
30	0.367	0.389	0.45	0.482
40	0.401	0.442	0.545	0.562
50	0.471	0.49	0.632	0.673
60	0.494	0.542	0.715	0.768

Table II.15 Rejection of different ions as a function of the stokes radius for the pristine MMT/PA membranes and ASMMT/PA membranes.

stokes radius (Å)	Rejection (%)	
	MMT/PA	ASMMT/PA
1.25	19.46294	13.39744

1.84	12.5325	7.94402
2.38	25.56062	16.4506
3.1	76.80569	95.18748
3.47	94.28884	100
2.83166	19.46294	13.39744